# Pore-scale Study of Bio-mineral and Bio-gas Formations in Porous Media

by

Daehyun Kim

A Dissertation Presented in Partial Fulfillment
of the Requirements for the Degree
Doctor of Philosophy

Approved October 2019 by the
Graduate Supervisory Committee:

Leon A. van Paassen, Chair
Edward Kavazanjian
Claudia Zapata
Nariman Mahabadi Mahabad
Junliang Tao
Jaewon Jang

ARIZONA STATE UNIVERSITY

December 2019

ABSTRACT

The potential of using bio-geo-chemical processes for applications in geotechnical engineering has been widely explored in order to overcome the limitation of traditional ground improvement techniques. Biomineralization via urea hydrolysis, referred to as Microbial or Enzymatic Induced Carbonate Precipitation (MICP/EICP), has been shown to increase soil strength by stimulating precipitation of calcium carbonate minerals, bonding soil particles and filling the pores. Microbial Induced Desaturation and Precipitation (MIDP) via denitrification has also been studied for its potential to stabilize soils through mineral precipitation, but also through production of biogas, which can mitigate earthquake induced liquefaction by desaturation of the soil. Empirical relationships have been established, which relate the amount of products of these biochemical processes to the engineering properties of treated soils. However, these engineering properties may vary significantly depending on the biomineral and biogas formation mechanism and distribution patterns at pore-scale. This research focused on the pore-scale characterization of biomineral and biogas formations in porous media.

The pore-scale characteristics of calcium carbonate precipitation via EICP and biogenic gas formation via MIDP were explored by visual observation in a transparent porous media using a microfluidic chip. For this purpose, an imaging system was designed and image processing algorithms were developed to analyze the experimental images and detect the nucleation and growth of precipitated minerals and formation and migration mechanisms of gas bubbles within the microfluidic chip. Statistical analysis was performed based on the processed images to assess the evolution of biomineral size distribution, the number of precipitated minerals and the porosity reduction in time. The resulting images

from the biomineralization study were used in a numerical simulation to investigate the relation between the mineral distribution, porosity-permeability relationships and process efficiency. By comparing biogenic gas production with abiotic gas production experiments, it was found that the gas formation significantly affects the gas distribution and resulting degree of saturation. The experimental results and image analysis provide insight in the kinetics of the precipitation and gas formation processes and their resulting distribution and related engineering properties.

ACKNOWLEDGMENTS

I would like to express my sincere gratitude to many people who have contributed to this research over the years.

First of all, my advisor, Dr. Leon van Paassen, accepted me in his group. It was a great fortune to meet him and to work with him at Arizona State University. I was always amazed by his open mind, approachable character, endless curiosity, vast knowledge, and critical view. With his enduring encouragement, excellent guidance, and generous support, I successfully complete my doctoral degree.

I would like to thank my thesis committee members. Dr. Edward Kavazanjian and Dr. Claudia Zapata shared this journey with me since its beginning. Dr. Nariman Mahabadi is an invaluable friend and mentor. Dr. Junliang Tao provided me with a different point of view on my work. Dr. Jaewon Jang gave me a chance to start this journey. I really appreciate their support and insightful comments.

I also want to thank my friends and colleagues at the Arizona State University and Center for Bio-mediated and Bio-inspired Geotechnics for their assistance, encouragement, and discussion. Special thanks go to Yanxin Yang, Hamed Khodadadi, Liya Wang, Xianglei Zheng, Miriam Woolley, Juan Paez, Kimberly Martin, Sichuan Huang, Yong Tang, Caitlyn Hall, Sean O'Donnell, Angel Gutierrez, Bob Brier, Jean Larson, Nasser Hamdan, Mary Bankhead, Junghwoon Lee, Boyoung Jeong, and Minyong Lee.

This dissertation is dedicated to my parents, Seong-Ik and Myoryeon Kim, who have always supported me and encouraged me to pursue my dreams. This is also dedicated to my sister, Sohyeon Kim. All I have and will accomplish are only possible due to their love and sacrifice.

TABLE OF CONTENTS

Page

CHAPTER Page

CHAPTER Page

LIST OF TABLES

Table Page

LIST OF FIGURES

Figure Page

Figure Page

Figure Page

Figure Page

Figure Page

# CHAPTER 1

# INTRODUCTION

## 1.1 BACKGROUND

Most of traditional ground improvement techniques, such as jet grouting, pile driving, deep mixing, and vibratory compaction, are not appropriate to treat large volumes of soil since these techniques are expensive, require high pressure and heavy machinery, have a limited injecting distance, or they cannot be applied under or around existing facilities (*O'Donnell et al.,* 2017; *van Paassen,* 2009). In order to overcome the limitations of traditional ground improvement techniques, the potential of using bio-geo-chemical processes for applications in geotechnical engineering has been widely explored (*DeJong et al.*, 2010; *Mitchell & Santamarina,* 2005; *van Paassen,* 2009; *Phillips et al.,* 2013).

Pioneers in this field of research have found opportunities to use microbial activities in the subsurface, specifically Microbially Induced Carbonate Precipitation (MICP), to change the hydro-mechanical properties of soils, such as permeability (*Nemati & Voordouw*, 2003; *Whiffin et al.*, 2007), shear strength (*DeJong et al.,* 2006; *van Paassen,* 2009; *Whiffin,* 2004), and compressibility (*van Paassen,* 2009). The process of MICP by urea hydrolysis has been the focus of research. In this process bacteria containing the enzyme urease are cultivated in the lab or stimulated in situ and supplied with a solution containing urea and calcium chloride. The urease enzymes catalyze the hydrolysis of urea, to produce ammonium chloride and dissolved inorganic carbon (DIC). In presence of dissolved calcium, the DIC will precipitate to form calcium carbonate minerals, which fill up the pore space, reducing porosity and permeability and form cementing bonds between

existing soil particles increasing density, strength and stiffness. The remaining ammonium chloride needs to be removed. Instead of using bacteria, the urease enzymes can also be extracted from plants. In that case the process is referred to as Enzymatic Induced Carbonate Precipitation (EICP). Many studies have proved that MICP or EICP via urea hydrolysis can be applied to various engineering applications, e.g. ground reinforcement (*DeJong et al.,* 2006; *van Paassen,* 2009; *Whiffin,* 2004), liquefaction mitigation (*O'Donnell,* 2016), hydraulic control (*Nemati & Voordouw,* 2003; *Zhang et al.,* 2010), entrapping groundwater contaminants (*Ferris et al.,* 2004; *Fujita et al.,* 2004), enhancing oil recovery (*Brown,* 2010), increasing storage security of $CO_2$ (*Cunningham et al.,* 2011), and fugitive dust control (*Hamdan and Kavazanjian,* 2016). The increase in strength and stiffness or reduction in porosity and permeability are related to the amount of precipitated calcium carbonate. The targeted amount of induced precipitation depends on the application.

Besides urea hydrolysis, several other microbial processes have been investigated for their potential to stimulate biomineralization. (*De Jong et al.* 2010; *Karatas,* 2008). Microbial denitrification is one of these processes that is used to induce calcium carbonate precipitation (*van Paassen et al.,* 2010). The process is slower than urea hydrolysis and requires more flushes at lower concentration; but in contrast to urea hydrolysis, denitrification does not result in any byproducts that require removal. One of these byproducts is nitrogen gas, which has been shown to have ground improvement potential, mitigating earthquake induced liquefaction through desaturation of the soil (*He,* 2013; *O'Donnell,* 2016). About 5 to 10 % of desaturation has been shown to be sufficient to dampen pore pressure build up during cyclic loading. The required amount of substrates to

desaturate a soil is much less than the amount of required calcium carbonate to cement the soil through biomineralization (*van Paassen et al.,* 2017). However, as the persistence of the gas may be limited, it is proposed to use the process of Microbial Induced Desaturation and Precipitation (MIDP) by denitrification as a two-stage ground improvement method (*O'Donnell et al.*, 2017a, b). During the first phase the soil is stabilized through biogas formation and if necessary in a second stage through biomineralization.

## 1.2 MOTIVATION

The processes of MICP, EICP or MIDP have been extensively studied and empirical relationships have been established between the engineering properties of treated soils such as soil strength and permeability and the overall amount of biomineral and biogas formations. However, these empirical relationships may significantly vary depending on the biomineral and biogas formation patterns including the location, size, and distributions, which require to be examined with pore-scale studies. This research will focus on the pore-scale characterization of biomineral and biogas formations in porous medium.

## 1.3 SCOPE AND ORGANIZATION

In this study, the pore-scale characteristics of calcium carbonate precipitation via EICP and biogenic gas formation via MIDP were explored by visual observation in a transparent porous media using a microfluidic chip at a larger scale. For this purpose, an imaging system was designed and image processing algorithms were developed to analyze the experimental images and detect nucleation and growth of precipitated minerals and formation and migration of gas bubbles within the microfluidic chip. Statistical analysis was performed based on the processed images to assess the evolution of biomineral size

distribution, the number of precipitated minerals and degree of saturation over time due to the gas formation. The experimental results and image analysis provide insight in the kinetics of the precipitation process and gas formation and distribution. The purpose of this research is to attain a fundamental understanding of the process of biomineral and biogas formations at pore-scale. Specifically, the goals of this work are to:

- Develop experimental testing systems and image processing algorithms for statistical evaluation of biomineral and biogas formations at pore-scale.
- Characterize biomineral and biogas formation patterns at pore-scale.
- Interpret the experimental results and study the effect of biomineral and biogas formations on the hydrodynamic properties of porous media.
- Interpret biogeochemical transformations of biomineral and biogas formations at pore-scale by computational simulations.
- Improve insights on the kinetics of biomineral and biogas formations in porous media.

This dissertation is organized as follows.

- Chapter 2 provides a literature review to give context to the background knowledge of microbially induced mineral and gas formations.
- Chapter 3 describes a study on the kinetics and pore-scale characteristics of biological calcium carbonate precipitation in porous media using microfluidic chip experiment.
- Chapter 4 presents a study in which the results of Chapter 3 are used to investigate how the pore-scale characteristics of the precipitated minerals affect the evolution

of hydrodynamic properties of porous media treated with multiple cycles of bio-mineralization using a hybrid experimental-numerical approach.

- Chapter 5 investigates biogenic gas formation mechanisms in comparison to the rapid $CO_2$ gas formation via depressurization to assess how the rate of gas formation affects the gas formation and migration mechanisms and resulting gas distribution and equilibrated degree of saturation.
- Chapter 6 summarizes the conclusions of this study and provides recommendations for further studies.

# CHAPTER 2

# LITERATURE REVIEW

## 2.1 PRIOR STUDIES ON NUMERICAL MODELLING FOR ENGINEERING APPLICATION OF BIOMINERAL PRECIPITATION

The design of engineering applications of MICP processes relies on availability of predictive models. However, since modeling of MICP in natural soil systems involves multiphase reactive transport and interactive coupled processes, this is challenging (*Burbank et al.,* 2013; *Hommel et al.,* 2016). Several numerical models have been developed and validated with a wide range of lab- and field-scale experimental studies. In order to predict the results of MICP process, these models interpret the MICP process at different scales including pore-scale (*Kim et al.,* 2017; *Mahabadi et al.,* 2017; *Qin et al.,* 2016), column-scale (*Barkouki et al.,* 2011; *Martinez et al.,* 2011), meter-scale (*Nassar et al.,* 2018), and large-scale (*van Wijngaarden et al.,* 2011, 2012, 2013). The geochemical processes for MICP can be modelled with different levels of complexity. Simplified models describe the process using a single chemical reaction equation (*Cuthbert et al.,* 2012; *Hommel et al.,* 2015; *Qin et al.,* 2016). More advanced models include geochemical speciation reactions of the different solute species often by using specific geochemical speciation software packages such as PHREEQC (*Charlton & Parkhurst,* 2011; *Parkhurst & Appelo,* 2013), Orchestra (*Salek et al.,* 2016; *Ubbink,* 2013), and TOUGHREACT (*Barkouki et al.,* 2011). Although, currently developed models allow to predict the distribution of the solute species and solid minerals in time, validation of these predictions using actual experimental results is still limited (*Barkouki et al.,* 2011; *van Wijngaarden et*

*al.,* 2016). The parameters, which describe the kinetics of urea hydrolysis, such as the maximum urease activity, substrate affinity or product inhibition and enzymatic decay, or the kinetics of mineral nucleation and growth are often not implemented in these models or mathematically fitted to the experimental results.

## 2.2 LARGE VARIATION IN EMPIRICAL CORRELATION BETWEEN ENGINEERING PROPERTIES AND BIOCEMENTED MATERIAL

In order to employ biomineralization for engineering applications, empirical correlations have been established relating the amount of calcium carbonate to engineering properties (*Al Qabany et al.,* 2011; *Burbank et al.,* 2013; *Mortensen et al.,* 2011; *Terzis & Laloui,* 2018; *van Paassen,* 2009; *Whiffin et al.,* 2007; *Zhao et al.,* 2014). However, these empirical correlations exhibit large variability. For example, Figure 2.1 shows empirical correlations between unconfined compressive strength and $CaCO_3$ content reported in the literature (*Gomez et al.,* 2017; *Terzis & Laloui,* 2018; *van Paassen et al.,* 2010; *Yasuhara et al.,* 2012). The observed variability in the engineering properties of the treated soils depends on many factors as explained in Figure 2.2. First, the initial conditions prior to treatment (Box I in Figure 2.2), which include the initial soil properties of the treated material, such as grain or pore size distribution, relative density and surface characteristics, and the environmental conditions, such as depth, temperature, pressure and groundwater chemistry (e.g. pH, salinity), will affect the feasibility, design and performance of the imposed treatment strategy (Box II in Figure 2.2), and the resulting engineering properties. The imposed treatment variables, which include the composition and concentration of the substrate solution, the type, amount and specific activity of the enzyme or micro-

organisms, and the injection strategy (mixing or permeation) together with the initial conditions will determine the properties of precipitated carbonate minerals (Box III in Figure 2.2). The characteristics of the precipitated minerals, which include the amount, size, mineral type, shape, texture, location and distribution, will define the final engineering properties of the treated soil mass. However, due to the complex coupling between the different variables and the wide range of potential initial and imposed process conditions, a large variability is expected for both the mineral properties and resulting engineering properties (Box IV).

Scanning Electron Microscopy (SEM) images has been widely used to verify the existence of precipitated carbonate mineral within the biotreated materials (*Al Qabany et al.*, 2011; *DeJong et al.*, 2010; *van Paassen*, 2009). *DeJong et al.* (2010) analyzed SEM images of a thin cross section of MICP treated sands and proposed potential precipitation

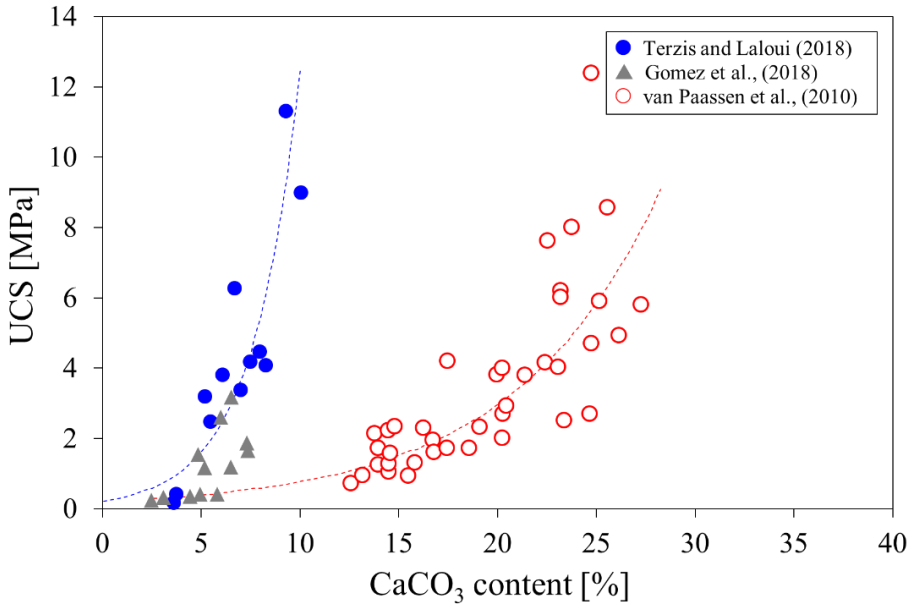


**Figure 2.1.** Empirical correlations relating unconfined compressive strength of MICP treated soils to the amount of calcium carbonate precipitation

## Key Determinants in Biomineralization Process

### *I. Initial Conditions*

| Soil Characteristics | Environmental Conditions |
|---|---|
| ▪ Grain size distribution<br>▪ Pore size distribution<br>▪ Relative density<br>▪ Particle surface characteristics | ▪ Depth<br>▪ Temperature<br>▪ Pressure<br>▪ Groundwater chemistry (pH, salinity) |

### *II. Imposed Process Boundary Conditions*

**Injection or Treatment Strategies**

- Composition and concentration of the substrate solution
- Type, amount, and specific activity of the enzyme or micro-organisms
- Number of flushes
- Injection strategies (mixing and permeation) or rate

### *III. Product Properties*

**Pore-scale Characteristics of Precipitated Mineral**

- Amount, number, and size of precipitated minerals
- Type, structure (shape), and texture of precipitated mineral
- Location and spatial distribution of precipitated mineral

### *IV. Engineering Properties*

**Engineering Properties of Treated Soil**

- Unconfined compressive strength, shear strength
- Permeability
- Compressibility and stiffness
- Seismic response, s-wave and p-wave velocities

**Figure 2.2.** Key factors affecting the biomineralization process and corresponding engineering properties of biotreated soils

patterns and failure mechanisms. *Van Paassen* (2009) found that mineral type, size and spatial distribution can vary depending on the precipitation conditions. Figure 2.3 demonstrates the large variety of precipitation patterns and mineral types and characteristics obtained via stimulating MICP, including randomly distributed calcite formation within the size range of 10~20 μm (Figure 2.3a), mixed lumps of spherical vaterite and rhombohedral calcite crystals up to 70 μm in size in silica sand (Figure 2.3b), a uniform coating of small calcite crystals 2~5 um in size on the surface of carbonate sands, and large rhombohedral calcite crystals up to 200 μm in size (Figure 2.3d).

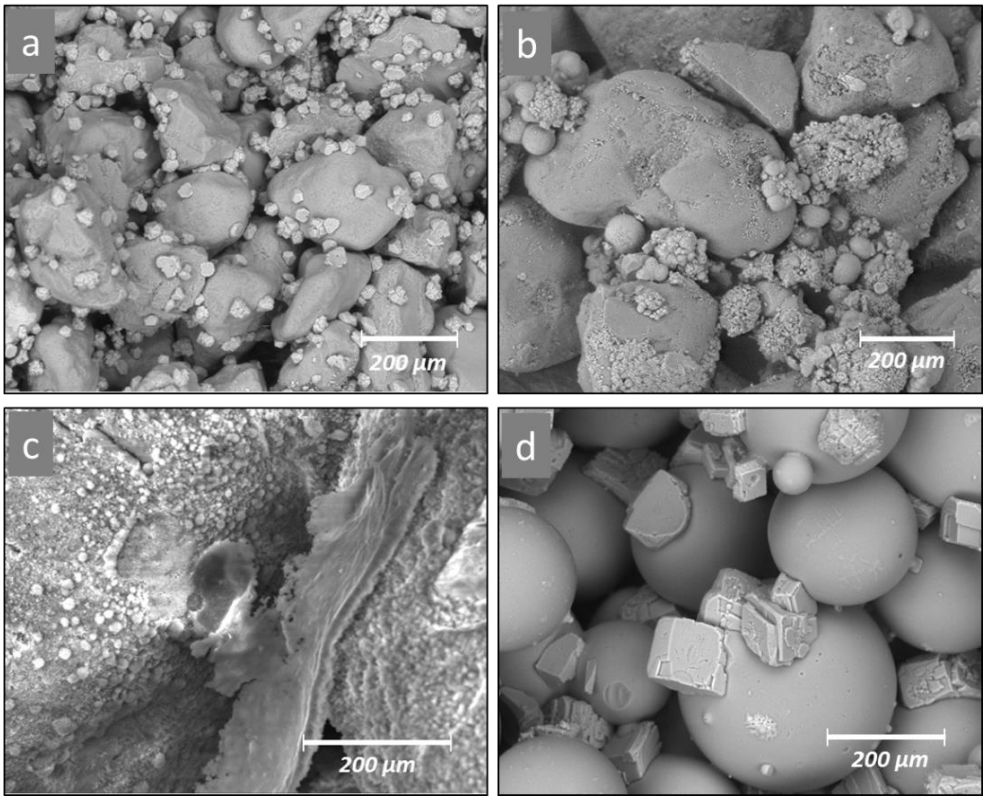


**Figure 2.3.** Large variation of biomineral type and precipitation patterns (a, b and c are SEM images of MICP treated sands, and d is SEM image of MICP treated glass beads, from *van Paassen, 2009*): (a) Randomly distributed calcite crystals, (b) Simultaneous formation of spherical vaterite and agglomerated calcite crystals, (c) Uniform coating calcite and bulk calcite sheets, (d) Irregular distribution of relatively large rhombohedral calcite crystals

## 2.3 REVIEW OF BIOGAS FORMATION VIA DENITRIFICATION

Urea hydrolysis has been considered and studied as the most common process for MICP due to its efficiency and rapid process time to induce carbonate mineral precipitation within soils. However, urea hydrolysis also produces ammonium as a byproduct which is a potential toxic substance required to be removed. Microbial denitrification has shown the potential as an alternative MICP mechanism since it can precipitate carbonate mineral (much slower than urea hydrolysis). In addition, denitrification also can produce biogenic gases, nitrogen and carbon dioxide, as byproducts which are non-toxic gas and able to desaturate the treated soils. In particular, desaturation by biogenic gas formation during denitrification has been suggested as an application to mitigate both static liquefaction (*He & Chu,* 2014; Pham et al., 2016) and earthquake-induced liquefaction (*He et al.,* 2013; *Kavazanjian et al.,* 2015; *Rebata-Landa & Santamarina,* 2012).

Denitrifying organisms are ubiquitous in the subsurface and one of well-known denitrifying organisms is *Pseudomonas denitrificans* which are very common in subsurface and aquatic environments (*Ehrlich,* 2002; *Fredrickson and Fletcher,* 2001; *Fujita et al.,* 2000; *Hamdan et al.,* 2016; *Karatas,* 2008). Denitrifying organisms are active within oxygen deficient subsurface condition in the presence of an electron acceptor (e.g. $NCO_3^-$). Denitrification is also expected to be a predominant microbial reaction under typical subsurface conditions due to highly negative standard Gibbs free energy ($\Delta G^o$ = -785 kJ/mol) in comparison to that of urea hydrolysis ($\Delta G^o$ = -27 kJ/mol).

It has been known that a small reduction of soil water saturation is sufficient to significantly increase the cyclic resistance of soils (*Arab et al.,* 2011; *Tsukamoto et al.,* 2002; *Yang et al.,* 2004; *Yegian et al.,* 2007; *O'Donnell,* 2016). Recent studies have shown

that the saturation level could be decreased to 80~95 % via microbial denitrification due to the nitrogen gas formation within several days (*Nakano,* 2018; *O'Donnell et al.,* 2017; *Pham et al.,* 2016). There also have been efforts to develop numerical models to predict the desaturation of soils via microbially induced denitrification, which theoretically estimate the amount of nitrogen gas formation at different depth or pressure levels using the Henry's law and ideal gas law (*van Paassen et al.,* 2018; *Hall et al.,* 2018). However, these models and experiments assume homogeneous gas distribution throughout the soil. Information about the spatial distribution and persistence of the biogenically formed gas is limited and requires further studies.

Researchers have investigated the distribution patterns in biogenic gas formation through denitrification. *He* (2013) observed that large gas pockets were produced during microbial denitrification and non-uniformly distributed using X-ray CT cross section images. *Pham et al.* (2016) visualized produced biogenic gas within PVC sand column using 3D X-ray CT tomography. Most of the gas appeared to be present in coarser grained sand at the top and bottom of the column, while in a finer grained sand the produced gas created cracks mostly in the upper half of the sand column. Although it has been found that a small fraction of gas in the pores can significantly affect the mechanical behavior of soils, it is not clear how the mechanism of biogenic gas formation within a soil system will affect the spatial distribution, and how the equilibrated degree of saturation after treatment affects the mechanical response and persistence of the gas phase.

# CHAPTER 3

# BIOMINERAL FORMATION IN POROUS MEDIA: AN EXPERIMENTAL STUDY

This chapter has been submitted to *Water Resources Research Journal* as Kim, D., Mahabadi, N., Jang, J., van Paassen, L. A. (2019). "Assessing the Kinetics and Pore Scale Characteristics of Biological Calcium Carbonate Precipitation in Porous Media using a Microfluidic Chip Experiment." The article is under review after the first revision."

## ABSTRACT

Biomineralization through Microbially or Enzymatically Induced Calcium Carbonate Precipitation (MICP/EICP) by urea hydrolysis has been widely investigated for various engineering applications, such as increasing strength and stiffness or reducing permeability in granular soils or fractured rocks. Empirical correlations relating the amount of mineral precipitation to engineering properties show a large variation, which can be partly attributed to the pore-scale characteristics of the precipitated minerals. This study aimed to gain insight into the kinetics and pore-scale characteristics of calcium carbonate precipitation in porous media. A reactive solution was flushed 10 times through a transparent microfluidic chip to stimulate hydrolysis of urea and precipitation of calcium carbonate. The process was monitored through time-lapse imaging. An image-processing algorithm was developed to detect the individual precipitated minerals and separate them from the grains and trapped air. Statistical analysis was performed to quantify the number and size distribution of precipitated minerals during each treatment cycle and the

cumulative volume, surface area, bulk precipitation rate, and supersaturation were calculated. Results were compared with a simple numerical model and existing theory on crystal nucleation and growth. The results showed that despite a limited resolution the observed bulk precipitation kinetics reasonably corresponded with simulated results, but were significantly affected by the assumed particle shape. The cumulative crystal volume (assuming a semi-spherical crystal shape), bulk precipitation rate and number of observable crystals were lower than expected. Possible explanations for observed discrepancies are discussed, including the presence of inhibiting compounds, local pore-clogging or observation bias.

## 3.1 INTRODUCTION

Biomineralization has potential for various engineering applications, e.g. improving soil strength (*Phillips et al.,* 2013; *van Paassen,* 2009; *Whiffin et al.,* 2007), reducing the hydraulic conductivity of soils (*Nemati & Voordouw,* 2003; *Zhang et al.,* 2010), immobilizing groundwater contaminants (*Ferris et al.,* 2004; *Fujita et al.,* 2004), enhancing oil recovery (*Cunningham et al.,* 2009), increasing storage security of $CO_2$ (*Cunningham et al.,* 2011), and fugitive dust control (*Hamdan & Kavazanjian,* 2016). Biomineralization can be stimulated through Microbially or Enzymatically Induced Carbonate Precipitation (MICP or EICP) by stimulating urea hydrolysis in presence of dissolved calcium ions. Urea hydrolysis is a slow irreversible reaction, which can be catalyzed by the enzyme urease. The urea is dissolved in water and hydrolyzes into ammonia and inorganic carbon. In aqueous solution, the ammonia is in equilibrium with ammonium, while the inorganic carbon can be present as carbon dioxide, bicarbonate or

carbonate depending on pH, or it can form complex ions in combination with calcium. At neutral pH, the dominant species are ammonium and bicarbonate and the overall reaction of urea hydrolysis is:

$$CO(NH_2)_2 + 3H_2O \xrightarrow{Urease} 2NH_4^+ + HCO_3^- + OH^- \quad (1)$$

The pH increases as hydroxide is generated to maintain the charge balance. An increase in pH causes bicarbonate to dissociate to carbonate and release a proton.

$$HCO_3^- \rightarrow CO_3^{2-} + H^+ \quad (2)$$

And in the presence of sufficient calcium ions, calcium carbonate will precipitate.

$$Ca^{2+} + CO_3^{2-} \rightarrow CaCO_3(s) \quad (3)$$

The acid released due to speciation and precipitation buffers the alkalinity production from the hydrolysis reaction and consequently the pH remains around neutral. As the precipitated biominerals fill the pore space they will reduce porosity and permeability and by forming cementing bonds between the grains in granular soils they may increase strength and stiffness of the soil matrix.

The design of engineering applications of MICP or EICP processes relies on availability of predictive models. However, since modeling of EICP in natural soil systems involves multiphase reactive transport, non-linear reaction kinetics and interactive coupled processes, this is a challenging task (*Burbank et al.,* 2013; *Hommel et al.,* 2016). Several numerical models have been developed, of which some have been validated using experimental studies. These studies have interpreted the process at different scales including pore-scale (*Kim et al.,* 2017; *Mahabadi et al.,* 2017; *Qin et al.,* 2016), column-scale (*Barkouki et al.,* 2011; *Martinez et al.,* 2011), meter-scale (*Nassar et al.,* 2018), and large-scale (*Van Wijngaarden et al.,* 2011, 2012, 2013). The geochemical processes for

MICP can be modelled with different levels of complexity. Simplified models describe the process using a single chemical reaction equation, which combines equations 1, 2 and 3. (*Cuthbert et al.,* 2012; *Hommel et al.,* 2015; *Qin et al.,* 2016). More advanced models include geochemical speciation reactions of the different solute species often by using specific geochemical speciation software packages such as PHREEQC (*Charlton & Parkhurst,* 2011; *Parkhurst & Appelo,* 2013), Orchestra (*Salek et al.,* 2016; *Ubbink,* 2013), or TOUGHREACT (*Barkouki et al.,* 2011). Some of these models included precipitation kinetics, describing the nucleation and growth rate of $CaCO_3$ minerals (e.g. *Barkouki et al.*, 2011; *Ebigbo et al.,* 2012; *Qin et al.,* 2016). *Van Paassen* (2009) showed that biochemical conversion could be reasonable well predicted, using a simplified single reaction approach, in which the substrate concentrations, and kinetics of urea hydrolysis are used as input variables, but more complex models were required to predict pH, supersaturation and resulting characteristics of precipitated minerals. However, quantitative prediction to a level at which the pH, and the number, size and type of crystals were simulated accurately was not yet possible as the parameters, which describe the kinetics of urea hydrolysis, such as the maximum urease activity, substrate affinity, product inhibition, or enzymatic decay, and the kinetics of mineral nucleation and growth in such complex models could not be determined a priori and needed to be fitted mathematically to experimental results.

In order to relate the amount of calcium carbonate to engineering properties, i.e. porosity, permeability, strength or stiffness, empirical relationships have been established. (*Al Qabany et al.,* 2011; *Burbank et al.,* 2013; *Mortensen et al.,* 2011; *Terzis & Laloui,* 2018; *van Paassen,* 2009; *Whiffin et al.,* 2007; *Zhao et al.,* 2014). However, these empirical correlations exhibit large variability (*Terzis & Laloui,* 2018; *van Paassen,* 2010; *Yasuhara*

*et al.,* 2012). The observed variability in the engineering properties of the treated soils depends on many factors. The characteristics of precipitated carbonate minerals, such as the amount, size, mineral type, shape, texture, location and distribution, have been found to significantly affect the mechanical response (*Almajed et al.,* 2019; *De Jong et al.,* 2010). Many studies have used Scanning Electron Microscopy (SEM) images to analyze the characteristics of carbonate minerals formed through MICP or EICP (e.g. *Almajed et al.,* 2019; *Al Qabany et al.,* 2011; *DeJong et al.,* 2010; *van Paassen,* 2009). *DeJong et al.* (2010) analyzed SEM images of a thin cross section of MICP treated sands and suggested that the failure mechanism depended on the precipitation pattern. *Van Paassen* (2009) found that mineral type, size and spatial distribution can vary depending on the precipitation conditions. Although high-resolution imaging tools, such as SEM, Atomic Force Microscopy (AFM) or Transmission Electron Microscopy (TEM) can provide valuable information about mineral type and structure, they are not capable of monitoring the MICP process during treatment and don't provide statistically quantifiable information about the spatial and property distribution of the precipitated minerals throughout a larger porous domain. Alternatively, microfluidic chips have been used to investigate precipitation kinetics and crystal characteristics of calcium carbonate in porous media (*Dawe & Zhang,* 1997; *Wang et al.,* 2019; *Yoon et al.,* 2012; *Zhang et al.,* 2010). *Dawe & Zhang* (1997) developed a method in which they could observe crystal nucleation and growth inside a microfluidic chip under a constant supersaturation condition. They investigated the effects of the solution composition, temperature and the presence of a gas-liquid interface on the spontaneous nucleation and the calcite crystal growth rate. *Zhang et al.* (2010) used a microfluidic chip to study precipitation induced by transverse mixing of

two separated solutions containing calcium and carbonate. The results were compared to numerical simulations by *Yoon et al.* (2012). *Wang et al.* (2019) used microfluidic chips to study the formation of calcite crystals by MICP. Using sequential microscopic images, with an image resolution of 0.65 μm/pixel, they were able to qualitatively describe the shape and size of the crystals, while varying the amount and composition of the injected solutions.

In this study, the pore-scale characteristics of calcium carbonate precipitation via EICP were explored by visual observation in a microfluidic chip. Experiments were performed at a larger scale. For this purpose, we used an imaging system with a digital camera with micro-lens. An image processing algorithm was developed to analyze the experimental images and detect the growth of individual and agglomerated precipitated minerals with time for the entire microfluidic chip pore space. Statistical analysis was performed based on the processed images to assess the evolution of biomineral size distribution and the number of precipitated minerals over time. Existing theory on crystal nucleation and growth and a simplified model describing the combined process of urea hydrolysis and calcium carbonate precipitation was used to interpret the results of the image analysis and provide insight on the kinetics of the precipitation process.

## 3.2 THEORETICAL BACKGROUND

### 3.2.1 Kinetics of Calcium Carbonate Precipitation

The amount, size and mineralogy of calcium carbonate minerals depend on the kinetics of the precipitation process. The precipitation process can be divided in two separate mechanisms: crystal nucleation and crystal growth. Several models have been proposed to describe the rate of calcite crystal growth (e.g. *Lasaga,* 1981; *Nancollas &*

*Reddy*, 1971; *Noiriel et al.*, 2012; *Söhnel & Garside*, 1992). A general equation for the bulk precipitation rate, $r_p$, [kmol $m^{-3}$ $h^{-1}$] is often described as:

$$r_p = k_p(S-1)^n \tag{4}$$

in which $k_p$ is the bulk kinetic 'constant' in [kmol $m^{-3}$ $h^{-1}$], $S$ is the supersaturation, and $n$ is the kinetic order. The kinetic order depends on the growth mechanism. For example, first order expressions (n = 1) have been suggested to describe the kinetics of calcite growth (*Kazmierczak et al.*, 1982; *Nancollas & Reddy*, 1971), for example when the crystallization process is limited by adsorption of lattice ions (*Nielsen*, 1984) or when the rate is controlled by diffusion (*Pokrovsky et al.*, 2005). Second order expressions (n = 2) are introduced to describe growth at screw dislocations by the spiral mechanism theoretically (*Blum & Lasaga*, 1987; *Lasaga*, *1998*; *Then et al.*, 2010) and have been measured experimentally (*House*, 1981; *Nancollas & Reddy*, 1973; *Shiraki & Brantley*, 1995). The second order expression is suggested to describe the precipitation rate for supersaturated solutions, where S is close to 2 while the pH of solution is above 7 (*Davies & Jones*, 1955; *Dawe and Zhang*, 1997). Different orders of expressions have been reported (*Söhnel & Mullin*, 1982) but were not considered in this study. The supersaturation $S$ is defined as:

$$S = \sqrt{\frac{IAP}{K_{sp}}} \tag{5}$$

where *IAP* is the ionic activity product of the dissolved precipitating ions (calcium and carbonate) and $K_{sp}$ is the solubility product of the mineral phase. Calcium carbonate is a polymorph, which implies that the crystal lattice can have varying configurations. The most common and stable calcium carbonate minerals are calcite and aragonite. Aragonite may form when the growth of calcite is inhibited due to the presence of dissolved ions, such as

magnesium and strontium (*Hill & Forti,* 1997; *Morse,* 1983; *Perdikouri et al.,* 2013). Vaterite and amorphous calcium carbonate (ACC) are meta-stable calcium carbonate minerals and calcium carbonate monohydrate and ikaite are calcium carbonate minerals, which have water molecules incorporated in their crystals lattice. The solubility product depends on the mineral type and varies with temperature (*Gal et al.,* 1996*; Plummer & Busenberg,* 1982). For example, at 25 ºC. $K_{sp}$ is $10^{-8.48}$ for calcite, $10^{-8.34}$ for aragonite, $10^{-7.91}$ for vaterite, and $10^{-6.40}$ for ACC (*Gal et al.*, 1996; *Plummer & Busenberg,* 1982; *Sass et al.,* 1983). Due to their higher solubility product, the meta-stable precursor minerals typically can only occur under conditions of very high supersaturation, and may dissolve and recrystallize into a more stable polymorph.

The bulk kinetic 'constant', $k_p$, is in fact not a constant, but a function of the growth mechanism, mineral type, crystal surface area and number of crystals:

$$k_p = \frac{k_g A_T}{V_m} = \frac{k_g A_c N}{V_m} \tag{6}$$

in which $k_g$ is the actual crystal growth rate constant in [m $s^{-1}$], $A_T$ is the total crystal surface area [$m^2$], $A_c$ is the average single crystal surface area [$m^2$], $N$ is the number of crystals in [$m^{-3}$] and $V_m$ is the molar volume of the crystallizing solid in [$m^3$ $kmol^{-1}$], which is the ratio between molar mass ($M_c$) in [g $mol^{-1}$] and solid density ($\rho_c$) in [g $m^{-3}$]. The growth rate constant, $k_g$, in [m $s^{-1}$] depends on the mineral type and temperature. For calcite, $M_c$ = 100 [kg $kmol^{-1}$], $\rho_c$ = 2710 [kg $m^{-3}$] and consequently $V_m$ = 0.0369 [$m^3$ $kmol^{-1}$] (*Graf,* 1961). The actual crystal growth rate constant depends on mineral type and temperature. For calcite, $k_g$ is about $10^{-11}$ [m $s^{-1}$] at 25 ºC (*Kralj et al.*, 1997). Both $A_c$ and $N$ can vary in time during the biomineral formation process. The overall precipitation rate is proportional to the total surface area, $A_T$, of precipitated minerals calcite over the solution volume (*Appelo*

*& Postma,* 2004), in which the total surface area can be defined as the sum of surface areas of each individual crystal.

Nucleation, i.e. the formation of new crystals, occurs when the solution becomes sufficiently supersaturated that clusters of dissolved molecules coagulate and get a critical size, which enables them to resist the tendency to redissolve, and allows them to start growing as a solid crystal. When nuclei appear in a pure liquid phase this is called homogeneous nucleation (primary nucleation). The theoretical rate of homogeneous nucleation for a spherical cluster of molecules is described using an Arrhenius equation, in which the activation energy, $\Delta G_{crit}$, needs to be exceeded before nuclei can start to grow (*Mullin,* 2001):

$$J = \frac{dN}{dt} = A \exp\left[-\frac{\Delta G_{crit}}{kT}\right] = A \exp\left[-\frac{16\pi\gamma^3 v^2}{kT3\left(kT(\ln S)\right)^2}\right] \quad (7)$$

where $J$ is the nucleation rate in [$m^{-3}$ $s^{-1}$], $A$ is the pre-exponential constant in [$m^{-3}$ $s^{-1}$], $\gamma$ is the interfacial tension in [J $m^{-2}$], $v$ is the molecular volume of $CaCO_3$ (6.13 x $10^{-29}$ $m^3$), $k$ is Boltzman constant (1.3805 x $10^{-23}$ J $K^{-1}$) and $T$ is temperature [K]. The pre-exponential component, $A$, represents the frequency of collisions between reactant molecules, and can be estimated following *Nielsen* (1964), but is typically assumed to be constant. In this study we used A ≈ $10^{35.5}$ [$m^{-3}$ $s^{-1}$], following *Söhnel & Mullin* (1982). Assuming constant temperature at 298 K the nucleation rate can be calculated for different values of surface tension, which has been reported to range from 7 to 280 [mJ $m^{-2}$] (*Söhnel & Mullin,* 1982). In this study we selected several values: $\gamma$ = 0.029 J $m^{-2}$ in presence of polymeric substrate (*Dalas et al.,* 1988) to $\gamma$ = 0.064 or 0.098 J $m^{-2}$ at which spontaneous nucleation occurs in a homogeneous solution in absence of nucleation sites (*Liouliou et al.,* 2007; *Söhnel &*

*Mullin,* 1982) or $\gamma$ = 0.120 J $m^{-2}$ in the presence of impurities which inhibit nucleation (*Söhnel & Mullin,* 1982). This equation indicates that theoretical nucleation rates may vary extremely, depending on the supersaturation and the presence of compounds, which either lower or increase the interfacial tension, and illustrates the difficulty to properly predict the rate of precipitation in case of spontaneous nucleation. On top of that, in the presence of seed crystals or other surfaces such as bacteria, enzymes, gas bubbles (*Dawe & Zhang*, 1997) or other minerals, which can act as a crystal nucleus, new crystals can appear through heterogeneous nucleation. In this case, the activation energy for nucleation reduces by the presence of seed crystals or other nucleation sites. Not all the minerals can act as a nucleus. For example, *Lioliou et al.* (2007) showed that quartz was hardly active as nucleation site, while calcite obviously did. Consequently, in presence of calcite seeds, heterogeneous nucleation can take place at lower supersaturation or nucleation can be skipped completely (*Lioliou et al.,* 2007; *Qin et al.,* 2016; *Tai & Chen,* 1995). The impact of bacterial cell surfaces as nucleation sites on the morphology, mineralogy and size of $CaCO_3$ precipitation has been also discussed (*Mitchell & Ferris,* 2006). Once crystals are present in the solution, their growth rate depends on the supersaturation and can be predicted using equations 4 and 6 above, where the crystal growth rate constant can vary depending on the type of calcium carbonate mineral phase.

### 3.2.2 Simplified Model Describing the Kinetics of EICP

When combining hydrolysis of urea and precipitation of calcium carbonate, the rate of precipitation and the characteristics of resulting precipitated $CaCO_3$ minerals will depend on the hydrolysis rate, as the hydrolysis and precipitation reactions are coupled.

The hydrolysis rate is a function of several factors including the amount and source of urease enzyme, concentration of urea, calcium, pH, temperature, and other environmental conditions, such as presence of inhibiting compounds, salinity, etc. (e.g. *Fidaleo & Lavecchia,* 2003; *Hammes & Verstraete,* 2002; *Hammes et al.,* 2003; *Lauchnor et al.,* 2015; *Mortensen et al.,* 2011; *Stocks-Fischer et al.,* 1999; *Whiffin,* 2004; *van Paassen*, 2009). The observed urease activity in EICP or MICP experiments is often lower than expected. Flocculation or flush out of enzymes may reduce the available amount of enzymes in the porous medium, or the hydrolysis rate may decrease in time, as a result of decay or encapsulation of the bacteria or enzymes into a crystal lattice.

Combining urea hydrolysis and calcium carbonate precipitation, *van Paassen* (2009) demonstrated through batch experiments and numerical simulations that once nucleation has occurred and there is still sufficient calcium present in the solution, the hydrolysis rate and bulk precipitation rate are approximately equal during the major part of the reaction.

$$r_h \approx r_p \tag{8}$$

This suggests that the bulk precipitation rate can be predicted if the hydrolysis rate is known. Also, it can be deduced by combining and inverting Equations 4 and 6 that the supersaturation is directly related to the bulk precipitation rate, and consequently a function of the hydrolysis rate:

$$S = \sqrt[n]{\frac{r_p V_m}{k_g A_T}} + 1 \tag{9}$$

Which implies that at low hydrolysis rates precipitation occurs at relatively low supersaturation, while at high hydrolysis rates supersaturation is relatively high and may

remain high for a prolonged period of time. Conditions of prolonged high supersaturation, may extend growth of meta-stable $CaCO_3$ minerals, such as amorphous $CaCO_3$ or vaterite, which was demonstrated by *Al-Thawadi & Cord-Ruwisch* (2012) or *van Paassen* (2009).

In this study we used a simplified model to predict the cumulative volume of precipitated minerals, following (e.g. *Connolly et al.,* 2013; *Fidaleo & Lavecchia,* 2003; *Lauchnor et al.,* 2015; *van Paassen,* 2009; *van Wijngaarden et al.,* 2011). Using the applied amount of substrates and enzymes and the urease activity provided by the manufacturer as input parameters and assuming hydrolysis and precipitation rate are equal, the reaction rate is described using the equation:

$$r_h = r_p = v_{max} \frac{C_s}{K_m + C_s} \tag{10}$$

in which, $r_h$ is the hydrolysis rate, $v_{max}$ is the maximum urease activity in [mol $L^{-1}$ $hr^{-1}$] as provided by the manufacturer's specifications, $C_s$ is the concentration of the substrate urea in [mol $L^{-1}$] and $K_m$ is the half saturation coefficient (affinity constant) in [mol $L^{-1}$].

## 3.3 EXPERIMENTAL STUDY

### 3.3.1 Preparation of Reactive Solution

The reactive solution prepared in this study was based on *Nemati & Voordouw*'s experimental work (2003) and contained 12g (~200 mmol $L^{-1}$) urea ($CO(NH_2)_2$, U5378, Sigma-Aldrich), 30g (~200 mmol $L^{-1}$) calcium chloride dihydrate ($CaCl_2 \cdot 2H_2O$, C3881, Sigma-Aldrich), and 0.1g (~0.01 w%) urease powder (extracted from jack beans, Type III, 26100 [U $g^{-1}$], U1500, Sigma-Aldrich) per liter. DI water was used to prepare the solution. Consequently, the concentrations of both urea and calcium chloride were at a 1:1 molar

ratio and the expected maximum urease activity, $v_{max} \approx 0.078$ [mol-urea $L^{-1}$ $hr^{-1}$]. Unlike *Nemati & Voordouw*'s recipe, the solution did not include milk powder.

### 3.3.2 Microfluidic Chip Experiment

A two-dimensional transparent microfluidic chip (Micronit Microfluidics BV, The Netherlands) was used, which was designed and fabricated to resemble a homogenized circular particle packing (*Mahabadi et al.,* 2016; *Zheng et al.,* 2017). The dimension of the microfluidic chip is 21.3 mm×12.7 mm, and the internal thickness (pore depth) is 50 μm. The microfluidic chip includes 377 circular mono-sized grains with 800 μm of diameter and the size of pore throat between two grains is 140 μm (Figure 3.1a). Figure 3.1b shows the configuration of the microfluidic chip experimental set-up. The microfluidic chip with injection and extraction ports is fixed in a steel holder and placed vertically. Before the first flush, the microfluidic chip was air-filled. The prepared solution was injected into from the bottom inlet. After the injection, both inlet and outlet ports were closed to prevent evaporation and fluid flow. The solution was left to react for 48 hours. The injection-reaction process was repeated 10 times. The volume of injected solution in each cycle was about 0.5 mL, which is significantly larger than the pore volume of the microfluidic chip to ensure the entire system volume would be replaced, including the volume of the tubing and inlet and outlet channels. After each flushing and reaction cycle, the microfluidic chip was flushed with about 0.5 mL of deionized water, to wash out the retained solution before injecting the next batch of EICP solution.

Time lapse digital photography was performed every 10 minutes for the entire reaction process (48 hours each cycle) to continuously monitor the evolution of carbonate

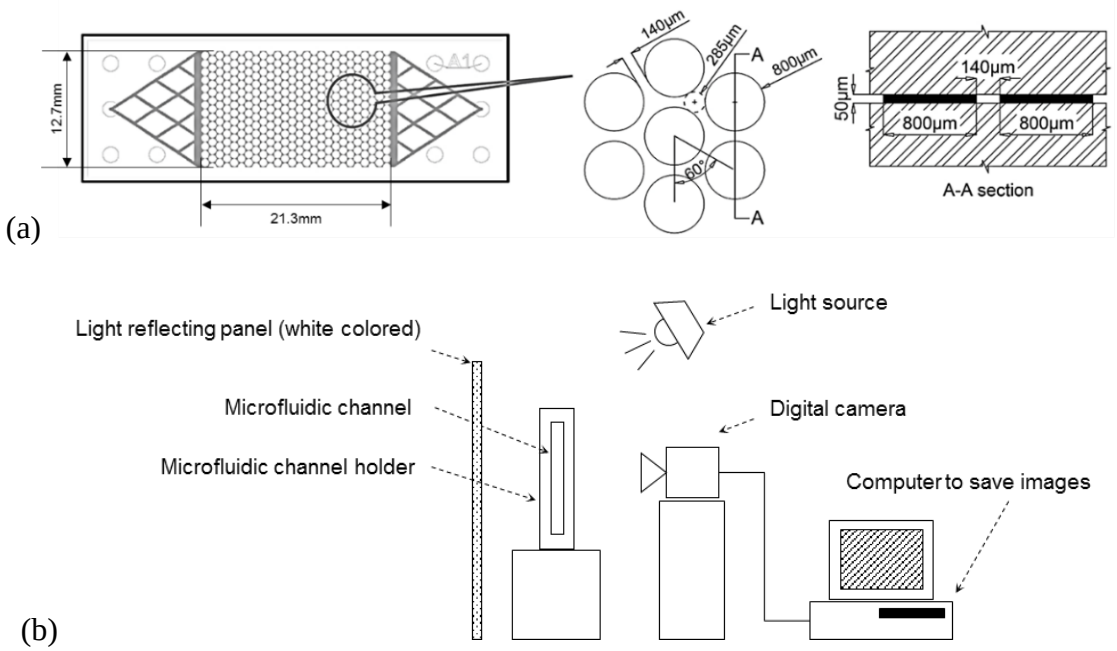


**Figure 3.1.** (a) Geometry of the patterned microfluidic chip (*Mahabadi et al.*, 2016; *Zheng et al.*, 2017), (b) Experimental configuration of the microfluidic chip test

mineral formation within the entire microfluidic chip. A digital camera (D5200, Nikon) equipped with a 60mm micro-lens (AF-S Micro NIKKOR 60mm f/2.8G ED, Nikon) was used to capture the growth of precipitated calcium carbonate minerals in high-resolution images.

### 3.3.3 Image Processing

A comprehensive image processing algorithm was developed using MATLAB (ver. R2017a) to automatically detect and extract the precipitated calcium carbonate crystals from the original images and monitor the precipitation process within the microfluidic chip over time. The proposed algorithm allows for a consistent detection of the boundaries of the different phases, minimizing human error associated with manual detection, thereby improving the reproducibility of the detection process, and significantly reduces the time

for massive image data analysis. Figure 3.2a shows the raw image of the entire microfluidic chip at the end of $4^{th}$ treatment cycle. Figure 3.2b highlights a cropped area of Figure 3.2a including the circular grains, precipitated minerals, and a few air bubbles which were trapped along the sides of the microfluidic chip. It should be noted that during the injection, some air bubbles were also flushed with the injected solution through the microfluidic chip. At the end of the injection, a few air bubbles were trapped in the low accessible pores along the left and right boundaries of the domain. Figure 3.2c shows the final processed image by an automated algorithm including the detected grains (presented in green color), precipitated minerals (presented in red color), and pore space (presented in white color). The detailed steps of the proposed image processing algorithm are explained as follows:

Image binarization: Image binarization is the first prerequisite for multi-phase segmentation, which aims to detect the outlines of all different phases such as grains, minerals, and pores. Acquisition of desired information from a digital image requires the segmentation of objects in it. Every digital color image consists of three $n \times m$ Red, Green and Blue (RGB) matrixes where $n$ and $m$ define the number of pixels in horizontal and vertical directions, and each pixel has a value ranging from 0 to 255. Converting the color image (RGB) to the gray-scale format (intensity image) allows to simply store all the information into a single matrix that facilitates post image segmentation processes. The digital RGB raw images of the microfluidic chip experiment were converted to gray-scale image and then turned into black and white (0 and 1) binary image by applying different intensity thresholds to classify different target objects (grains, minerals, and air pockets). The section below explains the image processing steps applied to detect the three different phases (air pockets, circular grains, and precipitated minerals):

Step 1. Detection of air pockets: In order to identify the location, size and numbers of biominerals, unnecessary objects such as air bubbles and circular grains needed to be identified and removed from the images. Air bubbles were detected and stored in a separate binary image using the *Roberts* edge detection method (1965) (Figure 3.2d). However, in some cases the detected outlines of air bubbles include discontinuities. For this reason, we used another function '*imdilate*' in MATLAB that allows to reconstruct the continuous boundary around the disconnected air bubbles by dilating the boundary pixels (Figure 3.2f). The dilated reconstructed boundaries of bubbles were filled and then contracted to compose bubbles and return their expanded size to the original size. The detected bubbles were later removed from the binary image constructed in step 3 for mineral detection (Figure 3.2j).

Step 2. Detection of circular grains: The *Canny* edge detection method (1986) was applied to obtain the perimetric boundaries of circular grains (Figure 3.2g). This method uses a block to find edges by searching for local maxima of the gradient within the Gaussian filtered image. The Canny method finds two threshold values, a higher and lower threshold, to detect strong and weak edges, and includes the weak edges in the output only when they are connected to strong edges. By applying the Gaussian filter and judging connectivity between weak and strong edges, the Canny method is more likely to remove the noise and detect a wide range of edges with high sensitivity. Thereafter, the '*imfindcircle*' function in MATLAB was employed to find and record the center's coordination and diameter of circular grains (detected grains presented by red circles in Figure 3.2h). However, due to variations of brightness over the grains, the size of detected circles varied. Considering the fact that all the grains have a fixed size (800 μm), the size of the detected circular grains

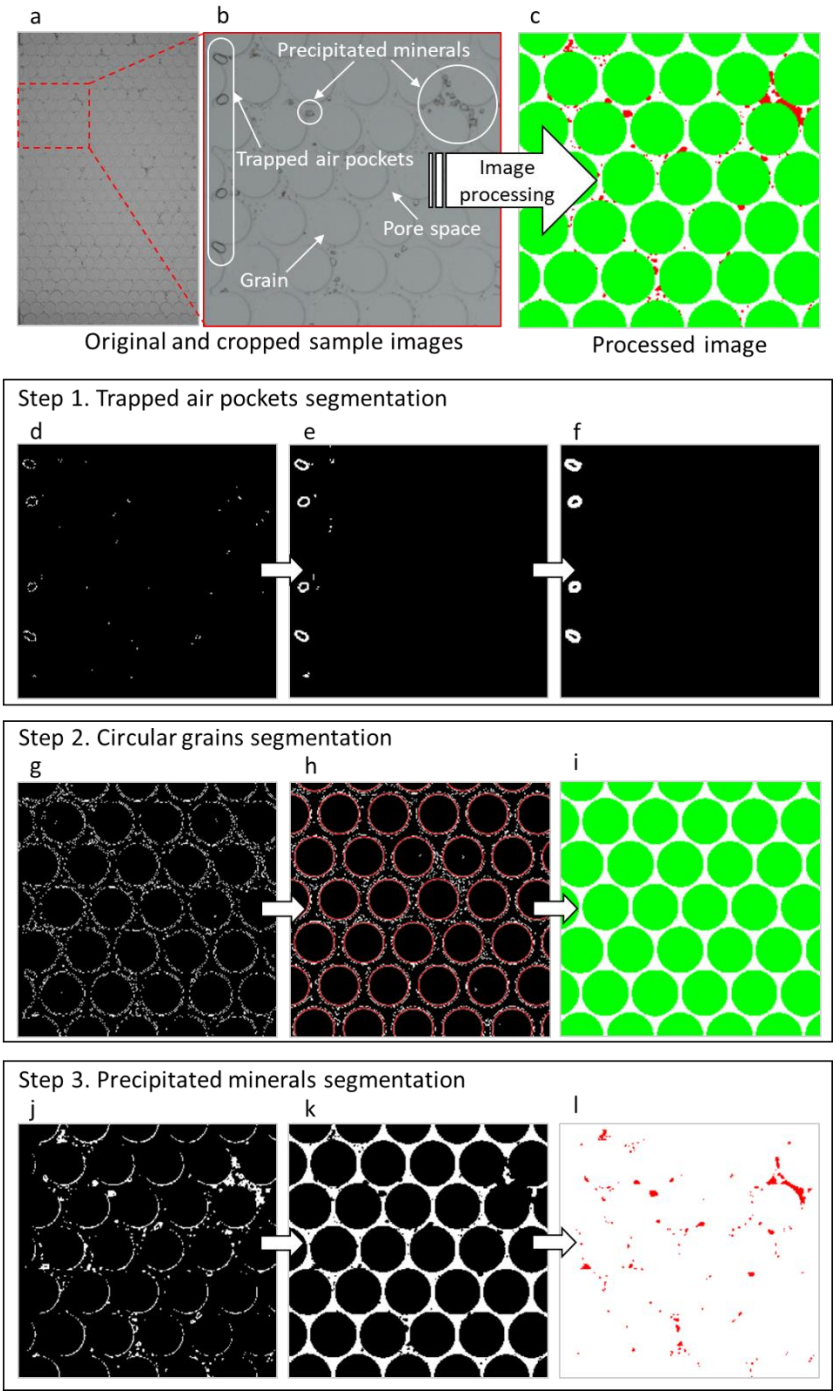


**Figure 3.2.** Phase segmentation performed by the automated image processing (top): (a) Original experimental sample image showing the entire domain of microfluidic chip, (b) Cropped area from the sample image including different phases, (c) Processed image based on the image segmentation. The image processing algorithm mainly consists of three steps (bottom): (d~f) Detection of trapped air pockets; (g~i) Detection of circular grains; (j~l) Detection of biominerals.

was adjusted to satisfy this constraint. Using the detected center and radius, the circular grains were mapped out and converted to a separate binary image (Figure 3.2i).

Step 3. Detection of precipitated minerals: The precipitated minerals have relatively smaller size than the circular grains and air bubbles, so edge detection methods are not proper to find the minerals. In order to detect the precipitated minerals, the gray-scale image was turned into a binary image by using Otsu's method, which automatically selects threshold and replaces all the values above a specified threshold with 1 (white) and all other values with 0 (black) (*Otsu,* 1979). Otsu's method can be readily carried out by using 'imbinarize' function in MATLAB. However, since the gray-scale image contains an illumination gradient, the default Otsu's method produces a very poor result. Moreover, the intensities of some parts of the circular grain boundaries have similar values to those of the mineral boundaries. Therefore, Otsu's binarization method required some modification for precise detection of mineral boundaries. In order to minimize the illumination artefacts, localized thresholding was applied using the 'adaptive' option within the 'imbinarize' function. The 'adaptive' method computes thresholds for each pixel using the local mean intensity of the neighborhood of the pixel. The 'ForegroundPolarity', 'dark' option was used to detect the pixels occupied by mineral boundaries, considering the mineral boundaries have darker intensities than the background values. The threshold in this option can be specified by the 'sensitivity' parameter, which ranges between 0 and 1. A higher sensitivity identifies more pixels as mineral boundaries. Due to illumination changes during the different cycles, the threshold values may vary slightly and needed to be manually selected using a trial and error approach. For the image in Figure 3.2 the 'sensitivity' was determined at 0.54 after trial and error. The resulting image (Figure 3.2j)

still contained boundaries of circular grains. The detected circular grains in the previous step were redrawn, filled (Figure 3.2i) and overwrapped onto Figure 3.2j, then the result was reversed. The reversed image included the circular grains and mineral outlines in black and pores in white but left the inside of some relatively big minerals white. These larger minerals, which were defined by their pixels size (<100) were filled black using the 'bwareaopen' function to obtain Figure 3.2k. By subtracting redrawn and filled grains (Figure 3.2i) from Figure 3.2k, the mineral phase could be generated as a separate phase (Figure 3.2l).

### 3.3.4 Statistical Analysis of the Mineral Phase

Quantitative information of the precipitated biominerals, i.e. the size, number and volume of crystals, were derived from the processed images (Figure 3.2l). In order to determine the individual crystal size, the number of pixels in each crystal were counted to determine the crystal area. Based on the size and resolution of the images, each pixel has the approximate dimensions of 6.5 µm×6.5 µm. The equivalent diameter, $d_{eq}$, of the individual crystals was derived from the total area of pixels ($A_p$) using:

$$d_{eq} = \sqrt{\frac{4A_p}{\pi}} \tag{10}$$

In order to exclude undesirable noises from the results, it was decided to exclude the detected crystals which were 3 pixels or less in size. This noise filtering may cause underestimating the volume of crystals.

The volume and crystal surface area of the individual crystals were calculated in different ways, depending on the assumption of the crystal shape. Assuming crystals had a cylindrical shape and filled up the entire internal thickness of the microfluidic chip, h = 50

[μm], crystals can only grow radially and the crystal surface area, $A_c$ in [μm$^2$], and crystal volume, $V_c$ in [μm$^3$], are calculated using:

$$A_c = \pi h d_{eq} = 100\pi r_{eq} \qquad \text{and} \qquad V_c = 50\pi r_{eq}^2 \tag{11}$$

Alternatively, assuming that crystals have a semi-spherical shape and are attached either to the front or the back of the microfluidic chip, the crystal height varies depending on the equivalent crystal radius. When the radius of a semi-spherical crystal is smaller than the internal thickness of the microfluidic chip, surface area and volume are calculated using:

$$A_c = 2\,\pi r_{eq}^2 \qquad \text{and} \qquad V_c = \frac{2}{3}\pi r_{eq}^3. \tag{12}$$

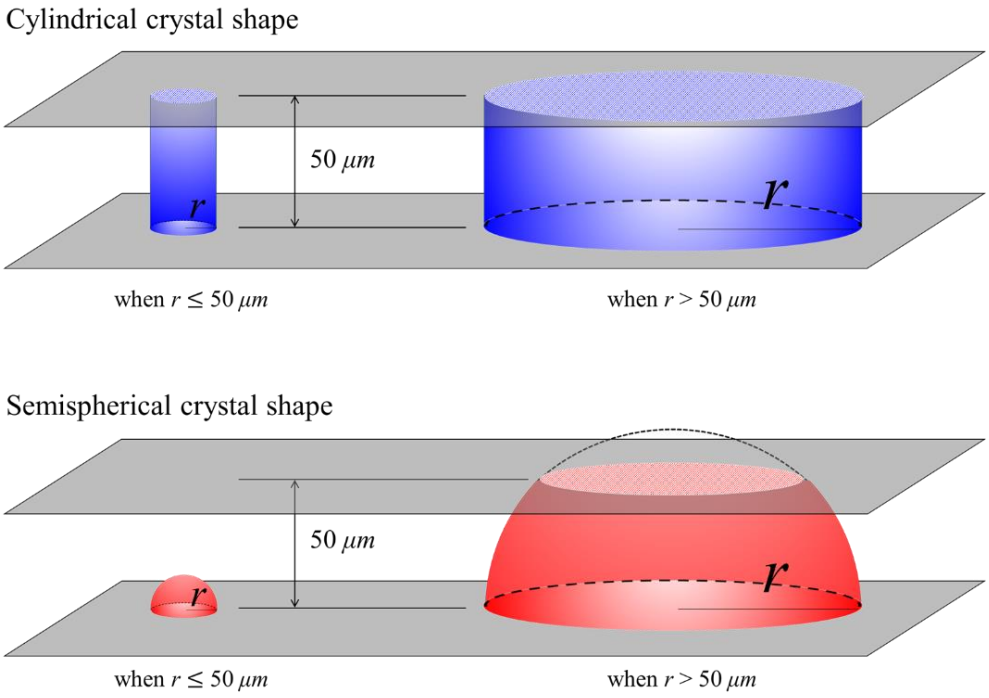


**Figure 3.3.** Two hypothetical shapes of calcium carbonate crystal formation in microfluidic chip

Once the radius of semispherical crystal is bigger than the internal thickness of the microfluidic chip, surface area and volume are calculated using:

$$A_c = 100\pi r_{eq} \quad \text{and} \quad V_c = \pi(50r_{eq}^2 - \frac{50^3}{3}). \tag{13}$$

The two hypothetical shapes are shown in Figure 3.3. The total volume of crystals and total surface area, $A_t$, are obtained by adding up the values for all individual crystals.

## 3.4 RESULTS AND DISCUSSION

Figure 3.4 shows the results of image analysis. On the left side the volume of crystals is plotted as a percentage of the initial pore volume of the untreated microfluidic chip as a function of time assuming cylindrical crystal shapes. As results of 10 cycles of EICP treatment the total volume of crystals filled up about 8.25 % of the pore space. The change in crystal volume per cycle varied. From 0.80 % in the first treatment cycle, it reached a maximum of 1.41 % in the 4$^{th}$ cycle and then declined to 0.29 % in the 10$^{th}$ cycle. The results of 2$^{nd}$ and 8$^{th}$ treatment cycles are not included as the images of these cycles were not sharp and could not be processed properly. The repetitive shutter operations of the digital camera during these cycles caused a slight movement of the test setup and a loss of focus of camera, which demonstrates that even a small disturbance during the image capturing process may critically affect the quality of the output images. In order to prevent this experimental issue, all imaging equipment including the camera, microfluidic chip and light source are required to be completely fixed with a rigid frame during the experiment.

During each treatment cycle, the volume of crystals increased until a threshold was reached, after which no more crystal volume change was recorded. During the 1$^{st}$ cycle a lag phase occurred, which lasted for ~5 hours (red hollow circles in Figure 3.4), after which

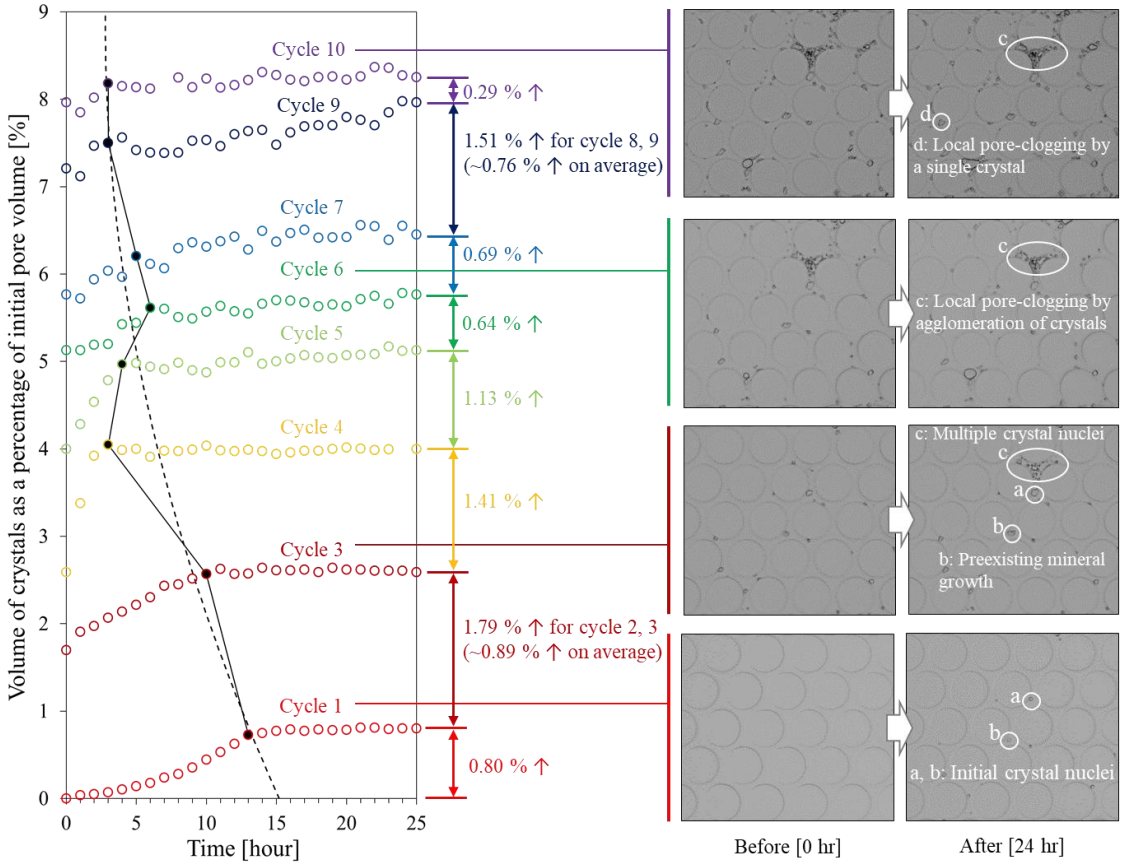


**Figure 3.4.** Volume of crystals as a percentage of initial pore volume with time for each cycle of treatment assuming cylindrical crystal shape (left). Highlighted area of the experimental images before and after EICP treatment for cycle 1 (red), 3 (brown), 6 (green), and 10 (purple) (right)

the first crystals were detected. The volume of crystals gradually increased until about 14 hours, after which no further significant change in crystal volume was observed. The lag phase in the 1st cycle could be interpreted as an induction time in which the supersaturation first needs to increase sufficiently in order to trigger crystal nucleation. Another reason for the observed lag phase could be that the initial crystals were too small to be detected at the given image resolution. In subsequent cycles the time to reach the end of reaction, which is indicated by the black-dashed line shown in Figure 3.4, decreased, which indicates that

the bulk precipitation rate gradually increased with increasing number of cycles. Most significant change in bulk precipitation rate was observed within the first four cycles of treatment. After 4$^{th}$ cycle, the precipitation rate remained approximately constant. The increase in bulk precipitation rate may be due to the presence of already existing crystals, which grow or stimulate heterogeneous nucleation and facilitate immediate precipitation, skipping the induction and nucleation phase. The precipitation rate can also be affected by differences in urease activity, substrate distribution, or amount of remaining substrates or enzymes from the previous cycles of treatment.

A detail of the original experimental images for the 1$^{st}$, 3$^{rd}$, 6$^{th}$ and 10$^{th}$ cycle is shown on the right side of Figure 3.4. These images illustrate the formation process of biominerals within subsequent treatment cycles. During the initial cycles of treatment, nucleation of new crystals is expected to occur. Small nuclei may have settled in the liquid, but were too small to detected. As soon has the crystals reached an observable size no movement of crystals was observed. Examples of new crystal occurrences are highlighted with labelled white circles (labels *a* and *b*) for the 1$^{st}$ cycle of treatment. By tracking crystals, *a* and *b*, it is clear that individual crystals gradually grow as the cycles of treatment increase (label *a* and *b* from cycle 1 to 3). In some cases, the growth of crystals leads to pore clogging. This could either be the result of an agglomeration of multiple crystals (label *c*), or due to a single large crystal (label *d*). Pore clogging could block pore connectivity and affect the distribution of substrates and resulting precipitates in subsequent flushes, which can potentially explain the variations in engineering properties of treated soils reported in the literature.

The size distribution of crystals after each cycle of treatment is presented in Figure 3.5a. In order to construct these curves, crystals were categorized into bins according to their equivalent diameter, with each bin representing a 5 μm range. As the objects with a size with 3 pixels or less were filtered out by the image processing, the counting started at 15 μm, which represents the bin between 15~20 μm. The crystal size distribution typically revealed a (truncated) exponential distribution, which gradually changed with multiple cycles of treatment. At the 1$^{st}$ cycle of treatment, the range of crystal sizes covered a relatively narrow range of equivalent diameters (15~105 μm). Upon subsequent flushes the variation in crystal size became wider reaching 20~455 μm at the 9$^{th}$ cycle of treatment. Besides an increase in size, the number of crystals also increased with multiple cycles of treatment, which implies that nucleation of new crystals and growth of existing minerals took place simultaneously throughout each cycle. The number of crystals within the range of 20~60 μm increased most significantly from the 1$^{st}$ cycle to 5$^{th}$ cycle, which confirms that nucleation of new crystals is most dominant within the first five cycles of treatment. After the 5$^{th}$ cycle, the predominant biomineralization mechanism is the growth of pre-existing crystals.

The total number of crystals as shown in Figure 3.5(b) and Table 3.1 increased mostly within first five cycles, particularly in the 1$^{st}$, 4$^{th}$ and 5$^{th}$ cycle. In the 6$^{th}$ and 7$^{th}$ cycle the number of crystals did not significantly change, whereas in the 9$^{th}$ and 10$^{th}$ cycle the total number of crystals increased again, but the increase in the number of crystals was smaller than in earlier cycles. This noticeable change in cumulative number of crystals affirms that for all cycles of treatment the precipitation mechanism involves both nucleation and growth. The results of statistical analysis were confirmed by the checking

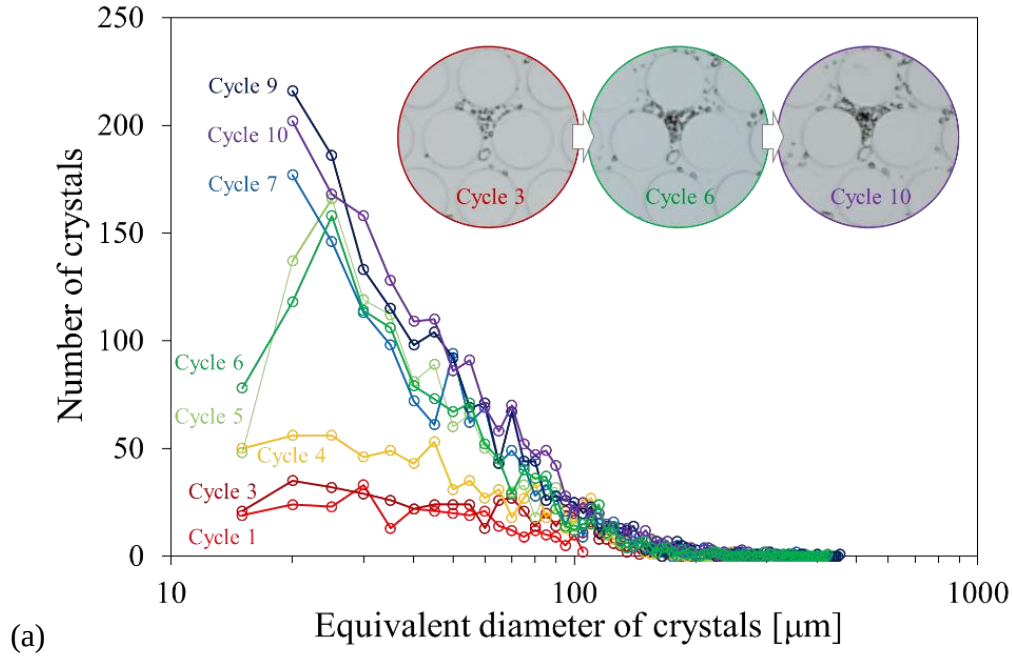


(a)

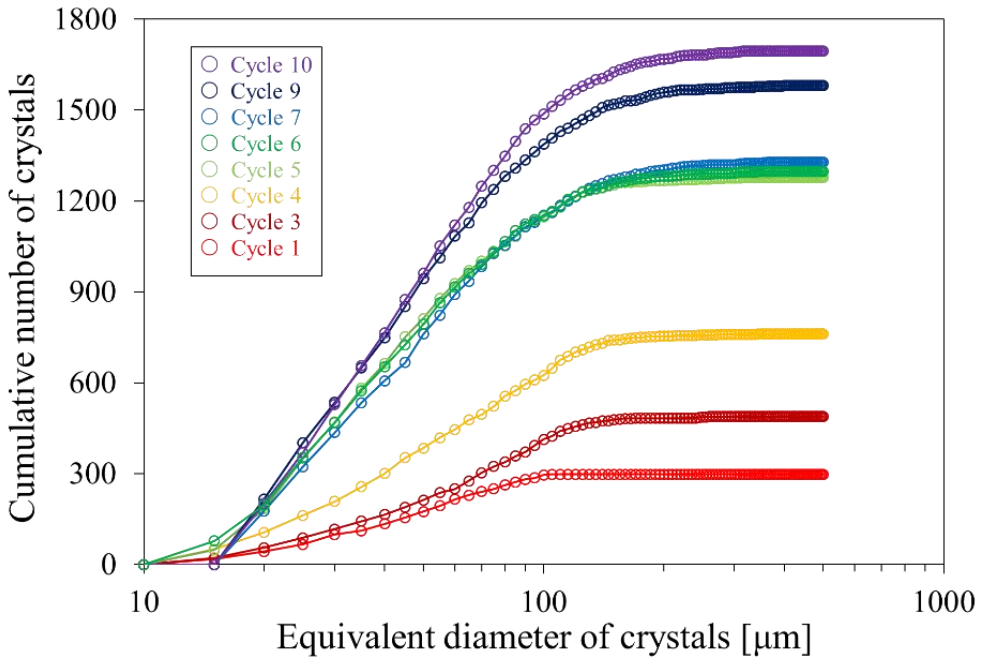


(b)

**Figure 3.5.** (a) Crystal size distribution at different flushing cycles and crystal formation-growth observation within the highlighted area of microfluidic chip (Right upper), (b) Cumulative number of crystals for different cycles of treatment

the original experimental images (right upper corner images in Figure 3.4(a). The image representing cycle 6 (green circle), clearly shows a number of new crystals are formed compared to the image of cycle 3 (red circle), whereas the image of cycle 10 (purple circle), shows that most of crystals have grown compared to cycle 6, but the number of newly formed crystals is less. A reduction of the increase in number of crystals per cycle would be expected considering that pre-existing crystals formed in previous cycles would stimulate heterogeneous nucleation or allow for crystal growth. Secondly, just like the total volume of crystals, the increase in number and size of crystals in each cycle would be affected by the accessibility of pore space when flushing substrate solution. After 5 cycles of treatment, some areas in the microfluidic chip become completely filled by precipitated biominerals, locally clogging the pores and creating inaccessible zones to the substrate solution, which would limit the growth or formation of new crystals in zones affected by those clogged regions.

Comparing the results with the numerical simulations showed several discrepancies. First, the increase in crystal volume for some of the cycles was significantly higher than theoretically possible when assuming cylindrical crystal shapes, particularly for cycle 4 (1.41 %) and 5 (1.13 %). Also, the total volume of crystals after 10 treatment cycles (8.25 %) was higher than expected. Simple mass and balance calculations indicate that for initial urea and calcium concentrations of 0.2 [mol $L^{-1}$] and assuming complete conversion the maximum crystal volume increase is 0.74 % of the initial pore volume. Considering that in each treatment cycle the pore volume is reduced by the volume of crystals, the theoretical increase in crystal volume reduces slightly each cycle reaching 0.69 % in the $10^{th}$ cycle. As a result of pore volume reduction, the total cumulative crystal

volume after 10 cycles is expected to reach 7.15 % instead of 7.4 % when assuming a fixed pore volume, which was confirmed by the results of the simplified model simulations shown in Figure 3.6.

The crystal volume appeared to be significantly affected by the assumption that the precipitated minerals have a cylindrical shape and completely fill up the internal depth of microfluidic chip. Considering that smaller crystals may not fill up the entire depth of microfluidic chip, the assumption of cylindrical crystal shape may overestimate the crystal

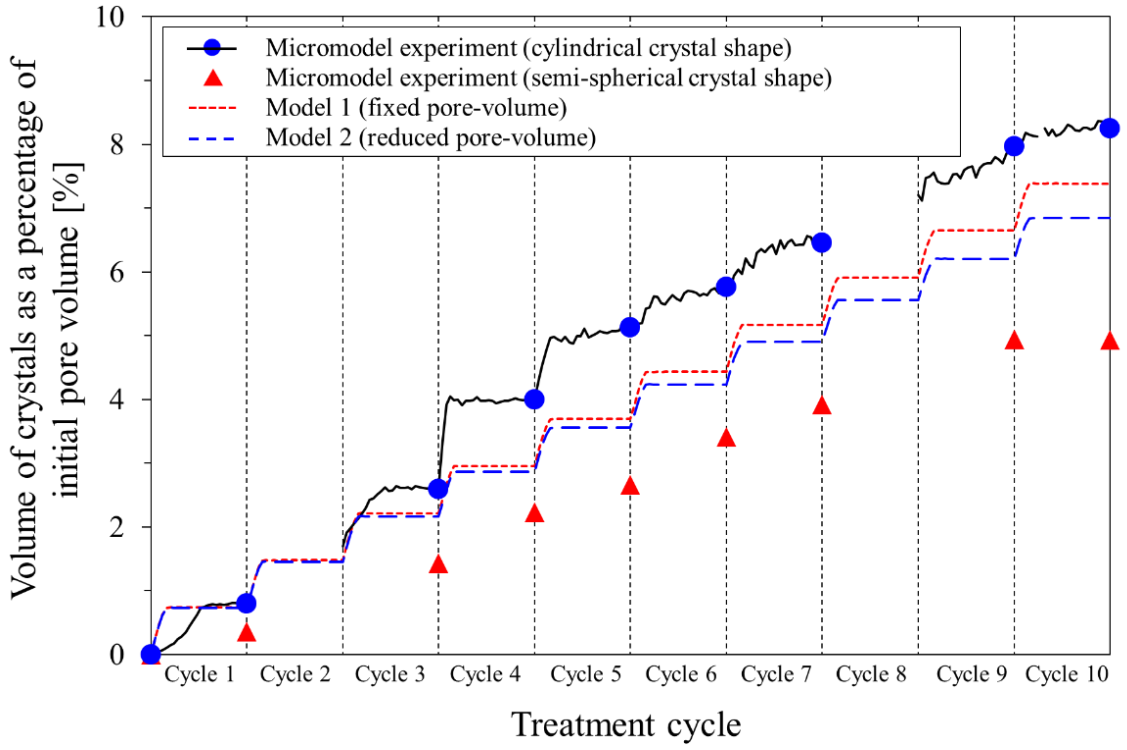


**Figure 3.6.** The estimated cumulative volume of crystals with increasing number of cycles based on the micromodel experiment using either cylindrical or semi-spherical crystal shape and the simulated cumulative volume of crystals based on the injected volume and concentrations of substrates and enzymes in the reactive solution, assuming either a fixed pore volume (model 1) or pore volume reduction as a result of precipitation (model 2)

volume. Calculating crystal volume assuming a semi-spherical crystal shape using equations 12 and 13 resulted in cumulative crystal volume that was on average 30 % smaller compared to the values for cylindrical crystals. This difference may explain why the calculated volume increase during cycle 4 and 5 in Figure 3.4 was larger than theoretically possible. Particularly, because during these cycles a large increase in the amount of new crystals were observed with relatively small sizes. The calculated cumulative crystal volume for semi-spherical crystal shapes was even lower than the results from the numerical model simulations. The difference between the model predictions and experimental observations assuming semi-spherical crystal shapes, could be due to the local pore clogging, which creates zones within the pore volume, inaccessible for convective supply of substrates and reduces the mobile pore volume, which causes a decrease of the amount precipitation. Further analysis on the effect of local pore clogging on substrate product distribution and porosity and permeability relationships in relation to EICP is required and currently being investigated. Other explanations for the differences between observed and predicted volumes may be the formation of alternative types and shapes of crystals or observation bias related to the limitations of the set-up and image processing and analysis procedure, which is discussed later.

Table 3.1 provides a summary of the quantitative analysis of the statistical results, assuming either cylindrical or semi-spherical crystal shapes. The average bulk precipitation rate was calculated by dividing the amount of moles of $CaCO_3$ by the total time to reach full conversion (indicated by the black dots in Figure 3.5). The average bulk precipitation rate was in most cases lower than predicted, except for cycle 4 assuming cylindrical crystal shape. Based on the amount of enzymes added and the specifications of the manufacturer

a maximum urease activity of 0.078 [mol $m^{-3}$ $hr^{-1}$] was expected. Similarly, *Nemati & Voordouw* (2003) or *Whiffin et al.* (2007) found that precipitation rates can be significantly lower than expected. The difference between the measured and expected precipitation rates could be due to various inhibition factors, as discussed in the theoretical background, but in this study inaccuracies in the calculation of cumulative crystal volume and observation bias could contribute to this error. For example, part of the lag phase in the first cycle could be due to the fact that the initial crystals were still too small to be detected at the given image resolution. During the later flushes the average precipitation rate may decrease as a result of local clogging, which reduces the available pore volume for convective supply of new substrates and consequently results in a lower increase in crystal volume.

Supersaturation was calculated following equation 9 using either a second (*S2* with $n = 2$) or first order kinetic model (*S1* with $n = 1$) in which the average bulk precipitation rate and total crystal surface area were used as an input. Total crystal surface area was

**Table 3.1.** The bulk precipitation rate, cumulative crystal surface area, supersaturation, increase in number of crystals, and nucleation rate for each treatment cycle

| Cycle | Cylindrical crystal shape | | | | Semi-spherical crystal shape | | | | Observation | |
|---|---|---|---|---|---|---|---|---|---|---|
| | $r_p$ [kmol $m^{-3}$ $h^{-1}$] | $A_T$ [$mm^2$] | *S2* [-] | *S1* [-] | $r_p$ [kmol $m^{-3}$ $h^{-1}$] | $A_T$ [$mm^2$] | *S2* [-] | *S1* [-] | *N* [-] | *'dN/dt'* [$m^{-3}$ $s^{-1}$] |
| 1 | 0.015 | 2.16 | 77.8 | 5899 | 0.008 | 1.3 | 71.3 | 4945 | 298 | 0.0064 |
| 3 | 0.024 | 4.82 | 65.7 | 4182 | 0.015 | 3.6 | 59.4 | 3413 | 95 | 0.0026 |
| 4 | 0.132 | 7.24 | 125 | 15528 | 0.073 | 5.4 | 108.4 | 11539 | 273 | 0.0253 |
| 5 | 0.066 | 10.1 | 75.7 | 5578 | 0.029 | 6.6 | 62.4 | 3768 | 517 | 0.0359 |
| 6 | 0.022 | 10.7 | 42.8 | 1747 | 0.034 | 7.2 | 64.3 | 4007 | 20 | 0.0009 |
| 7 | 0.024 | 11.5 | 43.1 | 1776 | 0.027 | 7.9 | 55.1 | 2928 | 30 | 0.0017 |
| 9 | 0.026 | 13.8 | 41.4 | 1633 | 0.047 | 9.6 | 65.5 | 4166 | 127 | 0.0118 |
| 10 | 0.020 | 15.0 | 34.6 | 1127 | -0.001 | 10.4 | <1 | <1 | 113 | 0.0105 |

calculated using either equation 11 for cylindrical crystal shape or equation 12 and 13 for semi-spherical crystal shape. The nucleation rate, *'dN/dt'*, was determined by dividing the increase in the number of observable crystals in each cycle, *N*, by the reaction time. It must be emphasized that the resolution of the images does not allow to observe the actual crystal nuclei as these would be far too small to be detected. Hence the calculated '*dN/dt*' does represent the increase in number of crystals and not an actual nucleation rate. However, considering that each new crystal must have nucleated, the number of crystals may be indicative for the amount of nuclei formed in each treatment cycle.

Figure 3.7 presents the calculated 'nucleation rate' as a function of the calculated supersaturation for the different selected model scenarios and compares them with the theoretically expected nucleation rates based on classical nucleation theory according to equation 7 for different values of interfacial tension based on the values provided by *Dalas et al.* (1988), *Liouliou et al.* (2007) and *Söhnel & Mullin.* (1982). The results of this comparison show that the calculated supersaturation is relatively high, particularly when considering first order growth kinetics (*S1*). The fact that in each cycle new crystals were observed indicates that supersaturation must have been sufficiently high to allow for spontaneous nucleation. However, at the calculated supersaturations higher nucleation rates would be expected.

Besides observation bias which are discussed later the low 'nucleation rates' (or high supersaturations) may due to inhibition of crystal nucleation. A minuscule amount of additives can significantly inhibit both of the nucleation and growth of calcium carbonate crystals (*Bernard et al.,* 1992; *Lin et al.,* 2005; *Matty & Tomson,* 1988; *Söhnel & Mullin,* 1982). Presence of dissolved organic matter may inhibit growth, but favor nucleation

(*Lebron & Suarez*, 1996). Proteins may also act as chelating compounds, lowering the concentration of free calcium ions, available for precipitation (*Almajed et al.*, 2019).

Since, the substrate solutions used in EICP experiments contain enzymes (i.e. organic polymers) of which the interaction with ions is not fully understood and precipitation in porous media takes place in a confined space, with limited convective mixing conditions and in presence of heterogeneous surfaces. Hence, ion concentrations vary in space and time and often cannot be measured at pore scale. Therefore, for EICP both measurements and direct predictions of the supersaturation and the resulting precipitation characteristics should be interpreted with caution.

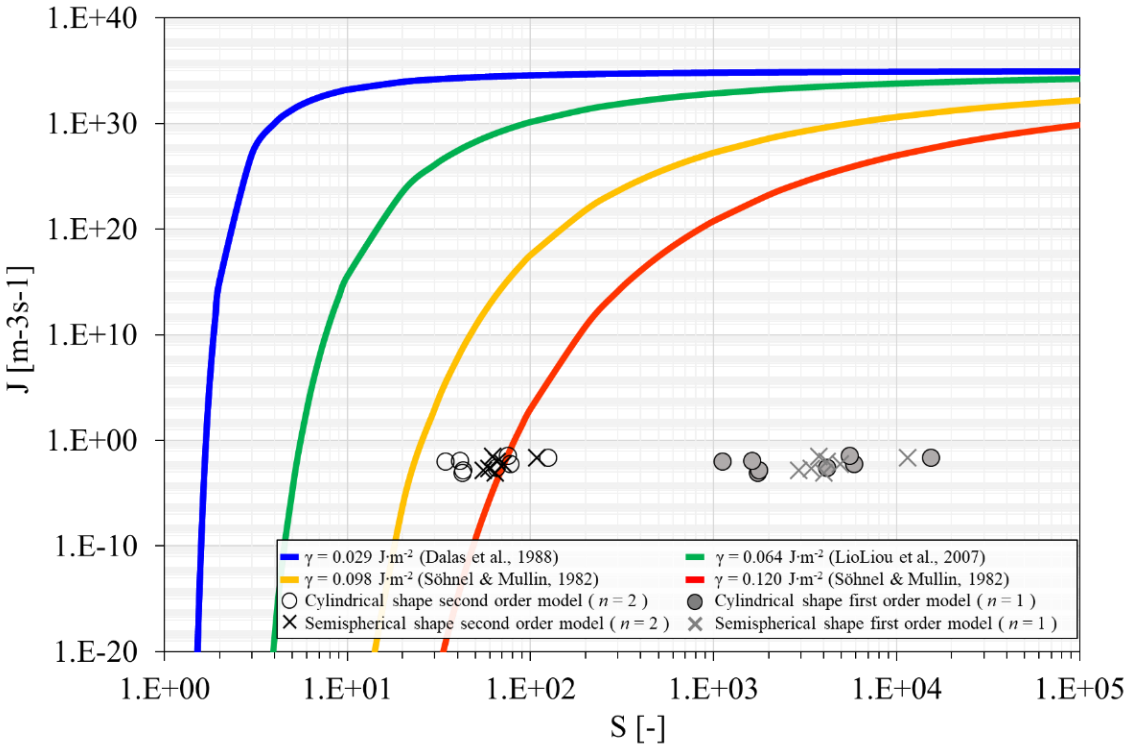


**Figure 3.7.** The theoretical and experimental nucleation rate for homogeneous nucleation of calcite crystals in S-J plot for various temperature and surface tension

Quantitative interpretation of the results in this study is affected by significant observation bias and limitations in the set-up or image analysis. Firstly, the resolution of the images and the accuracy of the image analysis algorithm are limited. The resolution of the imaging setup used in this study does not allow to identify the small crystals or crystal nuclei. Hence, fluctuations in the volume, size and number of crystals and derived parameters may be due to the inaccuracy of the processed images. Secondly, during the course of the experiment more air bubbles got trapped during the injection of substrates, partly attributed to local clogging by the increased number and amount of biominerals. As a result, it became difficult to separate air bubbles from minerals, as the bubble-liquid meniscus were overlapping with crystal boundaries.

Another type of observation bias relates to the definition of nucleation versus growth. Crystal growth may occur as individual calcium and carbonate molecules are incorporated in the crystal lattice, but also by heterogeneous nucleation in which new individual crystals start growing on existing crystal surfaces. Once multiple crystals agglomerate, they cannot be distinguished as individual crystals as the image processing and quantitative analysis treats the agglomerated crystals as a single particle. As a result, the analysis may underestimate the number of individual crystals and the cumulative surface area. The resulting supersaturation and nucleation rate may also be underestimated.

Finally the actual crystal shape may differ from the assumed cylindrical or semi-spherical crystal shapes, which is illustrated in Figure 3.8 showing a microscopic image of a section of the microfluidic chip. The actual crystal shape depends on type of mineral, calcite, vaterite or aragonite and the precipitation conditions. Vaterite typically shows spherical or ‘cauliflower’ crystal shapes, while calcite typically forms single or clusters of

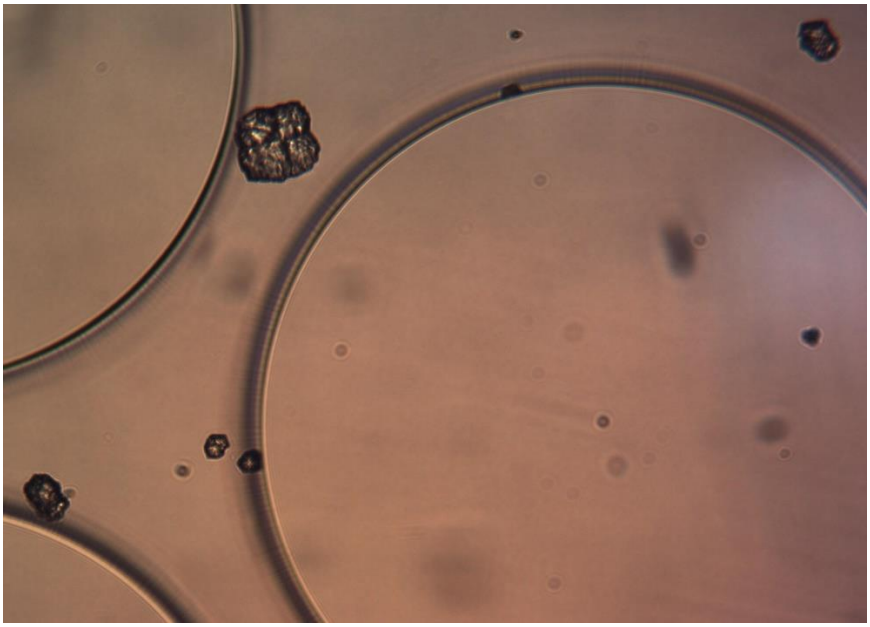

**Figure 3.8.** Microscopic image of a section of the microfluidic chip, illustrating the actual shape and surface area of the precipitated crystals

rhombohedral crystals (e.g. *Al-thawadi & Cord-Ruwisch*, 2012; *van Paassen*, 2009), but also dendritic calcite or aragonite crystal shapes have been observed (e.g. *Pham et al.*, 2016). These different crystal shapes typically increase the surface area, which lowers the calculated supersaturation.

## 3.5 CONCLUSIONS

Enzymatically induced calcium carbonate precipitation (EICP) by urea hydrolysis has been studied using a microfluidic chip experiment. The reactive solution was flushed 10 times through a microfluidic chip and was allowed to react for 48 hours. The precipitation of $CaCO_3$ minerals was monitored by time sequential images. An image processing algorithm was developed to analyze the experimental images, assess the

characteristics of the biominerals, and gain insight in the precipitation mechanisms and the kinetics of crystal nucleation and growth.

Despite a limited resolution, the cumulative crystal volume and bulk precipitation rate could be determined and corresponded reasonably well with values predicted with a simplified numerical model. The assumed crystal shape in the image analysis procedure significantly affected the calculated volume of crystals. Assuming a cylindrical crystal shape overestimates the crystal volume, particularly when the crystals are smaller than the internal thickness of the microfluidic chip. Assuming a semi-spherical crystal shape, the cumulative crystal volume and bulk precipitation rate, were lower than expected and gradually decreased with an increasing number of cycles. This decrease can partly be attributed to local pore clogging, which reduces the mobile porosity allowing a lower amount of substrate solution to be retained in the pore volume.

Also, the amount and size distribution of crystals could be determined. The calculated supersaturation was relatively high, which could explain the fact that new crystals were observed in each treatment cycle. However, when comparing the results with classical nucleation theory, it was found that for the calculated supersaturation the observed 'nucleation rate' was lower than expected. The difference between theoretical predictions and experimental data emphasizes the difficulty to accurately predict the pore-scale characteristics of biominerals directly. Still, this study has shown that despite its limitations, microfluidic chips are useful tools to assess the pore scale characteristics of precipitated minerals in porous media. The proposed procedure can be used to optimize MICP or EICP treatment strategies or validate numerical models, by analyzing the effect of different substrate and enzyme concentrations and quantify relationships between pore

scale crystal characteristics and continuum scale 'engineering' parameters of porous media, such as porosity and permeability.

## Acknowledgments

Work described herein was supported in part by the National Science Foundation (NSF) Engineering Research Center program under the grant numbered ERC-1449501. Any opinions, findings and conclusions or recommendations expressed in this material are those of the authors and do not necessarily reflect those of the NSF. Authors would like to thank Prof. Tim Ginn and two anonymous reviewers for their critical feedback, which enabled to improve the manuscript. The datasets generated and analyzed during the current study, including the MATLAB scripts will be available in the Open Science Framework (OSF), at https://osf.io/kprqd/.

# CHAPTER 4

# BIOMINERAL FORMATION IN POROUS MEDIA: A HYBRID EXPERIMENT-NUMERICAL STUDY

This chapter will be submitted to *Advanced in Water Resources Journal* as Mahabadi, N., Kim, D., Wang, L., van Paassen, L. A. "Evolution of Porosity-Permeability Relationships for Biomineral Precipitation in Porous Media: A Hybrid Experimental-Numerical Approach."

## ABSTRACT

The last decade has seen an exponential growth in research on engineering applications of microbially induced carbonate precipitation particularly in soil stabilization, subsurface remediation of toxic metals and radionuclides, and sealing of porous and fractured media to enable $CO_2$ storage. In this study, pore-scale characteristics of biogeochemically induced carbonate precipitation and its impact on the hydraulic properties of porous media are studied using a hybrid experimental-numerical approach. A two-dimensional transparent microfluidic chip is employed to visualize the biomineralization process at pore-scale. A reactive solution is flushed in 10 cycles through the microfluidic chip. During each cycle the formation of calcium carbonate crystals is monitored by time sequential images. An image processing algorithm is developed to analyze the experimental images and detect the carbonate minerals within the pore space. Based on the processed images, a finite element CFD model is developed using COMSOL Multiphysics to explore the evolving hydrodynamics of transported solutes in the treated

pore space. The numerical simulations verified that biomineral precipitation reforms the pore structure morphology, porosity, and permeability of porous media. Local pore-clogging by precipitated carbonate minerals leads to the development of isolated pore clusters and impermeable zones. The evolution of impermeable zones results in the formation of preferential flow paths towards the mobile zones, which also affects the mineral precipitation patterns in multi-cycle treatment strategies. The results suggest that simple porosity-permeability reduction relationships dramatically overestimate the permeability in biomineral precipitated sediments. The distinction between porosity and mobile porosity must be taken into consideration when predicting the hydraulic fields in biochemically altered sediments. The results of this study can be used to validate numerical models, which aim to predict the impacts of biomineralization on the permeability and fluid flow regimes in sediments.

## 4.1 INTRODUCTION

Microbially or Enzymatically Induced Carbonate Precipitation (MICP/EICP) has attracted great interest in recent years for its potential in geo-environmental and geotechnical engineering applications. MICP can be exploited for various engineering applications, e.g. improving soil strength (*DeJong et al.,* 20010; *Whiffin et al.,* 2007; *van Paassen,* 2009), entrapping groundwater contaminants (*Ferris et al.,* 2004, *Fujita et al.,* 2004), enhancing oil recovery (*Cunningham et al.,* 2009), and increasing storage security of $CO_2$ (*Cunningham et al.,* 2011).

Biogeochemistry and hydrodynamics are coupled processes in MICP, and include non-linear reaction kinetics, multi-phase transport of solutes, micro-organisms and solids,

biomass growth and decay and mineral precipitation, which result in varying properties of the liquid phase, such as density and viscosity and of the pore structure, such as porosity and permeability (*Al Qabany et al.,* 2012; *Fauriel & Laloui,* 2012; *Hommel et al.,* 2016). Due to this complexity, numerical modeling plays a critical role in quantifying the interplay between these coupled processes and properties as well as predicting the performance of MICP for different engineering applications.

Several numerical models have been developed in the past years to simulate MICP performance. They simulate MICP at different scales, including large-scale (*Cuthbert et al.,* 2012; *van Wijngaarden et al.,* 2011, 2012, 2013), meter-scale (*Nassar et al.,* 2018), column-scale (*Ebigbo et al.,* 2012; *Martinez et al.,* 2014), and pore-scale (*Qin et al.,* 2016). Different approaches have also been used including pore network models (*Qin et al.,* 2016), finite element or finite difference methods in which fluid flow can be modelled by using either Navier-Stokes equation (*Helmig et al.,* 2013) or Darcy's models at continuum scale (*Ebigbo et al.,* 2012).

The biogeochemical processes can be modelled with different levels of complexity. Simplified models generally adopt a single chemical reaction equation (*Cuthbert et al.,* 2012; *Hommel et al.,* 2015; *Qin et al.,* 2016), while more advanced models include geochemical speciation reactions of multiple solute species. These models often use specific geochemical speciation software such as PHREEQC (*Charlton & Parkhurst,* 2011; *Parkhurst & Appelo,* 2013), ORCHESTRA (*Salek et al.,* 2016; *Ubbink,* 2013), and TOUGHREACT (*Barkouki et al.,* 2011). Each of these packages uses geochemical databases, which include information about section equilibrium reactions. More advanced models may include kinetics of biomass growth or carbonate mineral nucleation and

growth at different levels of complexity (*Cunningham et al.,* 2009; *Fauriel & Laloui,* 2012; *Hommel et al.,* 2016; *Mitchell & Ferris,* 2006; *van Paassen,* 2009).

Continuum-scale models are popular due to their potential to simulate real world field applications. However, the efficiency of continuum-scale models relies on the up-scaled properties of porous media. In this context, continuum-scale models use an averaging concept in which the pore-scale characteristics of porous media such as pore size, shape and geometry and surface characteristics can be substituted with generalized up-scaled properties, such as permeability or porosity. Using up-scaled parameters avoids the need for a detailed description of the fluid–solid interface at the expense of losing information regarding pore-scale details.

Mineral precipitation via MICP reduces porosity and permeability. Numerical models commonly employ methods, which relate changes in the permeability to changes in porosity. A broad variety of porosity-permeability relations can be found in the literature that each are derived under specific circumstances and assumptions (*Hommel et al.,* 2018). Kozeny-Carman equation is one of the most widely accepted derivations of permeability as a function of the characteristic of porous media. This equation was originally proposed by *Kozeny* (1927) and was then modified by *Carman* (1937) to become the Kozeny-Carman equation. Based on the Kozeny-Carman equation the permeability $k$ of a porous system can be expressed in terms of the intrinsic properties of the medium as:

$$k = \frac{\emptyset^3}{2\tau(1-\emptyset)^2 a_v^2} \tag{1}$$

where the permeability $k$ is calculated using the porosity $\emptyset$, tortuosity $\tau$, and the specific surface area $\alpha_v$ of the porous medium. While the permeability in the Kozeny-Carman theory relies on porosity, specific surface area, and tortuosity, until recently only

the porosity could be measured relatively easily in practice, which left the tortuosity and surface area as substantially indeterminate quantities.

In addition to the Kozeny-Carman type of relations, power law relationships are commonly used to estimate porosity-permeability changes (*Aharonov et al.,* 1997; *Bear*, 1988; *Bernabé et al.*, 2003; *Carroll et al.*, 2013; *Clement et al.,* 1996; *Civan*, 2001; *Colón et al.*, 2004; *Doyen*, 1988; *Garing et al.*, 2015; *Hao et al.*, 2013; *Knapp and Civan*, 1988; *Luhmann et al.,* 2014; *Luquot et al.*, 2014; *Luquot & Gouze*, 2009; *Menke et al.*, 2015; *Noiriel et al.*, 2004, 2005; *Pereira Nunes et al.*, 2016; *Smith et al.,* 2013; *Vandevivere et al.*, 1995; *Zhang et al.*, 2015). In power-law type of relations, the change of permeability is related to changes in porosity, by using a fitting factor, $\eta$:

$$\frac{k}{k_0} = \left(\frac{\phi}{\phi_0}\right)^{\eta} \tag{2}$$

where the fitting factor, $\eta$, is an empirical value that can be determined from the available experimental data. However, the reported values for $\eta$ vary significantly with regards to the nature of bio-geochemical processes (e.g. biomineral precipitation or dissolution, biomass accumulation) and the pore-scale characteristics of the porous medium (*Bernabé et al.*, 2003). Despite the convenience of using a single fitting parameter to determine the changes in permeability, power law equations are often criticized, as they are not precisely representing the complex biogeochemical processes and the related changes of the porous media characteristics.

For MICP or EICP the change in the overall porosity can be easily estimated based on the volume of product formation via the biochemical reaction stoichiometry. However, the characteristics of the precipitated minerals, such as the crystal size, shape, amount and spatial distribution, may vary as a result of the imposed process and environmental

conditions (*El Mountassir et al.,* 2018; *Kim et al.*, under review; *van Paassen,* 2009). Variations in crystal characteristics, including size, shape and spatial distribution, may affect the results. However, not all the pore space contributes to flow; the most obvious example of this being isolated pores. Although, the prediction of effective porosity contributing to the fluid flow is challenging. To determine the impacts of biogeochemical processes on the changes in pore space geometry and associated hydrodynamics, pore-scale modeling can be useful. The aim of this study is to gain insight about the impacts of biomineralization on the evolution of pore structure and associated porosity-permeability relationships using a pore-scale hybrid experimental-numerical approach. A reactive solution, which results in enzymatic induced carbonate precipitation is flushed 10 times through a microfluidic chip, while the mineral formation is monitored by time sequential images. An image processing algorithm is developed to analyze the experimental images and detect the carbonate minerals within the pore space (*Kim et al.,* under review). Based on the processed images, a finite element CFD model is developed using COMSOL Multiphysics to explore the evolving hydrodynamics of the treated porous media, its impacts on the transport and distribution of substrate solution through the porous domain and the relationships between mineral precipitation, porosity and permeability. The results of this work highlight the need of micro-scale studies of bio-geochemical processes in porous media and provide guidance to interpret and scale-up the behavior of biogeochemical processes and evaluate the performance of MICP or EICP at continuum scale and determine the flow fields in biomineral treated soils, particularly in multiple treatment strategies.

## 4.2 MICROFLUIDIC CHIP EXPERIMENT

A two-dimensional transparent microfluidic chip (Micronit Microfluidics BV, Netherlands) was designed and fabricated to resemble a homogenized circular particle packing. The dimension of the microfluidic chip is 21.3 mm×12.7 mm, and the internal thickness (pore depth) is 50 μm. The microfluidic chip includes 377 circular mono-sized grains with 800 μm of diameter and the size of pore throat between each two grains is 140 μm (Figure 4.1a). Figure 4.1a and 1b present the configuration of the microfluidic chip set-up. The microfluidic chip with injection and extraction ports is fixed in a steel holder and placed vertically. A reactive solution was prepared based on *Nemati & Voordouw*'s experimental work (2003), which contained 12g (~0.2 M) urea ($CO(NH_2)_2$, U5378, Sigma-Aldrich), 30g (~0.2 M) calcium chloride dihydrate ($CaCl_2 \cdot 2H_2O$, C3881, Sigma-Aldrich), and 0.1g (~0.01 w%) urease powder (extracted from jack beans, Type III, 26100U/g, U1500, Sigma-Aldrich) per liter. The concentrations of both urea and calcium chloride were at a 1:1 molar ratio. Unlike *Nemati & Voordouw*'s recipe, the solution did not include milk powder. The prepared solution was injected from the bottom inlet.

The injection-reaction process was repeated 10 times. After each injection, both inlet and outlet ports were closed to prevent evaporation and fluid flow. The solution was left to react for 48 hours. Time lapse digital imaging was performed every 10 minutes using a digital camera (D5200, Nikon) equipped with a 60mm micro lens (AF-S Micro NIKKOR 60mm f/2.8G ED, Nikon) was used to capture the nucleation and growth of precipitated calcite within the pores of microfluidic chip. After each injection-reaction cycle, the retained solution in the microfluidic chip was rinsed with de-ionized (DI) water, before

injecting a next cycle. For all cycles, the volume of the injected solution was kept constant at about 4.05μL, which was similar to the initial pore volume of the micromodel.

An image processing algorithm was developed using MATLAB to automatically detect and extract the precipitated calcium carbonate crystals from the original images and monitor the precipitation process within the microfluidic chip over time. Raw images of microchip experiment were converted to digital RGB matrixes. Different phases existing in the microfluidic chip including circular grains, precipitated calcium carbonate minerals, some trapped gas bubbles and pore space were detected by applying different intensity thresholds for each phase. The proposed algorithm minimizes the risk of subjective bias or missing information by manual detection, maximizing the accuracy of the detection process and significantly reducing the image analysis time. Figure 4.1c shows the raw image of the entire microfluidic chip at the end of the 4th treatment cycle. Figure 4.1d highlights a cropped area of Figure 4.1c including the circular grains and precipitated minerals. Figure 4.1e shows the final processed image by the automated image processing algorithm including all the detected circular grains (presented in green color), precipitated minerals (presented in red color), and pore space (presented in white color). With image processing it was assumed that the precipitated calcium carbonate crystals form cylinders, which fill up the entire height of the pore space. The image processing is limited by the resolution of the images. Based on the image resolution of about 6.5μm per pixel and considering that crystals comprised of less than 2 by 2 pixels were regarded as noise, crystals with an equivalent diameter lower than 15μm could not be detected and were ignored. More details about the image processing algorithms are described by *Kim et al.* [under review].

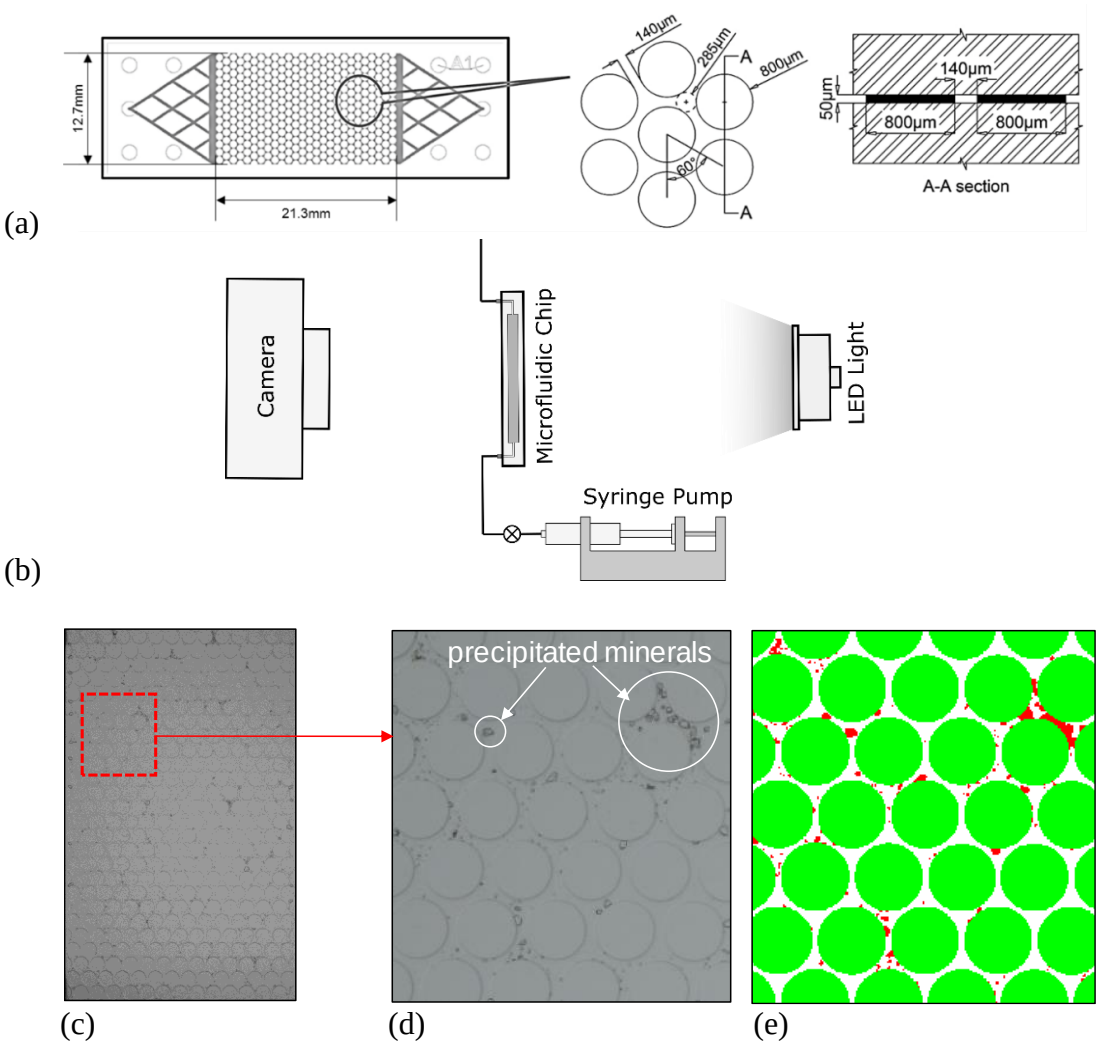


**Figure 4.1.** (a) Microfluidic chip geometry (*Mahabadi et al.*, 2016; *Zheng et al.*, 2017), b) the configuration of microfluidic chip experimental setup, (b) Raw image of the entire microfluidic chip after the 3rd cycle of treatment, (c) Zoom-in area of the precipitated pore space, (d) Processed image of the zoom-in area that detects circular grains and biomineral particles

## 4.3 CFD MODEL AND SIMULATION

### 4.3.1 Model Development

The processed binary images of the cemented microfluidic chip were used as the input geometry to develop a CFD model using the finite element software package

COMSOL Multiphysics (version 5.0). Figure 4.2 demonstrates the preparation process of the geometry development from the images of the cemented microfluidic chip. In order to prepare a compatible format of geometry for COMSOL, the processed binary images were converted to ".dxf" format (vector image format). Due to the vectorization, the ".dxf" format included several undesirable objects, which needed to be trimmed prior to the geometry development. The trimming of unwanted objects was achieved using the "PLD" command in AUTOCAD, with which the vertices and segments were removed. The trimmed vectorized format including both channels and particles was then exported to COMSOL and subtracted from the entire rectangular domain of the microfluidic chip. The difference of microchip domain and vectorized domain provides only the flow channels, which can then be employed as the geometry for the CFD simulations. The mesh elements were generated within the model using the automatic physics-controlled meshing setup. However, highly precipitated cases (higher precipitation cycles) contain thousands of (small) calcite particles in which manual mesh size refinements needed to be considered. Particularly, when the formation of crystals created extremely sharp corners, further modification schemes needed to be examined for the mesh generation of the domain. The number of mesh elements to be compiled increased with the increased number of treatment cycles, due to the complex geometry caused by the formation of biominerals. The number of elements allocated for the non-treated pore space was 21,871, while the cycle 10th of treatment required 1,836,494 elements. Table 4.1 presents the general information about the geometry in different treatment cycles.

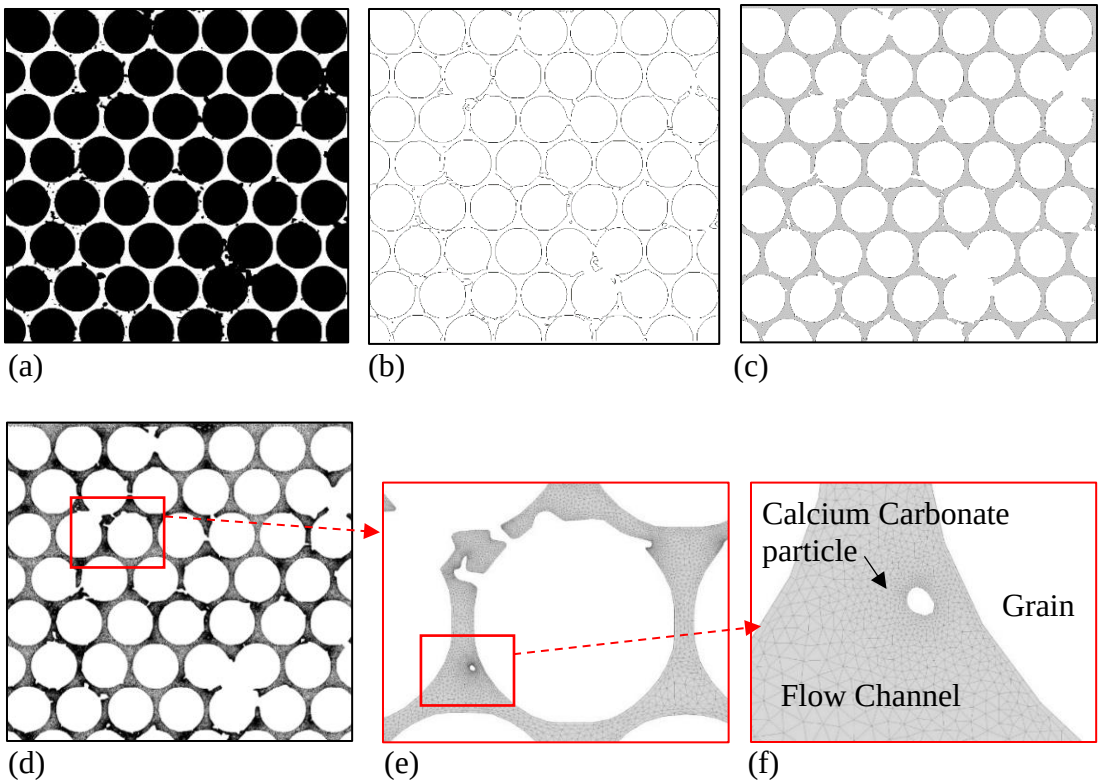


**Figure 4.2.** Development of the geometry of finite element model: (a) Binary image from the experiment, (b) Vectorized binary image, (c) Extraction of flow channels, (d-f) Meshed numerical model

**Table 4.1.** Information of microfluidic chip pore space model before treatment and after 3rd, 6th and 10th cycle of treatment

| | Non-treated | Cycle 3rd | Cycle 6th | Cycle 10th |
|---|---|---|---|---|
| Precipitation content (%)** | 0 | 2.64 | 5.89 | 8.67 |
| Total porosity | 0.3 | 0.29 | 0.28 | 0.27 |
| Mobile porosity | 0.3 | 0.26 | 0.22 | 0.16 |
| Normalized permeability* | 1 | 0.58 | 0.38 | 0.20 |
| Tortuosity | 2.25 | 3.15 | 4.51 | 5.97 |
| Total simulation time (min) | 0.92 | 29.3 | 63.3 | 117.5 |
| Number of elements | 21,871 | 529,835 | 1,161,013 | 1,836,494 |

* Normalized permeability (relative permeability) is the permeability relative to the maximum permeability occurred in the non-treated case.
* Precipitation content (%) is defined as the total volume of biominerals proportional to the initial total volume of pores.

### 4.3.2 Flow and Transport Simulation

Once the geometry was defined and the mesh was generated, two simulation steps and the required boundary conditions were assigned to the model:

*Stationary flow field simulation*: It was assumed that the flow field follows Stokes' flow (creeping flow) in which the fluid is incompressible and the internal term of stokes flow is negligible. The governing equation for the stationary flow field simulation is as follow:

$$\mu\nabla^2 u - \nabla p + f = 0 \tag{3}$$

where $u$ is the velocity of the fluid, $\nabla p$ is the gradient of the pressure, $\mu$ is the dynamic viscosity of the fluid, and $f$ is the applied body force which is assumed to be 0 in this study. A constant velocity of *1 mm/s* was defined at the inlet boundary located at the bottom of the microfluidic chip; a constant pressure (atmospheric pressure) was specified at the outlet located at the top of the microfluidic chip. The result of the stationary flow simulation was then used as the initial conditions for the next simulation step, the time dependent mass transport.

*Time dependent solute mass transport*: a constant concentration was imposed at the inlet boundary; zero concentration gradient was specified at the outlet. The total time of 20 seconds and time-intervals of 0.1 sec were selected for the time-dependent simulation of substrate transport. The governing equation for the simulation of the time dependent transport of species is as follows:

$$\nabla.(-D\nabla c) + u.\nabla c = 0 \tag{4}$$

where $\nabla.(-D\nabla c)$ describes diffusive flux, $D$ is the diffusion coefficient, $c$ is the concentration of the substrate, and $u.\nabla c$ describes the convective flux.

Numerical simulations were performed for four different precipitation levels: non-treated, cycle-3, cycle-6 and cycle-10. All the input parameters including the concentration and diffusivity of substrate were maintained constant for all the treatment cycles, while the geometry of the flow channels as the results of different levels of precipitation was the only difference. Table 1 shows general information regarding the pore space geometry achieved in this study.

## 4.4 RESULTS AND DISCUSSION

### 4.4.1 Flow Field, Total Porosity and Mobile Porosity

The precipitation of calcium carbonate minerals during each cycle, in which a reactive solution is injected into the microfluidic chip, fills up part of the pores, which reduces the total pore volume. Local pore-clogging by single crystal or agglomeration of multiple crystals creates isolated pore clusters inaccessible to the fluid flow. The mobile pore volume (or effective pore volume), which is defined as the portion of pore space that contributes to the fluid flow, reduces faster than the actual pore volume as a result of local-pore clogging. The reduction in mobile pore volume affects the flow field and the transportation of solutes, and consequently results in an irregular distribution of minerals, which eventually reforms the hydrodynamics of the porous media even further. In a few cases, the hydrodynamic forces were large enough to break the weak bonding between the crystals and grains and reopen blocked pore throats. Figure 4.3 shows a selected zone in the microfluidic chip for cycle-3 and cycle-6 which illustrates the evolution of pore structure and flow fields as a result of the nucleation and growth of calcium carbonate crystals within the pore space.

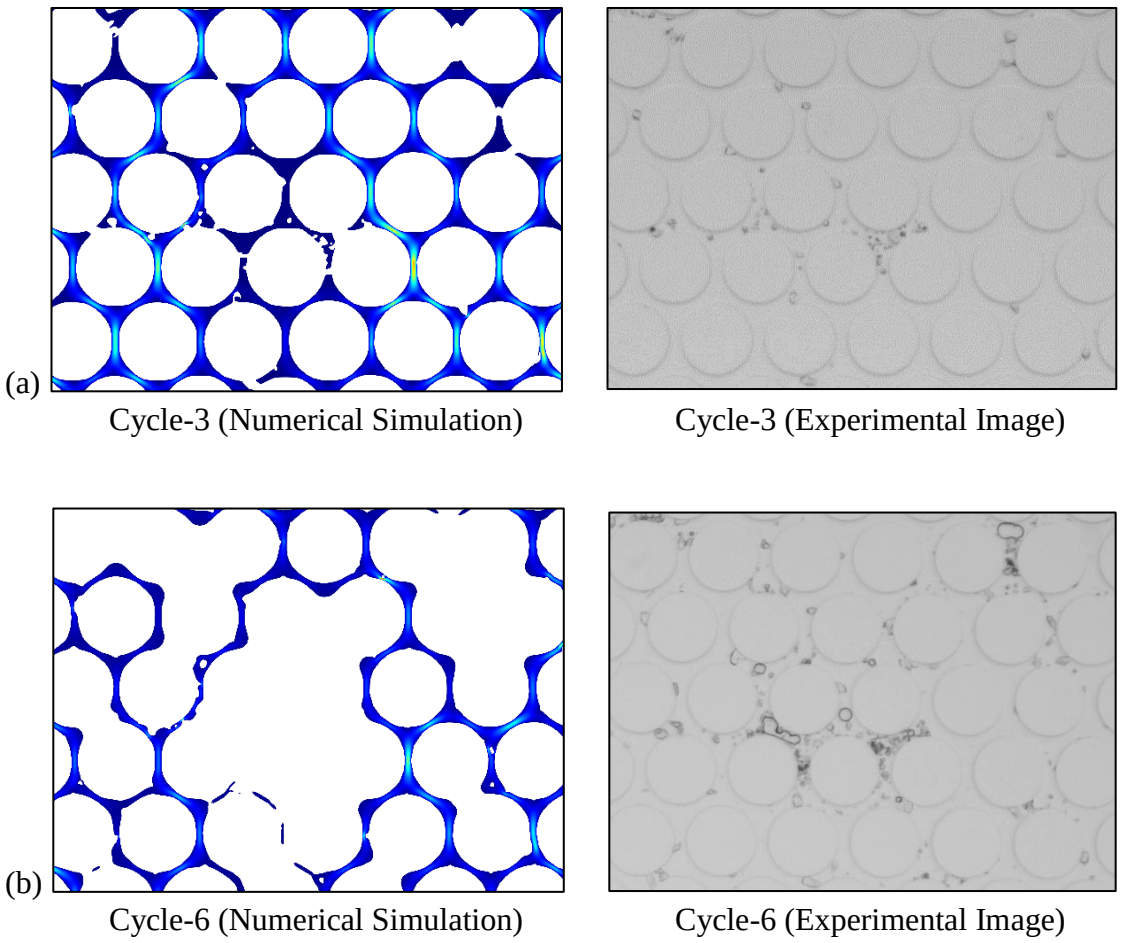


**Figure 4.3.** Flow fields from the numerical simulation results and raw images of the calcium carbonate precipitated microfluidic chip: a) Cycle-3, b) Cycle-6.

The mobile porosity within the microfluidic chip was calculated from the resulting velocities of the stationary flow field simulations, in which the velocity of 0.001 mm/s (0.1 % of the inlet velocity) was selected as a threshold to distinguish immobile zones. The areas with flow velocities below the threshold were subtracted from and divided by the initial total pore volume of the microfluidic chip to obtain the mobile porosity, that contributes to the flow and convective transport. Figure 4.4a shows the total pore space, which includes all flow velocities, while Figure 4.4b presents the mobile pore volume, which only shows the pores with a velocity range of $0.001v_{max} < v < v_{max}$. The results

clearly show that the divergence between total porosity and mobile porosity builds up as the degree of biomineralization increases.

The relation between the amount of precipitation and the evolution of porosity can be found by comparison between the results of different biomineralization cycles. The total and mobile porosity of the microfluidic chip for different treatment cycles is presented in Figure 4.5a. The single-colored fluid flow fields presented in Figure 4.4 were used to quantify the porosity of the microfluidic chip. The total and mobile porosity of the microfluidic chip were calculated for different precipitation levels by dividing the surface area of the flow channels (row-a in Figure 4.4 for total porosity, and row-b for mobile porosity) by the surface area of the entire domain (total volume) of the non-treated microfluidic chip. The total porosity linearly decreases with the increase in the number of treatment cycles while the mobile porosity reduces following a parabolic function. The best-fit equations determining the change of total and mobile porosity with the cycles of treatment were calculated as follows:

$$\emptyset_t = \emptyset_{to} - 0.0028N \tag{5}$$

$$\emptyset_{mobile} = \emptyset_{to} - 0.0108N - 0.0003N^2 \tag{6}$$

where $\emptyset_t$ is the total porosity, $\emptyset_{to}$ is the initial total porosity (non-treated sample), $\emptyset_{mobile}$ is the mobile porosity, and $N$ is the number of treatment cycles. Based on the best fit equations, the total porosity has a linear relationship with the cycles of injections while the mobile porosity follows a parabolic equation. After 10 cycles of treatment the total porosity is reduced by 9 % from 0.3 to 0.273, while the mobile porosity decreased significantly by 47 % from 0.3 to 0.159. In other words, although 91 % of the pore space

is still unoccupied by the biomineral crystals, only 53 % of the pore space is accessible to the fluid flow.

Figure 4.5b shows the total and mobile porosity in terms of precipitation contents. Here, the precipitation content (%) is defined as the total volume of biominerals proportional to the initial total volume of pores. Since, the precipitation content increases by approximately 1 % after each treatment cycle, the total and mobile porosity can be estimated by substituting number of cycles, *N*, with the precipitation content (%) in the equations 5 and 6.

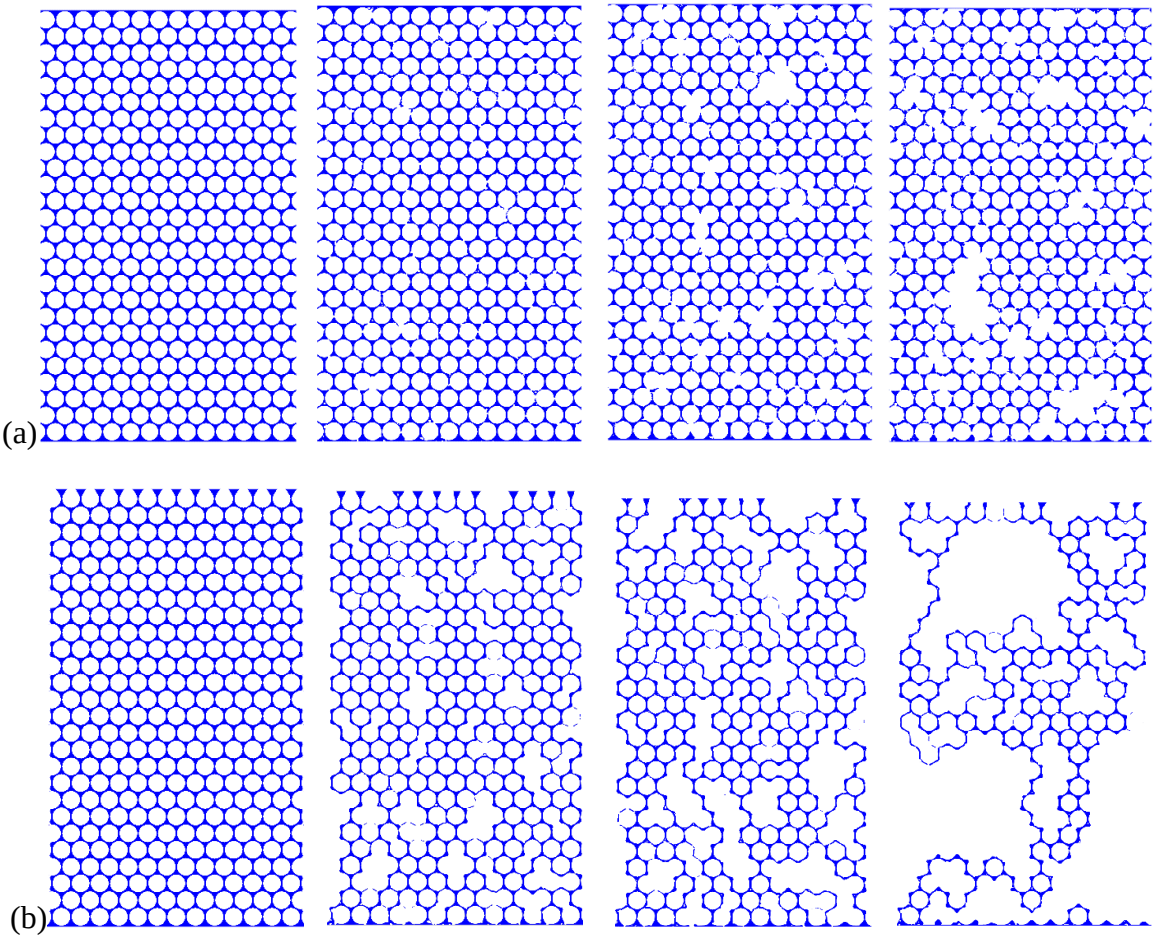


**Figure 4.4.** Pore space shown with blue color for different cementation levels: (a) Total pore space, (b) Mobile pore space (effective pore space that contributes to the fluid flow)

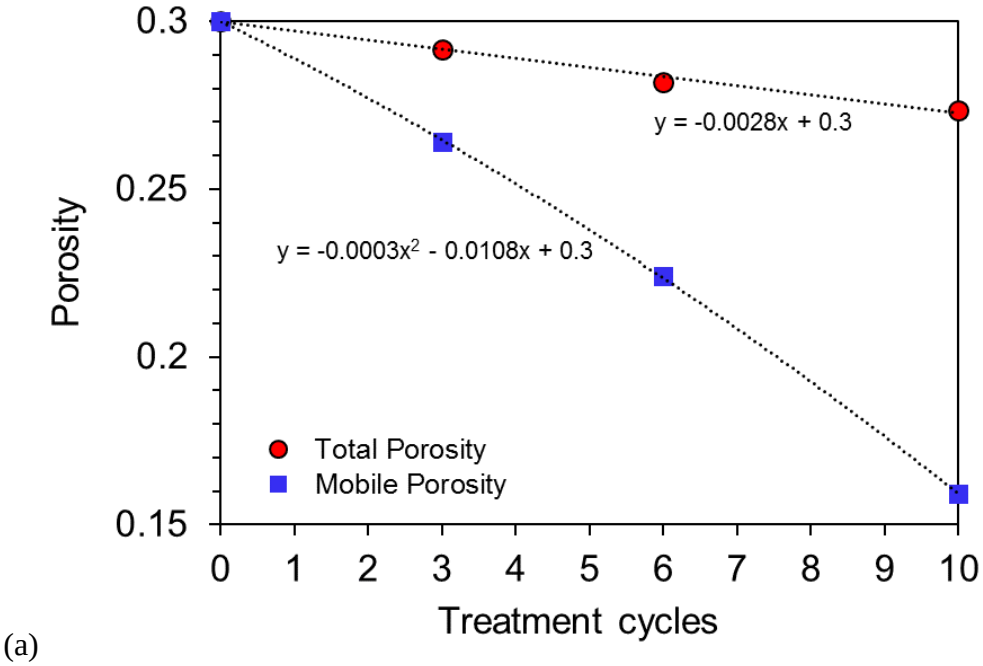


(a)

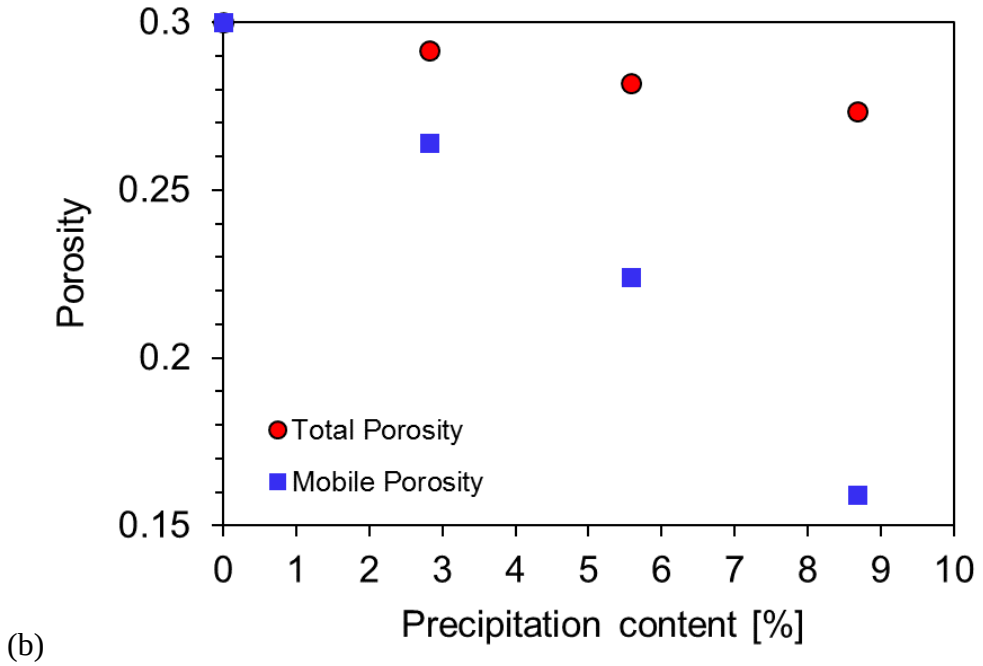


(b)

**Figure 4.5.** Numerical simulation results: (a) Total and mobile porosity for different treatment cycles, (b) Total and mobile porosity for different precipitation content (%)

### 4.4.2 Mass Transport and Residence Time

The reduction in mobile porosity due to calcium carbonate precipitation, and the resulting changes in the hydraulic flow field significantly affect the transport and distribution of solute substrates during subsequent injections. Figure 4.6 shows the spatial concentration profile after 1, 2 and 3 seconds of injection for the non-treated microfluidic chip, and for the $3^{rd}$, $6^{th}$ and $10^{th}$ treatment cycle. The results show that the concentration profile forms a completely uniform front displacing the water out of the crystal-free porous media in the non-treated case, while as the level of mineral precipitation increases, the heterogeneity of the transport patterns increases. The simulation results demonstrate that higher degree of calcite precipitation results in development of fringe patterns and faster transport of substrate through the porous media. For example, after 1 second of injection the substrate in the non-treated case is distributed only within the first quarter of the pore space, while at the same time in the $10^{th}$ cycle some part of substrate has already reached to the outlet boundary.

Figure 4.7 presents the breakthrough curves of the normalized average concentration along the outlet boundary of the microfluidic chip, which are an indicator of the substrate residence time. As the biomineral content increases, the residence time of the substrate decreases. The normalized average concentration after 3 seconds of injection is 0 for the non-treated pore space, 0.18 for the cycle, 0.34 for the $6^{th}$ cycle and 0.83 for $10^{th}$ cycle.

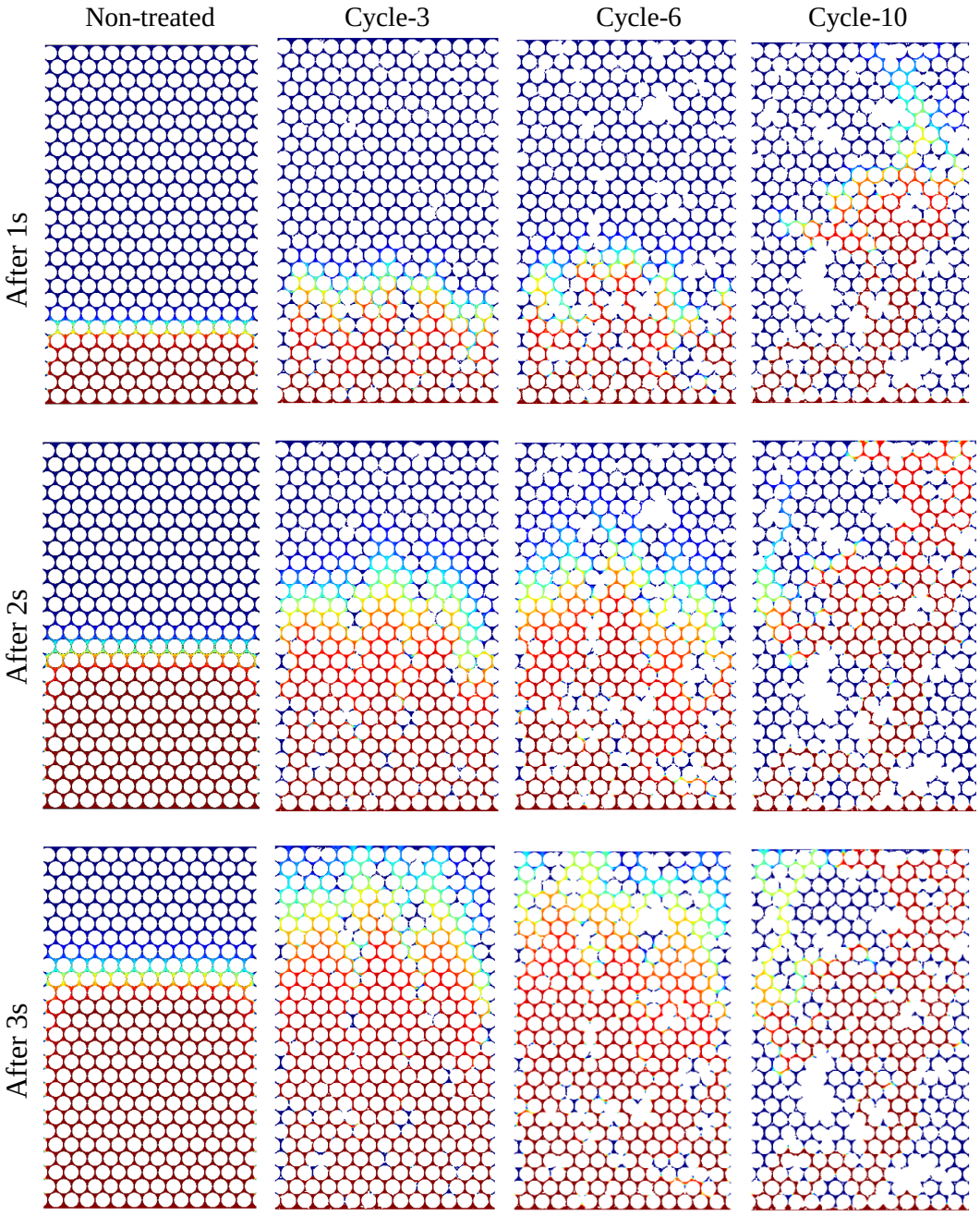


**Figure 4.6.** Numerical simulation results: the concentration of the substrate after 1, 2 and 3 seconds of injection into the microfluidic chip for non-treated, cycle-3, cycle-6, and cycle-10 of treatment

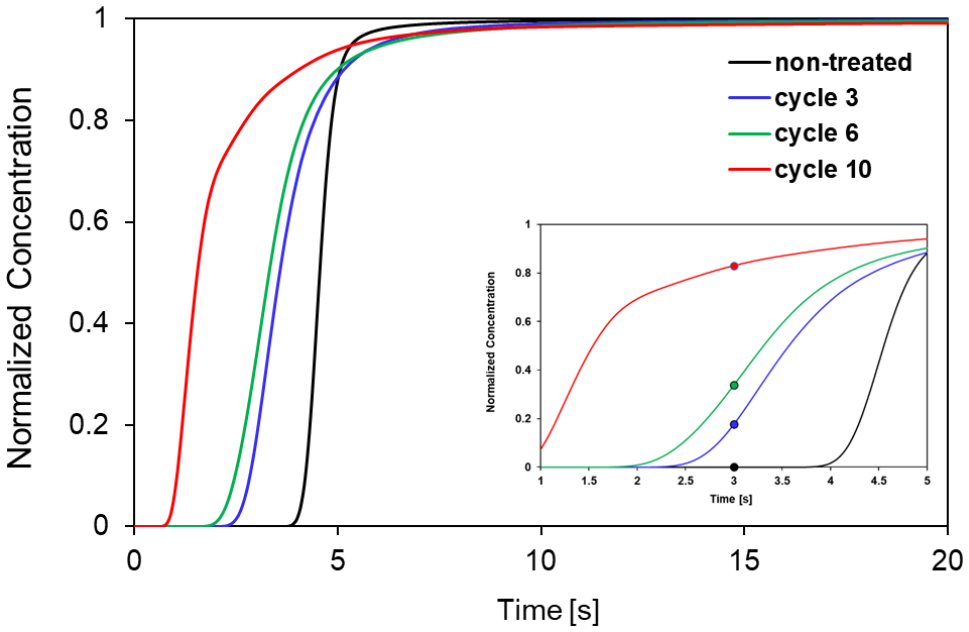


**Figure 4.7.** Normalized average concentration along the outlet boundary of the microfluidic chip over time for different cycles of treatment

### 4.4.3 Porosity-Permeability Relationship

In this study we aim to explore the validity of Kozeny-Carman and Power-Law equations, and their associated parameters in prediction of the porosity-permeability relationships in porous media affected by biomineralization process.

Three different approaches are considered to calculate the precipitation induced permeability reduction relationships:

1) *Numerical simulation:* The permeability of the microfluidic chip is calculated for different cycles of treatment directly using the CFD simulations and normalized by the maximum permeability simulated in the case of unaltered porous media (mineral free microfluidic chip). The CFD numerical results were considered as the baseline for comparison.

2) *KC equation:* Using the Kozeny-Carman equation, three different paths were used to calculate the change in permeability; a) KC-General: where only changes in total porosity was considered to calculate the permeability change (the tortuosity remained unchanged); b) KC-Effective Porosity: where the changes in effective porosity were used to calculate the permeability change while the tortuosity remained unchanged; c) KC-Tortuosity: where both the changes in total porosity and tortuosity were considered for permeability change calculations. The tortuosity of the non-cemented and cemented microfluidic chip were calculated using the results of the CFD simulations. To do this, the length of flow paths were calculated and divided by the straight length of the domain connecting the inlet to the outlet boundary.

3) *Power-law equation:* The power-law equation was fitted to the numerical simulation and KC equation results to achieve the best fitting parameter, $\eta$, with the minimum RMSE.

Figure 4.8a presents the normalized permeability values calculated based on the mentioned methods for the non-treated, cycle-3, cycle-6 and cycle-10 treatment cycles. The result presents that using only the total porosity in Kozeny-Carman equation (KC-General: solid blue line in Figure 4.8) leads to a significant overestimation of permeability. The estimated reduction in permeability by KC-General model is only 25 % after 10 cycles of treatment while the numerical results shows up to 80 % permeability reduction. Although adding the tortuosity change to the Kozeny-Carman equation (KC-Tortuosity: yellow triangles in Figure 4.8) improves the accuracy of the results, still there is a meaningful discrepancy between the permeability values. Particularly, as the level of precipitation increases, the difference between the direct calculation of permeability (CFD numerical results) and the predicted permeability by KC-Tortuosity escalates.

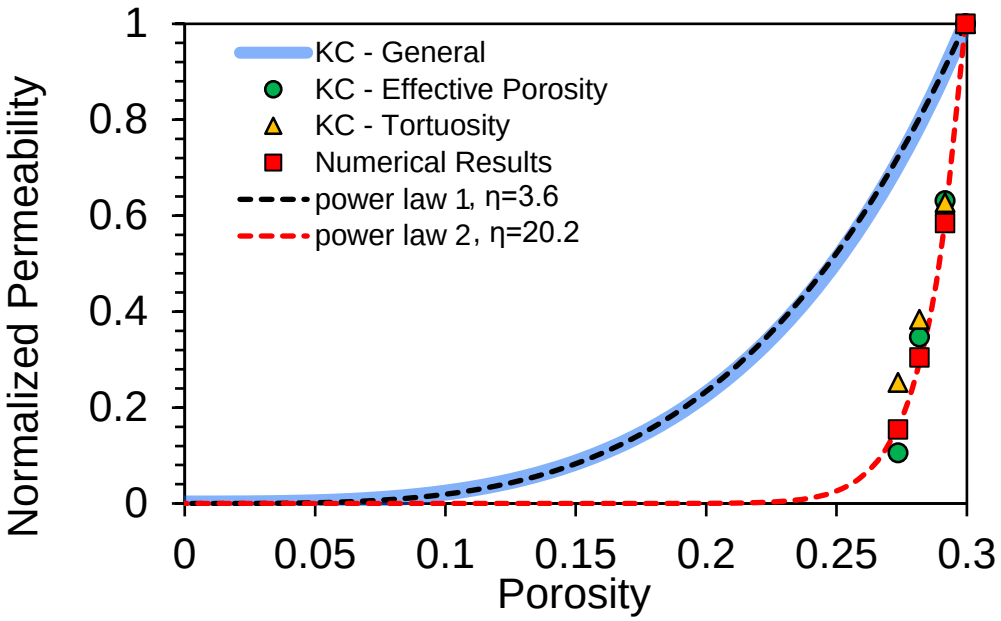


(a)

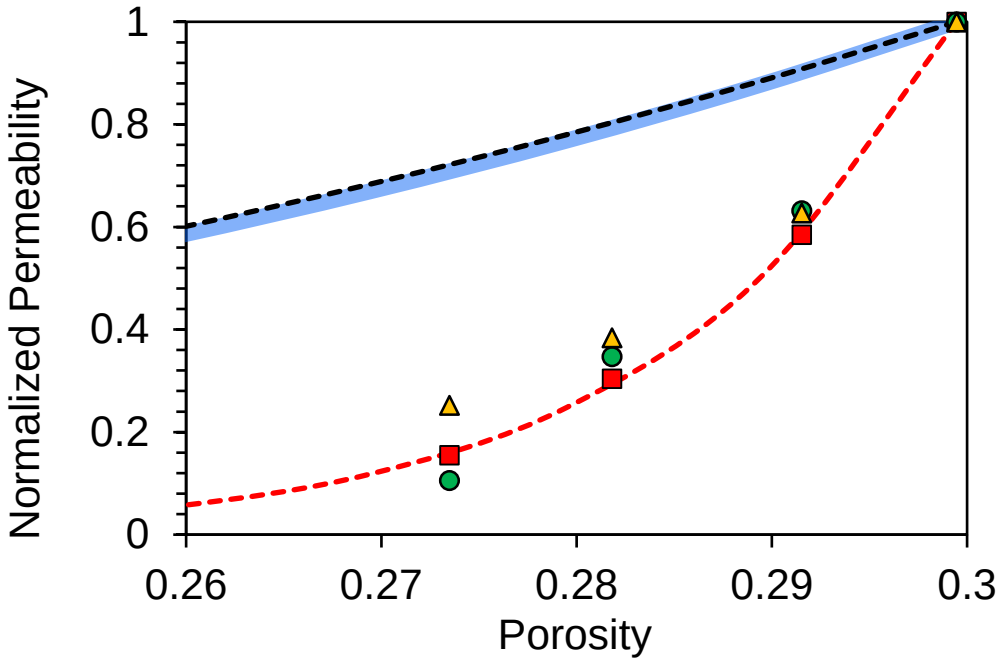


(b)

**Fig 4.8.** Numerical results compared to the different forms of Kozeny-Carman (KC-General, KC-Effective Porosity and KC-Tortuosity) and power law equations ($\eta$=3.6 and $\eta$=20.2).

This is in agreements with the agreements with the results of *Mostaghmi et al.* (2013) who showed that the Kozeny-Carman equation may significantly overestimate the permeability, particularly in complex, heterogeneous, and poorly connected porous media. However, the results reveal that by inserting the mobile porosity into the Kozeny-Carman equation, even by ignoring the tortuosity changes, the permeability can be estimated accurately. In the field scale, the mobile porosity can be measured relatively easy by injecting a trace fluid and recording the residence time of the effluent. The fitting parameters of the power-law equation were calculated to be $\eta$=3.6 for the KC-General while the realistic fitting parameter is considerably higher ($\eta$=20.2).

## 4.5 CONCLUSIONS

A hybrid experimental-numerical approach is used in this study to get insight about micro-scale processes of biomineralization and its associated impacts on the behavior of porous media such as the evolution of pore structure and development of immobile pore zones.

The total porosity linearly decreases with the increase in the number of treatment cycles while the mobile porosity significantly reduces following a parabolic function. The reduction in mobile porosity due to calcium carbonate precipitation, and the resulting changes in the hydraulic flow field significantly affect the transport and distribution of solute substrates during subsequent injections. The concentration profile forms a completely uniform front displacing the water out of the crystal-free porous media in the non-treated case; while as the level of mineral precipitation increases, the heterogeneity of the transport patterns increases. The simulation results demonstrate that higher degree of

calcite precipitation results in development of fringe patterns and faster transport of substrate through the porous media.

Using only the total porosity in Kozeny-Carman equation leads to a significant overestimation of permeability. The estimated permeability by KC-General model is reduced by only 25 % after 10 cycles of treatment while the numerical results shows up to 80 % permeability reduction. Although adding the tortuosity change to the Kozeny-Carman equation (KC-Tortuosity) improves the accuracy of the results, still there is a meaningful discrepancy between the permeability values. Particularly, as the level of precipitation rises, the difference between the direct calculation of permeability (CFD numerical results) and the predicted permeability by KC-Tortuosity escalates. This is in agreements with that the Kozeny-Carman equation may significantly overestimate the permeability, particularly in complex, heterogeneous, and poorly connected porous media. By inserting the mobile porosity into the Kozeny-Carman equation, even by ignoring the tortuosity changes, the permeability can be estimated accurately. In the field scale, the mobile porosity can be measured relatively easy by injecting a trace fluid and recording the residence time of the effluent. The fitting parameter of power-law equation were calculated $\eta$=3.6 for the KC-General while the realistic fitting parameter is considerably higher, $\eta$=20.2.

**Acknowledgments**

Work described herein was supported in part by the National Science Foundation (NSF) Engineering Research Center program under the grant numbered ERC-1449501. Any opinions, findings and conclusions or recommendations expressed in this material are those of the authors and do not necessarily reflect those of the NSF.

# CHAPTER 5

# BIOGENIC GAS FORMATION IN POROUS MEDIA: A COMPARATIVE STUDY WITH $CO_2$ GAS FORMATION VIA DEPRESSURIZATION

This chapter will be submitted to *'Environmental Science & Technology Journal'* or '*Lab on a Chip'* as Kim, D., Mahabadi, N., Wang, L., Jang, J., & van Paassen, LA. (2019). "Visualization Biogenic $N_2$ Gas Formation in Synthetic Porous Media: A Comparative Study with $CO_2$ Gas Formation via Depressurization."

## ABSTRACT

In this study experiments were performed using a glass microfluidic chip, in order to investigate the effect of gas formation rate on the gas formation mechanism and residual gas distribution and saturation in porous media. Biogenic gas formation via microbial denitrification was stimulated inside the microfluidic chip and compared with abiotic depressurization of a supersaturated $CO_2$ solution at two different depressurization rates. Time lapse imaging, and image analysis were used to observe and quantitatively characterize the gas phase. Visual observations indicated that the biogenic $N_2$ gas did not homogeneously desaturate the microfluidic chip, but started from a single nucleation point, which expanded to form a big gas pocket, gradually migrating upward or through channels mainly along the edges of porous domain. The two experimental cases of $CO_2$ gas formation showed completely different patterns, affected by the depressurization rate and initial pressure. The equilibrated degree of saturation levels of two $CO_2$ cases were comparable (~40 %) but much lower than that of biogenic $N_2$ gas case (~80 %).

## 5.1 INTRODUCTION

Stimulating indigenous micro-organisms or augmenting soil with exogenous micro-organisms, biochemical conversion in the subsurface can be catalyzed, which lead to formation of biomass, biominerals or biogas. These processes can significantly alter hydro-mechanical behavior of soil, and have been investigated as new technologies for soil improvement or modification. In particular, desaturation of soils through biogas formation during denitrification has been suggested as an application to mitigate earthquake-induced liquefaction (*He,* 2013; *Kavazanjian et al.,* 2015; *Rebata-Landa & Santamarina,* 2012; *van Paassen et al.,* 2010). Denitrifying bacteria are being considered, which reduce nitrate to nitrogen gas, while oxidizing an organic carbon source to form dissolved inorganic carbon, which may partly transfer to carbon dioxide gas. Trapped bubbles of nitrogen and carbon dioxide gas desaturate the soil and may dampen pore pressure build up during earthquake events.

A small reduction of soil water saturation (less than 10 %) is sufficient to significantly increase the cyclic resistance of soils (*Arab et al.,* 2011; *Tsukamoto et al.,* 2002; *Yang et al.,* 2004; *Yegian et al.,* 2007; *O'Donnell,* 2016). Recent studies have shown that the saturation level could be reduced to 80~95 % via microbial denitrification due to the nitrogen gas formation within several days (*Nakano,* 2018; *O'Donnell et al.,* 2017; *Pham et al.,* 2016). The degree of saturation has been determined experimentally by monitoring depletion of substrate concentrations or measuring the volume changes of the soil and expelled water as a result of gas production at soil column scale. There also have been efforts to develop numerical models to predict the desaturation of soils via microbially induced denitrification, which theoretically estimate the amount of nitrogen gas formation

at different depth or pressure levels using the Henry's law and ideal gas law (*Hall et al.*, 2018, *van Paassen et al.,* 2018). However, these models and experiments assume homogeneous gas distribution throughout the soil. Information about the spatial distribution and persistence of the biogenically formed gas is limited and requires further studies.

In studies on biogenic or abiotic gas formation or exsolution, three mechanisms are distinguished: bubble nucleation, bubble growth and migration or invasion. These mechanisms depend on the gas and liquid properties, energy potential for phase change, gas solubility, and heterogeneity of the porous system. Nucleation of new gas bubbles occurs when the concentration of dissolved gas exceeds a threshold, in order to allow a bubble to form and continue to grow. This threshold concentration is often significantly larger than the equilibrium concentration, which is defined by Henry's law.

$$C^* = \frac{P}{K_H} \tag{1}$$

In which $C^*$ is the equilibrium concentration of the gas in the solute phase, P is the partial pressure of the gas in the gas phase and $K_H$ is Henry's constant, which varies for different types of gas and temperature. The nucleation threshold in a homogeneous solution is higher than in presence of rough surfaces, as these surfaces may act as a nucleation site. A nucleating bubble has to reach a critical size in order to remain stable, as the partial pressure of the gas depends on the bubble radius, following the Young-Laplace equation:

$$\Delta P = P_g - P_w = \frac{2\gamma}{R} \tag{2}$$

In which $P_g$ and $P_w$ are the gas and water pressure, $\gamma$ is the surface tension at the liquid gas interface and $R$ is the radius of the bubble.

Once a stable bubble is formed it may grow, either due to changes in pressure or through gas transfer. A drop in pressure (both water and gas pressure) would cause an existing bubble to increase in volume following Boyle's law, which postulates that volume, *V*, is inversely proportional to pressure:

$$V \propto \frac{1}{P} \tag{3}$$

However, a drop in pressure also reduces the gas solubility, following Henry's law. This could stimulate gas transfer from the solute to the gas phase, as gas transfer is driven by a concentration gradient over the gas-liquid interface

$$J = k_L A(C_L - C^*) \tag{4}$$

In which $J$ is rate of gas transfer from the liquid to the gas phase, $k_L$ is the gas transfer coefficient, $A$ is the gas-liquid interfacial area and $C_L$ is the concentration of the gas in the liquid. In non-mixed systems the gas transfer rate may be limited by diffusion.

Different approaches have been used to study or simulate formation and migration of gas in porous media. For example, *Mahabadi et al.* (2016) simulated gas formation in porous media using a pore network model, assuming that gas bubbles would start as randomly distributed micro-sized bubbles, which migrated upward through the pore space due to buoyancy and which grow through diffusion and gas transfer from the solute to the gas state or while they move upward due to a decrease in hydraulic pressure or by coalescing with other. When bubbles are still smaller than the pore throat size they can freely migrate upwards, but once the bubbles get bigger than the pore throats, the mobility of gas bubbles is restricted and gas bubbles may get trapped (*Zuo et al.*, 2013).

Further increase in gas volume would force cause the gas bubbles to get trapped in the pore space. Still the trapped gas bubbles can migrate and displace the water phase.

Displacement of a liquid phase by a gas phase in porous media (or displacement of two immiscible fluids such as oil and water) has been extensively studied in relation to various engineering applications such as enhanced oil and gas production, $CO_2$ sequestration or soil remediation (*Mahabadi et al.*, 2019). Three different displacement patterns are distinguished: stable displacement, viscous fingering and capillary fingering. The displacement patterns are affected by the viscosity ratio of the two fluids, interfacial tension, the displacement velocity, the wettability of the solid phase and the characteristics and geometry of the porous medium (*Lenormand et al.*, 1988; *Zhang et al.*, 2011). To describe migration of gas bubbles or distinguish different displacement mechanisms in multiphase flow systems various dimensionless numbers are used, including Capillary number (Ca), viscosity ratio (M) and Bond number (Bo). The Capillary number relates the viscous forces to the surface tension:

$$Ca = \frac{v\mu_{inv}}{\gamma} \tag{5}$$

In which $v$ is the flow velocity in [$m^3$/s] and $\mu_{inv}$ is the viscosity of the invading fluid. High capillary numbers would favor stable displacement resulting efficient displacement, whereas low capillary numbers would result in capillary fingering. The viscosity ratio relates the viscosity of the invading fluid with the viscosity of the defending fluid:

$$M = \frac{\mu_{inv}}{\mu_{def}} \tag{6}$$

A high viscosity ratio would result in stable displacement, whereas a low viscosity ratio would result in viscous fingering. Both viscous fingering and capillary fingering would result in a less efficient displacement of the defending fluid by the invading fluid

than stable displacement. In the case that gas is displacing water, the viscosity ratio is lower than 1, since the viscosity of gas is significantly lower than the viscosity of water. Hence, viscous fingering can be expected. The Bond or Eötvös number relates gravitational or buoyant forces with capillary forces:

$$Bo = \frac{\Delta\rho g L^2}{\gamma} \tag{7}$$

In which $\Delta\rho$ is the difference in density, $g$ is the gravity acceleration, $L$ is the characteristic length, i.e. the radius of curvature of the gas-water interface. A low value for the Bond number (typically less than one) indicates that surface tension dominates, e.g. that bubbles remain spherical, whereas a large value for the Bond number indicates that the system is relatively unaffected by surface tension, and bubbles may easily deform or break up into smaller bubbles. The Bond number also affects the movement of trapped gas bubbles. In case a bubble entirely fills a pore, it shows 'slug' movement as it squeezes through the pore throats. Experimental results described in literature showed that a slug does not move in water-filled capillary tubes for Bond numbers smaller than 3.37 (*Bretherton,* 1961; *White & Beardmore,* 1962).

Some researchers have looked at the distribution patterns in biogenic gas formation through denitrification. *He* (2013) observed that large gas pockets were produced during microbial denitrification and non-uniformly distributed using X-ray CT cross section images. *Pham et al.* (2016) visualized produced biogenic gas within PVC sand column using 3D X-ray CT tomography. Most of the gas appeared to be present in coarser grained sand at the top and bottom of the column, while in a finer grained sand the produced gas created cracks mostly in the upper half of the sand column. Although it has been found that a small fraction of gas in the pores can significantly affect the mechanical

behavior of soils, it is unclear how the mechanism of biogenic gas formation within a soil system will affect the spatial distribution, and how the equilibrated degree of saturation after treatment affects the mechanical response and persistence of the gas phase.

We hypothesize that the mechanisms of biogenic gas formation i.e. nucleation, growth, migration and displacement mechanisms, and resulting distribution and saturation of the soils, are affected by the rate of gas formation. In this study gas formation experiments were performed using microfluidic chip, in which the rate of gas formation and pressure conditions were varied, in order to test this hypothesis and improve understanding about these mechanisms.

## 5.2 EXPERIMENTAL STUDY

### 5.2.1 Microfluidic Chip

A two-dimensional transparent microfluidic chip (Micronit Microfluidics BV, Netherlands) was designed and fabricated to resemble a homogenized circular particle packing. The dimensions of the microfluidic chip are 21.3 mm×12.7 mm, and the internal thickness (pore depth) is 50 μm. The microfluidic chip includes 377 circular mono-sized grains with 800 μm of diameter and the size of pore throat between two grains is 140 μm (Figure 1a).

### 5.2.2 Biogenic $N_2$ Gas Formation in the Microfluidic Chip

The reactive solution for biogenic gas formation was prepared and consisted of a mixed bacterial culture and a growth medium containing 12 mM of calcium acetate ($Ca(C_2H_3O_2)_2$), 10 mM of calcium nitrate ($Ca(NO_3)_2$), and 0.5 mL/L of trace mineral

solution Figure 1b shows the configuration of the microfluidic chip experiment. The microfluidic chip was fixed in a steel holder and placed vertically. The prepared solution was injected into the microfluidic chip from the bottom inlet. The volume of the injected solution was about 5 mL, which was sufficient to flush the pore volume of the microfluidic chip. After injection of solution, both inlet and outlet ports were closed to prevent evaporation and fluid flow. The solution was left to react for a month.

### 5.2.3 $CO_2$ Gas Formation via Depressurization in the Microfluidic Chip

A high-pressure resistant system was designed and built for $CO_2$ gas formation in a microfluidic chip (Figure 1b). The system consisted of a $CO_2$ gas tank, a high pressure chamber for dissolving $CO_2$ gas into water, a syringe pump for taking water with dissolved $CO_2$ from the high pressure chamber and injecting it into the microfluidic chip, the microfluidic chip, and a second high pressure chamber for collecting remainder liquid and gas from the microfluidic chip outlet. The entire system was closed from the atmosphere and valves were used to open and close different compartments. $CO_2$ gas was dissolved in de-ionized (DI) water and stored in the high pressure chamber #1. By opening all valves, the entire system is connected. $CO_2$ gas from the tank was released to the system at a pressure of 1 MPa. The system was left at constant pressure for 24 hours to allow the $CO_2$ gas to dissolve in the DI water in high pressure chamber 1. By closing valve #1, the $CO_2$ gas tank was disconnected from the system. In order to isolate the pressure chamber 1 and syringe from the microfluidic chip and take water with dissolved $CO_2$, valve #3 was closed. By closing valve #2 and opening valve #3, the solution was injected through the microfluidic chip. The solution was injected through the bottom inlet channel of the

(a)

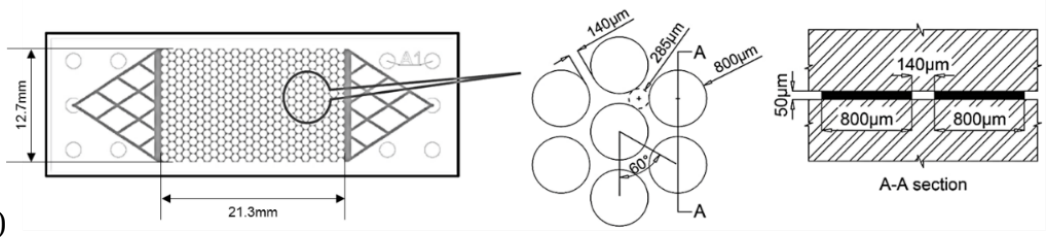


(b)

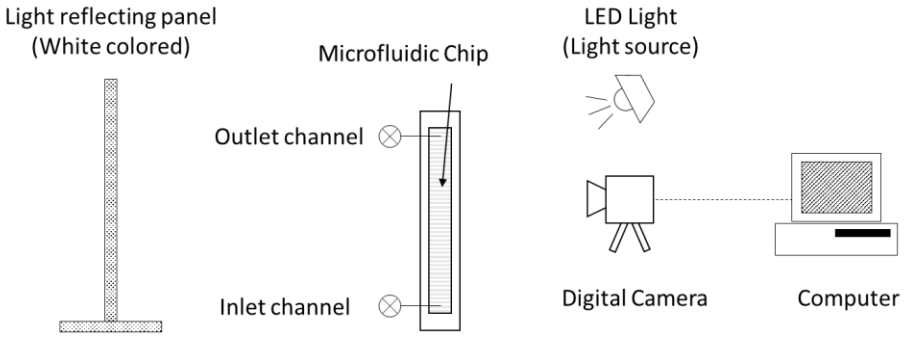


(c)

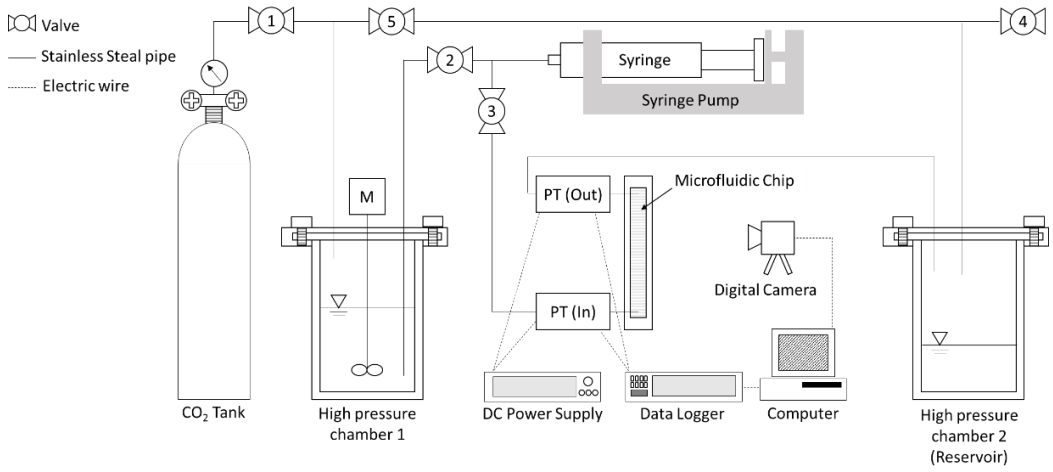


**Figure 5.1.** (a) Geometry of a patterned microfluidic chip (*Mahabadi et al.*, 2016; *Zheng et al.*, 2017), (b) Experimental configuration for biogenic gas formation in the microfluidic chip, (c) Experimental configuration for $CO_2$ gas formation in the microfluidic chip

microfluidic chip, and remaining liquid was expelled through the top outlet channel into the high pressure chamber #2. The total injected volume was significantly larger than the volume of the microfluidic chip (including connected tubings) to ensure that the entire volume of the chip was filled with the saturated $CO_2$ solution. Two pressure transducers (presented as PT in figure 1b) were connected to both inlet and outlet channels of the microfluidic chip. DC power supply (E3645A, Agilent) provided electric power source with 28V to operate pressure transducers. A data logger (34972A, Keysight) and computer were used to record pressure every 5 seconds. Depressurization of the system was initiated by opening valve #4.

### 5.2.4 Image Capture

Time-lapse imaging was performed using a digital camera (D5200, Nikon) equipped with a 60mm micro lens (AF-S Micro NIKKOR 60mm f/2.8G ED, Nikon). Four light sources (JANSJÖ flexible LED light, IKEA) and a white colored light reflecting panel were used to optimize light illumination. For the biogenic gas formation images were taken every 10 minutes at a resolution of 1920×1080 pixels, to allow for continuous monitoring of the evolution of gas formation within the microfluidic chip. Depressurization experiments were recorded using video mode at 25 frames per second and a full HD resolution of 1920×1080 pixels.

### 5.2.5 Image Processing Algorithm

Figure 5.2a shows the raw image from the biogenic gas formation experiment after denitrification reaction had been ongoing for 244 hours. The raw experimental images showed different phases, such as produced the gas bubbles or pockets, circular grains, and

pore space filled with reactive liquid solution. These features are highlighted in the cropped area from the original image (Figure 5.2b). In order to detect the gas bubbles and extract the volume information for the estimation of degree of saturation, a comprehensive image processing algorithm was developed using MATLAB (ver. R2017a). Figure 5.2c presents a sample of processed image in which the gas pocket within the pore space is well detected and is filled with green color. The detailed algorithm contained different stages. First the gray scale images were converted to binary images and consequently the different phases, solid, liquid and gas were separated in three steps: circular grains detection, gas bubble cluster detection, and gas bubble segmentation.

***Image binarization.*** Acquisition of desired information from the image requires the detection and segmentation of targeting objects in it. The original (raw) image (24-bit RGB color image) from the experiment consists of three n×m matrixes which includes values presenting three colors (Red, Green and Blue) and each matrix has a range of values from 0 to 255. Image binarization is one of the effective ways for building the base image for detection of targeting objective. Converting the RGB color image to the gray-scale image (8-bit intensity image) allows to store all the information into a single matrix that facilitates post image segmentation processes. In order to solidify the outlines of gas bubbles, the converted gray-scale image was turned into a black and white (0 and 1) binary image by using Otsu's method [1979]. Otsu's method selects a threshold and replaces values above this threshold with 1 (white) and values below the threshold with 0 (black) and can be carried out by using 'imbinarize' function in MATLAB (Figure 5.2d). Since the intensity values varied throughout the domain due to the inconstant illumination, threshold values

were selected locally using the ‘adaptive’ option, which results in automatic adjustment of the brightness.

***Step 1: Circular grains detection.*** The boundaries of the gas bubbles were clearly outlined in the binarized image (Figure 5.2d). But, the outlines also included the boundaries of circular grains, which needed to be removed. In order to do so, the binarized image was reversed (Figure 5.2e), then the ‘imfindcircle’ function in MATLAB was used to find circular grains (detected grains presented by red circles in Figure 5.2f). The center coordinates and diameter of circular grains were recorded and used for re-mapping the circular grains out on the same dimension matrix and generating a separate binary image containing the grains only (Figure 5.2h). The size of re-built circles slightly varies due to differences in the light intensity.

***Step 2: Gas bubble cluster detection.*** The gas bubble cluster located on the middle of the Figure 2d has a relatively large continuous skin boundary. This big cluster can be detected by using ‘bwareaopen’ function, which removes all connected objects fewer than a specified size (Figure 2g). The redrawn detected circular grains were masked onto the reversed image of Figure 2g. The resulting big bubble cluster without circular grains is plotted in Figure 2i.

***Step 3: Noise filtering.*** Small noises, which remained after detecting the circular grains and the gas bubble clusters in steps 1 and 2, were removed from Figure 2i by defining a size threshold value (Figure 5.2j). Few minor noises were still remained (see the circled area in Figure 5.2j), which potentially could affect the estimation of the gas volume. This noise is difficult to be removed by size thresholding since the noise is tiny and connected to an existing gas bubble cluster. Factitial noise was added (Figure 5.2k) and a 2D median

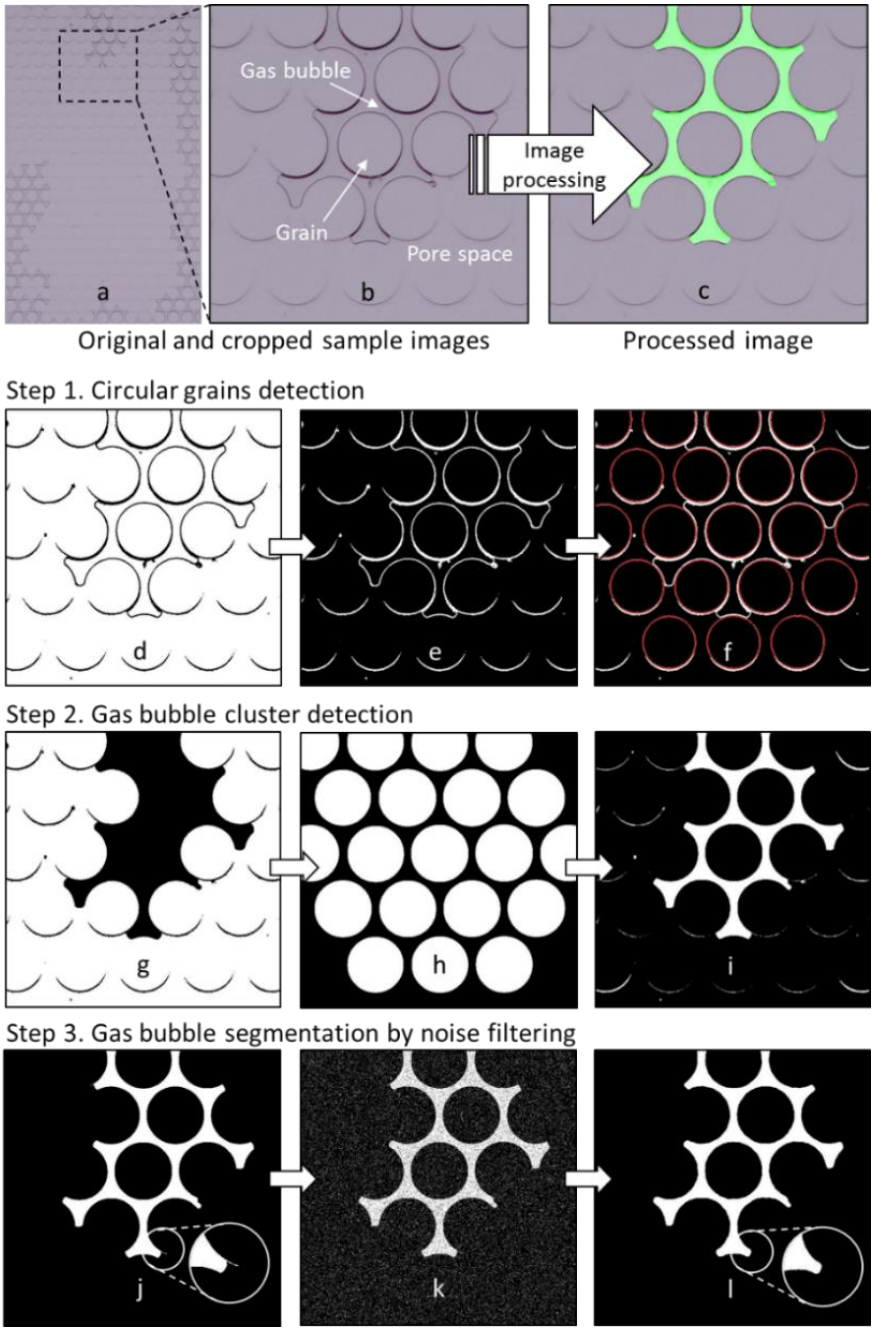


**Figure 5.2.** Gas bubbles extraction performed by the automated image processing (upper): Original experimental sample image (after 244 hours) showing the entire domain of microfluidic hip, cropped area from the sample image, and processed image based on the image segmentation (from the left to right). Image processing algorithm (lower): The algorithm mainly consists of three steps, circular grains segmentation, gas bubble phase detection, and noise filtering.

filter was used to remove this noise resulting in the final processed image shown in Figure 5.2l showing the bubble clusters in white color.

The number of pixels in all bubble clusters were counted and accumulated, then converted into the total bubble volume. It was assumed that the bubbles completely filled the entire depth of the microfluidic chip in this study. By using the automated image processing algorithm, several advantages were expected compared to the manual detection. As this algorithm kept the consistency for the phase segmentation and saved some processing time when analyzing a large number of images.

The constants used for the functions within this algorithm and some minor operations, needed some manual adjustments during the image analysis based on the color variation of experimental images and the characteristics of different bubbles. The developed MATLAB codes and constants used are provided in the supplementary material.

## 5.3 RESULTS AND DISCUSSION

### 5.3.1 Biogenic $N_2$ Gas Formation via Denitrification

Figure 5.3 shows a selection of images at several times and degrees of saturation with significant observations illustrating the different gas formation mechanisms that occurred during biogenic gas formation within the microfluidic chip. After 24 hours a first gas bubble appeared in the upper half of the domain, which is magnified in the black circle (Figure 5.3a). The gas bubble nucleated at the surface of circular grain, which was expected considering that the energy barrier for heterogeneous nucleation of gas bubbles on surfaces is significantly lower than homogeneous nucleation from solution. (e.g. *Jones et al.,* 1999; *Vachaparambil et al.,* 2018). The nucleated bubble grew as denitrification proceeded with

time. The initial nucleation had a circular shape in 2D plane view, and it kept the shape until it filled the entire pore space between three grains. Then, the bubble continued to

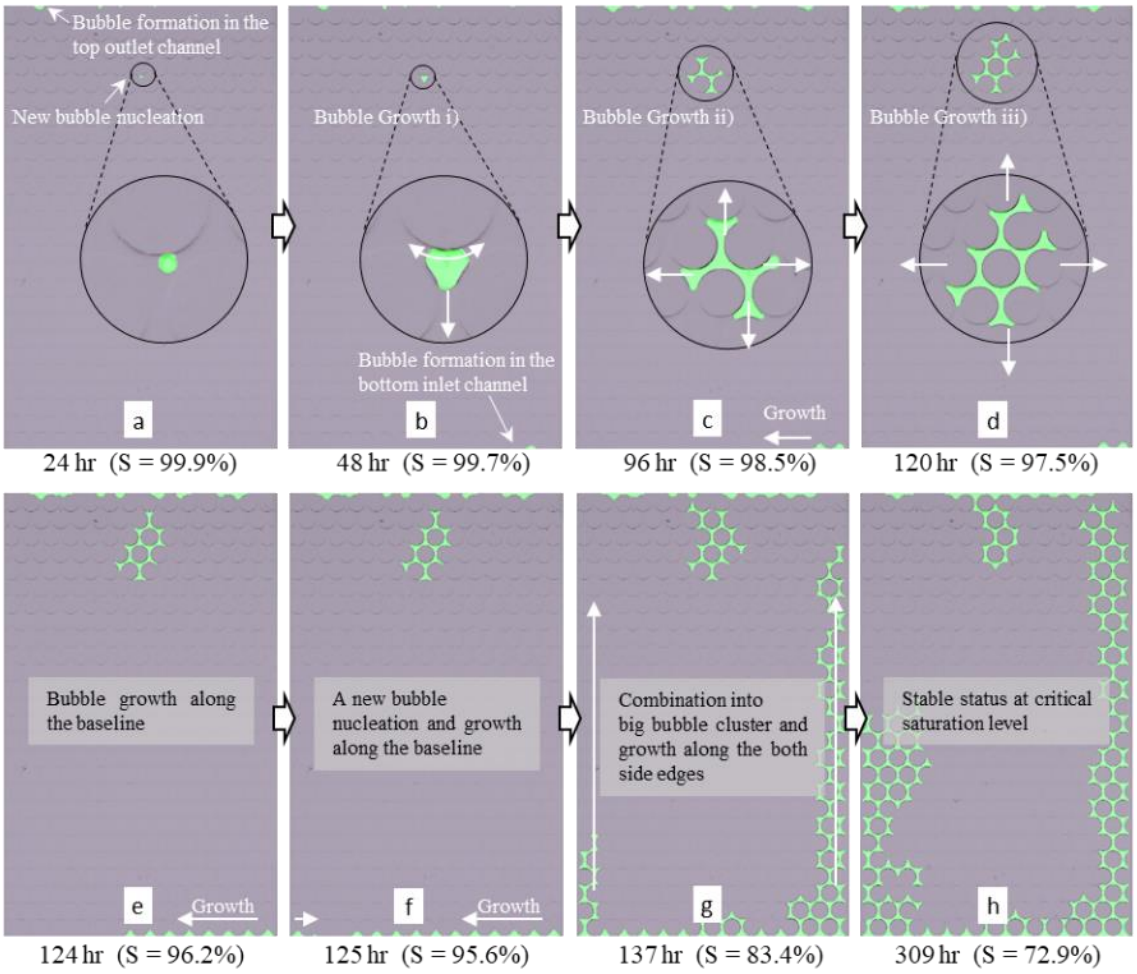


**Figure 5.3.** Visualization of the mechanisms of biogenic gas bubble formation and growth within the microfluidic

expand in all three directions and gradually fill up the connected pore throats (Figure 5.3b ~ 5.3d). Once the bubble reaches the gas pressure and tends to go up as the radius of the bubble needs to decrease in order to squeeze through the pore throat. Follow the Young-Laplace equation the capillary pressure is inversely proportional to the bubble radius. Once bubble reaches the narrowest point of the pore throat, the bubble was expected to expand

rapidly filling up the neighboring pore, while the capillary pressure decreases, through a process referred to as Haines jumps (e.g. *Armstrong et al.,* 2015). However, in this experiment the expansion was more gradual, which could be attributed to the relatively large pore throat size in comparison to the thickness of the microfluidic chip. Since the pore throat width is larger than the thickness of the microfluidic chip, the capillary pressure, which is controlled by the smallest radius remains constant. The direction of the gas phase expansion is affected by the pore throat size and buoyancy. Similar pore and pore throat sizes in the micromodel stimulate a gradual isotropic expansion, while buoyancy may cause bubbles to gradually migrate upward.

In the meantime, other gas bubbles appeared at the top (outlet) and bottom (inlet) channels. These channels were relatively larger pore spaces designed for the homogenous distribution of injection fluid (Figure 5.1a). As these bubbles were expanding laterally along the boundaries they were forming a large gas pocket filling up the entire inlet channel. After the inlet channel at the bottom was completely filled, the big gas pocket expanded relatively fast upwards along the side boundaries. These observations corresponded with previous studies on biogenic gas formation via denitrification within the soil columns, which showed that the produced gas pockets were predominantly in coarser layers and in limited wider channels from the top and bottom through the finer sand (*Mahabadi et al.,* 2018; *Nakano,* 2018; *Pham et al.,* 2016). Once the gas filled channels along the sides of the microfluidic chip reached the channel at the top, the gas rapidly vented upward, leaving some disconnected gas pockets along the side of the microfluidic chip, which gradually reconnected again, while the gas continued to be formed. This

process of rapid venting followed by gradual upward displacement and reconnection of disconnected gas pockets repeated several times until the end of the experiment.

As the volume of gas increased with time the degree of saturation decreased. The initial degree of saturation starts from 100 % since the microfluidic chip was fully saturated with the substrate solution at the start of the experiment. The degree of saturation with time is presented in Figure 5.4. The decrease in saturation during the first 124 hours could be attributed to the growth of a single bubble. The bubble size increased exponentially as expected for the biological conversion, which results in an increase in biomass catalyzing the formation of biogas. After 125 hours (Figure 5.3f), the degree of saturation rapidly decreased corresponding to the rapid gas invasion along the sides of the chip. This faster gas formation is clearly observed in Figure 5.4, in which the degree of saturation is significantly drops to reach a minimum value of 75 %. The invasion of gas along the sides

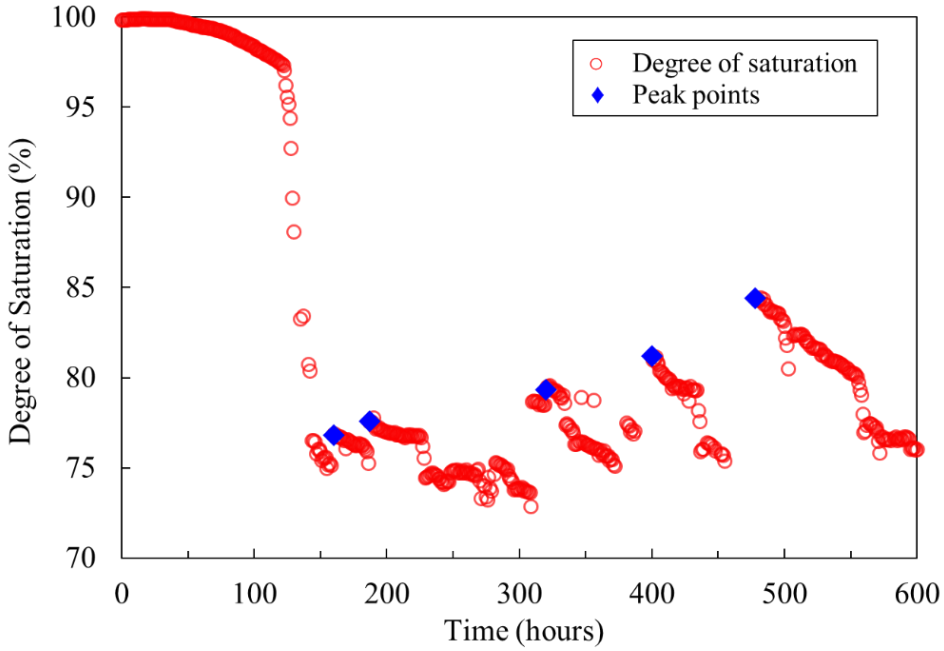


**Figure 5.4.** Degree of saturation with time by biogenic $N_2$ gas formation within the microfluidic chip

could be driven by biological activity in the tubing upstream of the microfluidic chip, in which any generated gas would expel the liquid or gas downstream through the microfluidic chip towards the outlet. The degree of saturation started fluctuating, after the invading gas reached the gas pocket at the top boundary at which rapid increase in saturation level corresponding to venting of the gas were followed by gradual decrease, when the gas was gradually migrating upward again. The first and following peaks during the reaction are masked by blue diamonds in Figure 5.4. During these fluctuations the degree of saturation remained between 75 and 85 %.

### 5.3.2 $CO_2$ Gas Formation via Depressurization

$CO_2$ gas formation experiment through rapid depressurization showed significantly different gas formation and migration mechanisms than the slow biogenic gas formation, which affected the equilibrated degree of saturation and gas distribution pattern. Before the pressure was released some air, bubbles were trapped along the side edges of domain during the injection phase. These trapped bubbles played a role in phase changes of dissolved $CO_2$ gas. As shown in Figure 5.5 rapid depressurization caused nucleation and growth of many small air bubbles throughout the microfluidic chip. Within the first 3 seconds nucleation of new bubbles and growth of existing gas bubbles predominantly occurred along the sides of the microfluidic chip. In case of depressurization growth of gas bubbles can be attributed to a drop in pressure, causing the gas to expand following the ideal gas law. Some of the smaller bubbles migrated upward. Particularly in the center and close to the top of the microfluidic chip, migration was faster than near the bottom and along the edges migration.

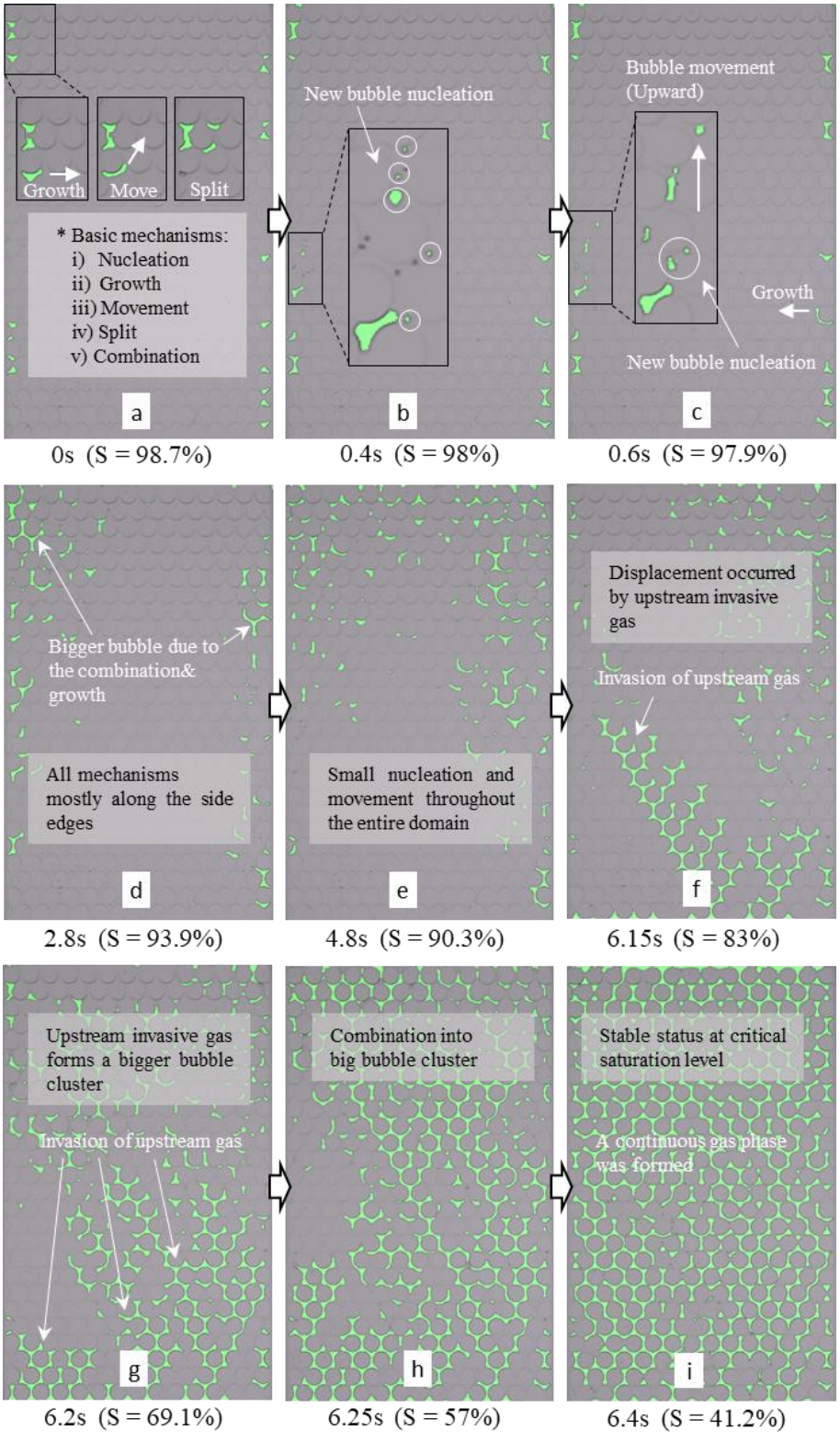


**Figure 5.5.** Visualization of the mechanisms of $CO_2$ gas formation and growth within the microfluidic (by quick pressure release)

Upward migration of gas bubbles could be attributed to buoyancy, allowing small bubbles to pass through freely, pressure gradients, stimulating gas to flow to the outlet or advection by the liquid phase being flushed from bottom to top potentially being expelled by gas formation in the tubing upstream from the microfluidic chip. Also splitting of bubbles into multiple smaller bubbles coalescence of bubbles and formation of larger bubbles was observed (Black box in Figure 5.5a), similar to observations by *Mahabadi & van Paassen* (2018). As the pressure dropped down with time, more gas bubbles were nucleating, also in the upper part of the domain (Figure 5.5b and 5.5c). During the first 4.8 seconds the degree of saturation gradually decreased to 90.3 % as a result gas nucleation and growth (Figure 5.6). However, between 4.8 and 6 seconds the degree of saturation remained constant as the volume of newly formed gas was equal to the volume of gas venting through

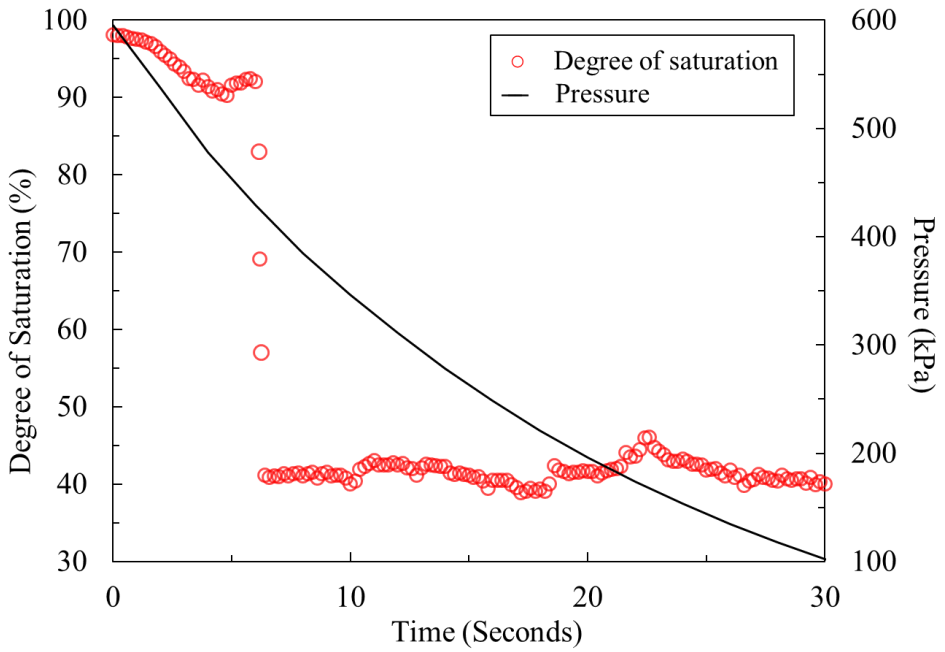


**Figure 5.6.** Degree of saturation change by $CO_2$ gas formation (by quick pressure release) within the microfluidic chip

the outlet. Between 6 and 6.4 seconds rapid upward migration of upstream invasive gas was observed (Figure 5.5f), which caused a sudden drop in the degree of saturation from 92 to 41.2 %. Migration took place through several channels (Figure 5.5g). After the displacing gas reached the outlet, a continuous gas phase was formed from bottom to top (Figure 5.5h & i). Although some minor migration of gas was still observed, the saturation did not change upon further pressure drop after 6.4 second. The degree of saturation remained about 40 % during the remainder of the experiment.

Compared to the fast depressurization experiment, the slow depressurization experiment showed a system, which was dominated by gas displacement (Figure 5.7). However, the gas displacement pattern was different than the displacement in the case of biogenic gas formation or the fast depressurization. Similar to the fast depressurization some gas bubbles were trapped during the injection phase, which started to grow when the depressurization was initiated. However, after 15 seconds gas bubble formation was observed at the bottom of the domain. A stable gas front migrated upward displacing most of the liquid, until it reached the top side of the microfluidic chip after 33 seconds, forming a continuous gas phase from bottom to top and reaching an equilibrated degree of saturation of about 35.6 %.

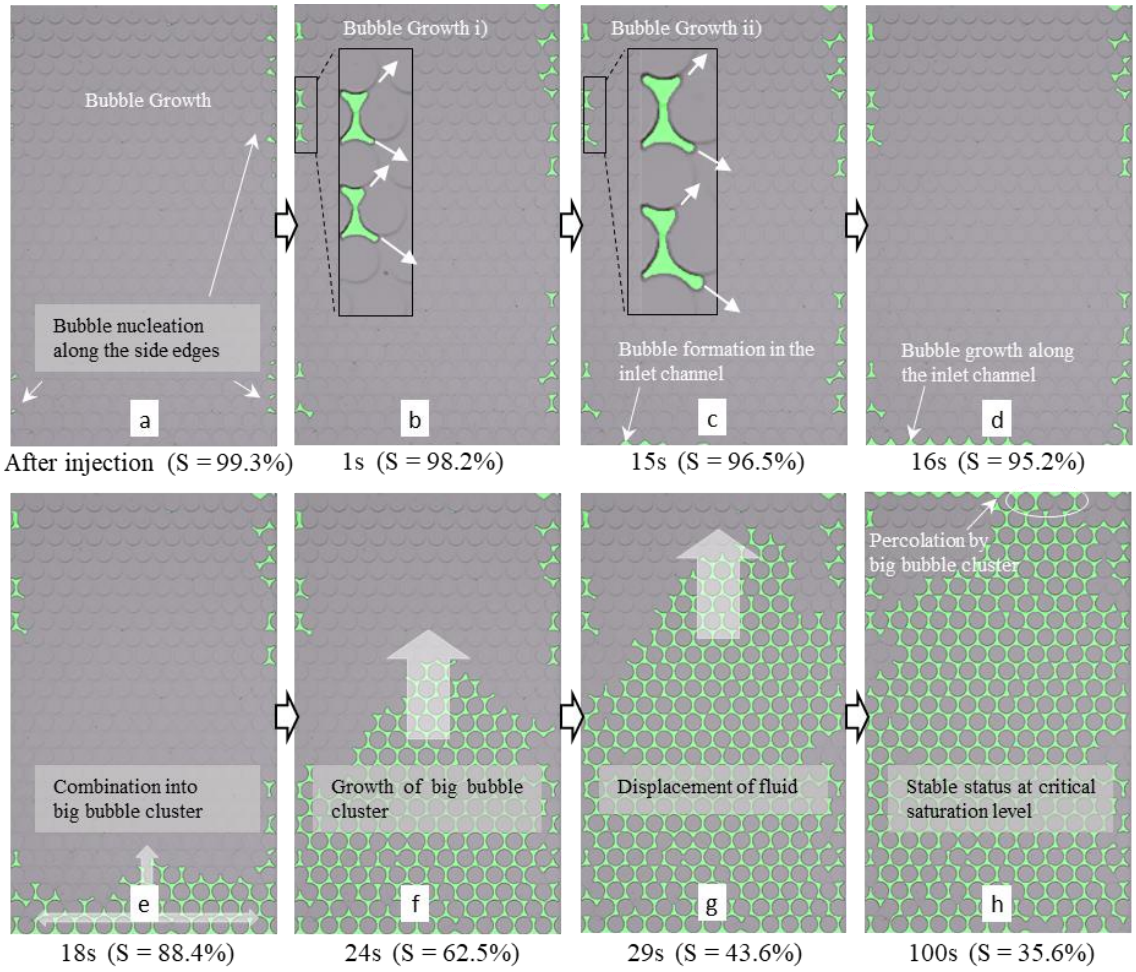


**Figure 5.7.** Visualization of the mechanisms of $CO_2$ gas formation and growth within the microfluidic (by slower pressure release)

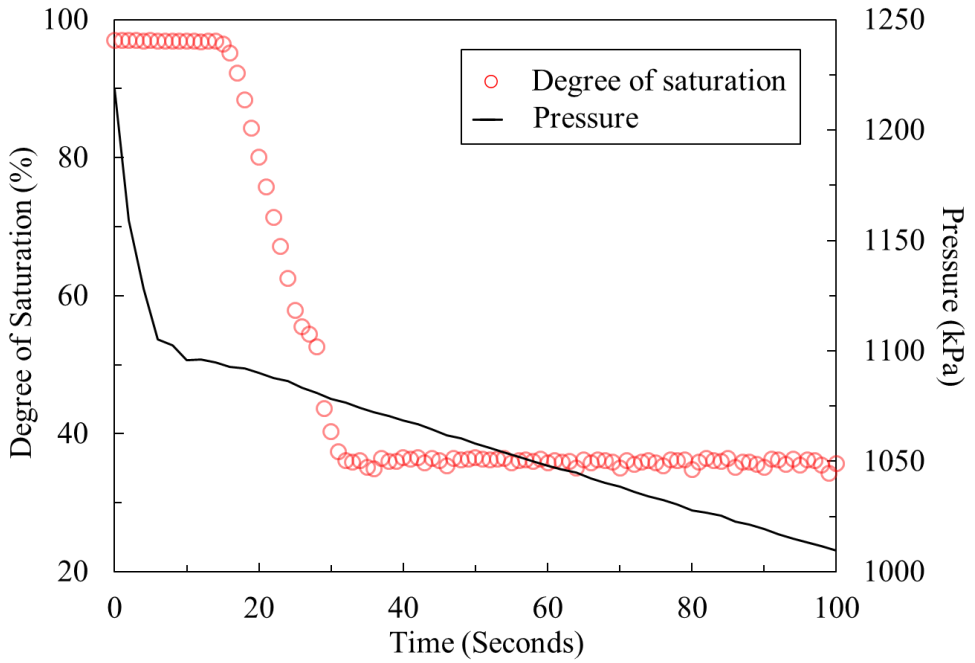


**Figure 5.8.** Degree of saturation change by $CO_2$ gas formation (by slower pressure release) within the microfluidic chip

### 5.3.3 Comparison, Interpretation and Limitations

Comparing the three experiments clearly shows differences in the gas bubble formation and migration mechanisms:

1. Biogenic gas production showed a single nucleated bubble and slow growth, followed by displacement along the sides, resulting in heterogeneous gas distribution at 75 to 80 % of equilibrated water saturation.
2. Rapid depressurization resulted in rapid nucleation and growth of many bubbles and migration of single bubbles, followed by rapid displacement through several branches, resulting in a homogeneously distributed gas phase, at an equilibrated water saturation of about 40 %.

3. Slow depressurization did not show any nucleating gas bubbles and showed limited growth, followed by stable displacement and resulting in a homogeneous gas distribution at an equilibrated degree of saturation of 35.6 %

In all three cases gas displacement appeared to be the dominant mechanism reducing the degree of saturation. The gas displacement mechanism depends on capillary number, viscosity ratio and bond number. Assuming the viscosity of water at $8.9\times10^{-4}$ [Pa s] (*Korson et al.,* 1978) and viscosities of nitrogen gas and carbon dioxide gas at $1.76\times10^{-5}$ [Pa s] (*Johnston et al.,* 1951) and 1. $74\times10^{-5}$ [Pa s] (*Phillips,* 1912), the viscosity ratio is estimated at $1.57\times10^{-2}$. Considering gas displacement velocities can be estimated at $9.3\times10^{-11}$, $2.5\times10^{-7}$, $1.4\times10^{-4}$ [m $s^{-1}$] for the three listed experiments by dividing the change in gas volume during displacement, by the cross-sectional area of the microfluidic chip and the total displacement time and assuming a surface tension of 72 [N $m^{-1}$], capillary numbers are estimated at $2.30\times10^{-12}$, $6.20\times10^{-9}$, and $3.41\times10^{-6}$ for case 1, 2 and 3 respectively. At these low capillary numbers and low viscosity ratios capillary fingering or viscous fingering is expected to be the dominant displacement mechanism (*Cao et al.,* 2016; *Mahabadi et al.,* 2019). Assuming the characteristic length $L$ is $2.5\times10^{-5}$ m, equal to minimum radius of the gas bubbles, which is limited by the thickness of the microfluidic chip, and a gas density of 0.8 [kg $m^{-3}$] and water density of $1\times10^{3}$ [kg $m^{-3}$], the Bond number is estimated at $8.5\times10^{-5}$, which is significantly lower than 3.37, indicating that once a gas bubble gets trapped it will not migrate due to buoyancy alone. Instead it is expected that migration of larger gas bubbles is the result of bubble growth or induced inertia or hydraulic pressure of upstream invading fluids.

Although different formation and migration mechanisms and a relation between the gas formation rate, the different mechanisms and equilibrated degree of saturation and gas distribution have been identified, the observed displacement mechanisms do not fully correspond with the expectations. Further study and experiments are required to explain the observed displacement mechanisms.

Part of the discrepancy between theory and observation may be attributed to limitations of the experimental set up and procedure. For example, the thickness of the microfluidic chip is smaller than the pore throat radius, which may affect the migration of the gas phase, resulting in a gradual displacement, without irregular Haines jumps. The regular pore geometry and extremely uniform pore throat size distribution may affect the displacement mechanism, as shown by *Mahabadi et al.* (2019). The pore geometry should be modified in other to better reflect the pore size distribution in an actual soil and establish a more quantitative assessment of the relation between gas production rate and equilibrated degree of saturation. Another aspect which is not taken into account is the limited pore size in fine grained soils and likely stratification in natural sediments. Biogenic gas bubbles may not be able to form in fine grained soils, since there may be a mechanical constraint limiting the activity or penetration of gas producing bacteria (*Rebata-Landa & Santamarina*, 2006) and the pore size may not allow bubbles to remain stable since the gas pressure and related equilibrium concentration increase with a decreasing bubble radius. On the other hand, formation of gas may also generate macro-pores, fractures or cracks in sediments, as shown by *Pham et al.* (2017), allowing the gas to fill larger pockets. Stratification in soils may prevent gas to migrate upward through finer grained soil layers

and spread downward sideways through coarser grained layers, resulting in variable degrees of saturation related to pore size.

## 5.4 CONCLUSIONS

Experiments in a microfluidic chip have demonstrated that the gas formation mechanism and resulting gas distribution and degree of saturation are affected by the gas formation rate. In a regular porous medium biogenic gas formation is relatively slow, which limits the amount of nucleating gas bubbles and stimulates growth of existing gas bubbles filling multiple pores and gradually reducing the degree of saturation and migrating upward as a result of buoyancy. Displacement of water by invading gas from the bottom is the major factor reducing the equilibrated degree of saturation, fluctuating between 75 and 85 %, which corresponds to other experiments using sand columns. Fast gas formation due to depressurization of a saturated $CO_2$ solution resulted in a more homogeneously distributed gas phases and lower degree of saturation, in which the displacement was also the dominant factor reducing the degree of saturation.

**Acknowledgments**

Work described herein was supported in part by the National Science Foundation (NSF) Engineering Research Center program under the grant numbered ERC-1449501. Any opinions, findings and conclusions or recommendations expressed in this material are those of the authors and do not necessarily reflect those of the NSF.

# CHAPTER 6

# CONCLUSIONS AND RECOMMENDATIONS

## 6.1 OVERVIEW

The potential of using bio-geo-chemical processes for applications in geotechnical engineering has been widely explored in order to overcome the limitation of traditional ground improvement techniques. Pioneers in this field of research have found opportunities to use microbial activities in the subsurface. Biomineralization via urea hydrolysis, referred to as Microbial or Enzymatic Induced Carbonate Precipitation (MICP/EICP), has been shown to increase soil strength by stimulating precipitation of calcium carbonate minerals, bonding soil particles and filling the pores. Microbial Induced Desaturation and Precipitation (MIDP) via denitrification has also been studied for its potential to stabilize soils through mineral precipitation, but also through production of biogas, which can mitigate earthquake induced liquefaction by desaturation of the soil.

The processes of MICP, EICP or MIDP have been extensively studied and empirical relationships have been established between the engineering properties of treated soils such as soil strength and permeability and the overall amount of biomineral and biogas formation. However, these empirical relationships may significantly vary depending on the biomineral and biogas formation patterns including the location, size, and distributions, which require to be examined with pore-scale studies. This research will focus on the pore-scale characterization of biomineral and biogas formations in porous medium.

In this study, the pore-scale characteristics of calcium carbonate precipitation via EICP and biogenic gas formation via MIDP were explored by visual observation in a

transparent porous media using a microfluidic chip at a larger scale. For this purpose, an imaging system was designed and image processing algorithms were developed to analyze the experimental images and detect the nucleation and growth precipitated minerals and formation and migration of gas bubbles within the microfluidic chip. Statistical analysis was performed based on the processed images to assess the evolution of biomineral size distribution, the number of precipitated minerals and degree of saturation over time due to the gas formation. The experimental results and image analysis provide insight in the kinetics of the precipitation process and gas formation and distribution.

## 6.2 CONCLUSIONS

*Biomineral formation in porous media: An experimental study*

- Enzymatically induced calcium carbonate precipitation (EICP) by urea hydrolysis has been studied using a microfluidic chip experiment. The precipitation of $CaCO_3$ minerals was monitored by time sequential images. An image processing algorithm was developed to analyze the experimental images, assess the characteristics of the biominerals, and gain insight in the precipitation mechanisms and the kinetics of crystal nucleation and growth.
- Despite a limited resolution, the cumulative crystal volume and bulk precipitation rate could be determined and corresponded reasonably well with values predicted with a simplified numerical model.
- The assumed crystal shape in the image analysis procedure significantly affected the calculated volume of crystals. Assuming a cylindrical crystal shape overestimates the crystal volume, particularly when the crystals are smaller than

the internal thickness of the microfluidic chip. Assuming a semi-spherical crystal shape, the cumulative crystal volume and bulk precipitation rate, were lower than expected and gradually decreased with an increasing number of cycles. This decrease can partly be attributed to local pore clogging, which reduces the mobile allowing a lower amount of substrate solution to be retained in the pore volume.

- The calculated supersaturation was relatively high, which could explain the fact that new crystals were observed in each treatment cycle. However, when comparing the results with classical nucleation theory, it was found that for the calculated supersaturation the observed 'nucleation rate' was lower than expected. The difference between theoretical predictions and experimental data emphasizes the difficulty to accurately predict the pore-scale characteristics of biominerals directly.

*Biomineral formation in porous media: A hybrid experiment-numerical study*

- A hybrid experimental-numerical approach is used in this study to get insight about micro-scale processes of biomineralization and its associated impacts on the behavior of porous media such as the evolution of pore structure and development of immobile pore zones.
- The total porosity linearly decreases with the increase in the number of treatment cycles while the mobile porosity significantly reduces following a parabolic function. The reduction in mobile porosity due to calcium carbonate precipitation, and the resulting changes in the hydraulic flow field significantly affect the transport and distribution of solute substrates during subsequent injections. The concentration profile forms a completely uniform front displacing the water out of

the crystal-free porous media in the non-treated case, while as the level of mineral precipitation increases, the heterogeneity of the transport patterns increases. The simulation results demonstrate that higher degree of calcite precipitation results in development of fringe patterns and faster transport of substrate through the porous media.

- Using only the total porosity in Kozeny-Carman equation leads to a significant overestimation of permeability. The estimated permeability by KC-General model is reduced by only 25 % after 10 cycles of treatment while the numerical results shows up to 80 % permeability reduction. Although adding the tortuosity change to the Kozeny-Carman equation (KC-Tortuosity) improves the accuracy of the results, still there is a meaningful discrepancy between the permeability values. Particularly, as the level of precipitation rises, the difference between the direct calculation of permeability (CFD numerical results) and the predicted permeability by KC-Tortuosity escalates. This is in agreements with that the Kozeny-Carman equation may significantly overestimate the permeability, particularly in complex, heterogeneous, and poorly connected porous media. By inserting the mobile porosity into the Kozeny-Carman equation, even by ignoring the tortuosity changes, the permeability can be estimated accurately.
- In the field scale, the mobile porosity can be measured relatively easy by injecting a trace fluid and recording the residence time of the effluent. The fitting parameter of power-law equation were calculated $\eta$=3.6 for the KC-General while the realistic fitting parameter is considerably higher, $\eta$=20.2.

*Biogenic gas formation in porous media: A comparative study with $CO_2$ gas formation via depressurization*

- Experiments in a microfluidic chip have demonstrated that the gas formation mechanism and resulting gas distribution and degree of saturation are affected by the gas formation rate.
- In a regular porous medium biogenic gas formation is relatively slow, which limits the amount of nucleating gas bubbles and stimulates growth of existing gas bubbles filling multiple pores and gradually reducing the degree of saturation and migrating upward as a result of buoyancy.
- Displacement of water by invading gas from the bottom is the major factor reducing the equilibrated degree of saturation, fluctuating between 75 and 85 %, which corresponds to other experiments using sand columns.
- Fast gas formation due to depressurization of a saturated $CO_2$ solution resulted in a more homogeneously distributed gas phases and lower degree of saturation, in which the displacement was also the dominant factor reducing the degree of saturation.

## 6.3 RECOMMENDATIONS FOR FURTHER STUDY

In this study, the microfluidic chip simulating a homogenous porous media was used. The microfluidic chip can also be designed to represent a realistic pore distribution of soils using a cross section of X-ray CT image. Based on the objectives, various designs and types of microfluidic chip can be selected.

The imaging system using a digital camera with micro-lens in this study has a limitation on the resolution to observe a single bacteria or tiny nucleation of crystal or bubble. Depending on the targeting observation objectives, different imaging tool can be used, such as confocal microscope or high-speed video camera.

This study has shown that despite its limitations, visualization using microfluidic chip is a useful method to assess the pore scale characteristics of mineral and gas formations in porous media. The proposed procedure can be used for:

- Optimization in MICP/EICP/MIDP treatment strategies or validation of numerical models by analyzing the effect of different substrates and bacteria/enzyme activity/concentrations.
- Quantification of relationships between pore-scale crystal/gas characteristics and continuum scale 'engineering' parameters of porous media, such as porosity and permeability.
- Combined experimental studies with conventional compressive testing in order to correlate pore-scale crystal/gas characteristics to column-scale 'engineering' parameter of soils, such as compressive and shear strength.

# REFERENCES


Aharonov, E., Rothman, D. H., & Thompson, A. H. (1997). "Transport properties and diagenesis in sedimentary rocks: The role of micro-scale geometry." *Geology*, *25*(6), 547-550.

Almajed, A., Tirkolaei, H. K., Kavazanjian, E., & Hamdan, N. (2019). "Enzyme Induced Biocementated Sand with High Strength at Low Carbonate Content." *Scientific Reports*, 9(1), 1135.

Al-Thawadi, S., & Cord-Ruwisch, R. (2012). "Calcium carbonate crystals formation by ureolytic bacteria isolated from Australian soil and sludge." *J. Adv. Sci. Eng. Res*, *2*(1), 12-26.

Al Qabany, A., Soga, K., & Santamarina, C. (2011). "Factors affecting efficiency of microbially induced calcite precipitation." *Journal of Geotechnical and Geoenvironmental Engineering*, 138(8), 992–1001.

Armstrong, R. T., Evseev, N., Koroteev, D., & Berg, S. (2015). "Modeling the velocity field during Haines jumps in porous media." *Advances in Water Resources*, 77: 57-68.

Barkouki, T. H., Martinez, B. C., Mortensen, B. M., Weathers, T. S., De Jong, J. D., & Ginn, T. R., et al. (2011). "Forward and inverse bio-geochemical modeling of microbially induced calcite precipitation in half-meter column experiments." *Transport in Porous Media*, 90(1), 23.

Bear, J., Braester, C., & Menier, P. C. (1987). "Effective and relative permeabilities of anisotropie porous media." *Transport in porous media*, *2*(3), 301-316.

Bernabé, Y., Mok, U., & Evans, B. (2003). "Permeability-porosity relationships in rocks subjected to various evolution processes." *Pure and Applied Geophysics*, *160*(5-6), 937-960.

Bernard, J. P., Adrich, Z., Montalto, G., De Caro, A., De Reggi, M., Sarles, H., & Dagorn, J. C. (1992). "Inhibition of nucleation and crystal growth of calcium carbonate by human lithostathine." *Gastroenterology*, 103(4), 1277–1284.

Bretherton, F. P. (1961). “The motion of long bubbles in tubes.” *Journal of Fluid Mechanics*, 10(2), 166-188.

Burbank, M., Kavazanjian, E., Weaver, T., Montoya, B. M., Hamdan, N., & Bang, S. S., et al. (2013). “Biogeochemical processes and geotechnical applications: progress, opportunities and challenges.” *Géotechnique*, 63(4), 287–301. https://doi.org/10.1680/geot.SIP13.P.017

Canny, J. (1986). “A computational approach to edge detection.” *IEEE Transactions on Pattern Analysis and Machine Intelligence*, (6), 679–698.

Cao, S. C., Dai, S., & Jung, J. (2016). “Supercritical CO2 and brine displacement in geological carbon sequestration: Micromodel and pore network simulation studies.” *International Journal of Greenhouse Gas Control*, *44*, 104-114.

Carman, P. C. (1948). “Some physical aspects of water flow in porous media.” *Discussions of the Faraday Society*, *3*, 72-77.

Carroll, S., Hao, Y., Smith, M., & Sholokhova, Y. (2013). “Development of scaling parameters to describe CO2–rock interactions within Weyburn-Midale carbonate flow units.” *International Journal of Greenhouse Gas Control*, *16*, S185-S193.

Charlton, S. R., & Parkhurst, D. L. (2011). “Modules based on the geochemical model PHREEQC for use in scripting and programming languages.” *Computers & Geosciences*, 37(10), 1653–1663.

Civan, F. (2001). “Scale effect on porosity and permeability: Kinetics, model, and correlation.” *AIChE journal*, *47*(2), 271-287.

Clement, T. P., Wise, W. R., Molz, F. J., & Wen, M. (1996). “A comparison of modeling approaches for steady-state unconfined flow.” Journal of Hydrology, 181(1-4), 189-209.

Colón, C. F. J., Oelkers, E. H., & Schott, J. (2004). “Experimental investigation of the effect of dissolution on sandstone permeability, porosity, and reactive surface area.” *Geochimica et Cosmochimica Acta*, *68*(4), 805-817.

Connolly, J., Kaufman, M., Rothman, A., Gupta, R., Redden, G., Schuster, M., Colwell, F., & Gerlach, R. (2013). "Construction of two ureolytic model organisms for the study of microbially induced calcium carbonate precipitation." *Journal of microbiological methods*, 94(3), 290-299.

Cunningham, A. B., Gerlach, R., Spangler, L., & Mitchell, A. C. (2009). "Microbially enhanced geologic containment of sequestered supercritical CO2." *Energy Procedia*, 1(1), 3245–3252.

Cunningham, A. B., Gerlach, R., Spangler, L. M., Mitchell, A. C., Parks, S., & Phillips, A. J. (2011). "Reducing the risk of well bore leakage using engineered biomineralization barriers." *Energy Procedia*, 4, 5178–5185.

Cuthbert, M. O., Riley, M. S., Handley-Sidhu, S., Renshaw, J. C., Tobler, D. J., Phoenix, V. R., & Mackay, R. (2012). "Controls on the rate of ureolysis and the morphology of carbonate precipitated by S. Pasteurii biofilms and limits due to bacterial encapsulation." *Ecological Engineering*, 41, 32–40.

Dalas, E., Kallitsis, J., & Koutsoukos, P. G. (1988). "The crystallization of calcium carbonate on polymeric substrates." *Journal of Crystal Growth*, 89(2–3), 287–294.

Dawe, R. A., & Zhang, Y. (1997). "Kinetics of calcium carbonate scaling using observations from glass micromodels." *Journal of Petroleum Science and Engineering*, 18(3-4), 179-187.

DeJong, J. T., Mortensen, B. M., Martinez, B. C., & Nelson, D. C. (2010). "Bio-mediated soil improvement." *Ecological Engineering*, 36(2), 197–210.

Doyen, P. M. (1988). "Permeability, conductivity, and pore geometry of sandstone." *Journal of Geophysical Research: Solid Earth*, *93*(B7), 7729-7740.

Ebigbo, A., Phillips, A., Gerlach, R., Helmig, R., Cunningham, A. B., Class, H., & Spangler, L. H. (2012). "Darcy-scale modeling of microbially induced carbonate mineral precipitation in sand columns." *Water Resources Research*, *48*(7).

El Mountassir, G., Minto, J. M., van Paassen, L. A., Salifu, E., & Lunn, R. J. (2018). "Applications of microbial processes in geotechnical engineering." *Advances in applied microbiology* (Vol. 104, pp. 39-91). Academic Press.

Fauriel, S., & Laloui, L. (2012). “A bio-chemo-hydro-mechanical model for microbially induced calcite precipitation in soils.” *Computers and Geotechnics*, *46*, 104-120.

Ferris, F. G., Phoenix, V., Fujita, Y., & Smith, R. W. (2004). “Kinetics of calcite precipitation induced by ureolytic bacteria at 10 to 20 C in artificial groundwater.” *Geochimica et Cosmochimica Acta*, 68(8), 1701–1710.

Fidaleo, M., & Lavecchia, R. (2003). “Kinetic study of enzymatic urea hydrolysis in the pH range 4-9.” *Chemical and biochemical engineering quarterly*, *17*(4), 311-318.

Fujita, Y., Redden, G. D., Ingram, J. C., Cortez, M. M., Ferris, F. G., & Smith, R. W. (2004). “Strontium incorporation into calcite generated by bacterial ureolysis1.” *Geochimica et Cosmochimica Acta*, 68(15), 3261–3270.

Gal, J.-Y., Bollinger, J.-C., Tolosa, H., & Gache, N. (1996). “Calcium carbonate solubility: a reappraisal of scale formation and inhibition.” *Talanta*, 43(9), 1497–1509.

Garing, C., Gouze, P., Kassab, M., Riva, M., & Guadagnini, A. (2015). “Anti-correlated porosity–permeability changes during the dissolution of carbonate rocks: experimental evidences and modeling.” *Transport in Porous Media*, *107*(2), 595-621.

Graf, D. L. (1961). “Crystallographic tables for the rhombohedral carbonates.” *American Mineralogist: Journal of Earth and Planetary Materials*, 46(11-12), 1283-1316.

Hamdan, N., & Kavazanjian, E. (2016). “Enzyme-induced carbonate mineral precipitation for fugitive dust control.” *Géotechnique*, 66(7), 546–555.

Hammes, F., & Verstraete, W. (2002). “Key roles of pH and calcium metabolism in microbial carbonate precipitation.” *Reviews in Environmental Science and Biotechnology*, 1(1), 3–7.

Hammes, F., Boon, N., de Villiers, J., Verstraete, W., & Siciliano, S. D. (2003). “Strain-specific ureolytic microbial calcium carbonate precipitation.” *Appl. Environ. Microbiol.*, 69(8), 4901–4909.

Hao, Y., Smith, M., Sholokhova, Y., & Carroll, S. (2013). "CO2-induced dissolution of low permeability carbonates. Part II: Numerical modeling of experiments." *Advances in water resources, 62*, 388-408.

He, J. (2013). "Mitigation of liquefaction of sand using microbial methods." Nanyang Technological University.

Hill, C. A., & Forti, P. (1997). "Cave minerals of the world (2nd edition)." National Speleological Society, Huntsville, Alabama.

Helmig, R., Flemisch, B., Wolff, M., Ebigbo, A., & Class, H. (2013). "Model coupling for multiphase flow in porous media." *Advances in Water Resources, 51*, 52-66.

Hommel, J., Coltman, E., & Class, H. (2018). "Porosity–permeability relations for evolving pore space: a review with a focus on (bio-) geochemically altered porous media." *Transport in Porous Media*, *124*(2), 589-629.

Hommel, J., Ebigbo, A., Gerlach, R., Cunningham, A. B., Helmig, R., & Class, H. (2016). "Finding a balance between accuracy and effort for modeling biomineralization." *Energy Procedia*, 97, 379–386.

Hommel, J., Lauchnor, E., Phillips, A., Gerlach, R., Cunningham, A. B., Helmig, R., et al. (2015). "A revised model for microbially induced calcite precipitation: Improvements and new insights based on recent experiments." *Water Resources Research*, 51(5), 3695–3715.

Johnston, H. L., Mattox, R. W., & Powers, R. W. (1951). "Viscosities of air and nitrogen at low pressures." *National Advisory Committee for Aeronautic*, TECHNICAL NOTE 2546.

Jones, S. F., Evans, G. M., & Galvin, K. P. (1999). "Bubble nucleation from gas cavities—a review." *Advances in colloid and interface science*, *80*(1), 27-50.

Kavazanjian, E., O'Donnell, S. T., & Hamdan, N. (2015). "Biogeotechnical mitigation of earthquake-induced soil liquefaction by denitrification: A two-stage process." In *Proceedings of 6th International Conference on Earthquake Geotechnical Engineering, Christchurch, New Zealand* (pp. 20-28).

Kim, D., Mahabadi, N., Hall, C., Jang, J., & van Paassen, L. A. (2017). "Characterization of Calcite Mineral Precipitation Process by EICP in Porous Media." In *AGU Fall Meeting* Abstracts.

Kim, D., Mahabadi, N., Jang, J., & van Paassen, LA. (*Under review*). "Assessing the Kinetics and Pore Scale Characteristics of Biological Calcium Carbonate Precipitation in Porous Media using a Microfluidic Chip Experiment." *Water Resources Research Journal.*

Knapp, R., & Civan, F. (1988). "Modeling growth and transport of microorganisms in porous media." *IMACS, f, 3*, 676679.

Korson, L., Drost-Hansen, W., & Millero, F. J. (1969). "Viscosity of water at various temperatures." *The Journal of Physical Chemistry*, *73*(1), 34-39.

Kozeny, J., Striedieck, W. F., & Wyllie, M. R. J. (1927). "Concerning Capillary Conduction of Water in the Soil:(Rise, Seepage and Use in Irrigation)." *Petroleum Branch of the American Institute of Mining and Metallurgical Engineers*.

Kralj, D., Brečević, L., & Kontrec, J. (1997). "Vaterite growth and dissolution in aqueous solution III. Kinetics of transformation." *Journal of crystal growth*, 177(3-4), 248-257.

Lasaga, A. C. (1981). "Rate laws of chemical reactions." *Rev. Mineral.*(United States), 8.

Lauchnor, E. G., Topp, D. M., Parker, A. E., & Gerlach, R. (2015). "Whole cell kinetics of ureolysis by S porosarcina pasteurii." *Journal of Applied Microbiology*, 118(6), 1321–1332.

Lebron, I., & Suarez, D. L. (1996). "Calcite nucleation and precipitation kinetics as affected by dissolved organic matter at 25 C and pH> 7.5." *Geochimica et Cosmochimica Acta*, 60(15), 2765-2776.

Lenormand, R., Touboul, E., & Zarcone, C. (1988). "Numerical models and experiments on immiscible displacements in porous media." *Journal of fluid mechanics*, *189*, 165-187.

Lin, Y. P., Singer, P. C., & Aiken, G. R. (2005). "Inhibition of calcite precipitation by natural organic material: kinetics, mechanism, and thermodynamics." *Environmental Science & Technology*, 39(17), 6420–6428.

Lioliou, M. G., Paraskeva, C. A., Koutsoukos, P. G., & Payatakes, A. C. (2007). "Heterogeneous nucleation and growth of calcium carbonate on calcite and quartz." *Journal of Colloid and Interface Science*, 308(2), 421–428.

Luhmann, A. J., Kong, X. Z., Tutolo, B. M., Garapati, N., Bagley, B. C., Saar, M. O., & Seyfried Jr, W. E. (2014). "Experimental dissolution of dolomite by CO2-charged brine at 100 C and 150 bar: Evolution of porosity, permeability, and reactive surface area." *Chemical Geology*, *380*, 145-160.

Luquot, L., & Gouze, P. (2009). "Experimental determination of porosity and permeability changes induced by injection of CO2 into carbonate rocks." *Chemical Geology*, *265*(1-2), 148-159.

Luquot, L., Rodriguez, O., & Gouze, P. (2014). "Experimental characterization of porosity structure and transport property changes in limestone undergoing different dissolution regimes." *Transport in Porous Media*, *101*(3), 507-532.

Mahabadi, N., & van Paassen, L.A. (2018). "Pore scale study of gas bubble nucleation and migration in porous media." *B2G Conference, Atlanta*, GA, September 10-13, 2018

Mahabadi, N., Zheng, X., & Jang, J. (2016). "The effect of hydrate saturation on water retention curves in hydrate-bearing sediments." *Geophysical Research Letters*, 43(9), 4279–4287.

Mahabadi, N., Zheng, X., Yun, T. S., van Paassen, L., & Jang, J. (2018). "Gas Bubble Migration and Trapping in Porous Media: Pore-Scale Simulation." *Journal of Geophysical Research: Solid Earth*, *123*(2), 1060-1071.

Mahabadi, N., van Paassen, L.A., Battiato, I., Yun, T. S., & Jang, J. (2019). "Impact of pore-scale characteristics on immiscible fluid displacement." *Journal of Petroleum Science and Engineering* (in review)

Martinez, B. C., Barkouki, T. H., DeJong, J. D., & Ginn, T. R. (2011). "Upscaling microbial induced calcite precipitation in 0.5 m columns: Experimental and

modeling results." In *Geo-Frontiers 2011*: Advances in Geotechnical Engineering (pp. 4049–4059).

Matty, J. M., & Tomson, M. B. (1988). "Effect of multiple precipitation inhibitors on calcium carbonate nucleation." *Applied Geochemistry*, 3(5), 549–556.

Menke, H. P., Bijeljic, B., Andrew, M. G., & Blunt, M. J. (2015). "Dynamic three-dimensional pore-scale imaging of reaction in a carbonate at reservoir conditions." *Environmental science & technology, 49*(7), 4407-4414.

Mitchell, A. C., & Ferris, F. G. (2006). "The influence of Bacillus pasteurii on the nucleation and growth of calcium carbonate." *Geomicrobiology Journal,* 23(3–4), 213–226.

Morse, J. W. (1983). "The kinetics of calcium carbonate dissolution and precipitation. Carbonates: Mineralogy and Chemistry" *Reviews in Mineralogy*, 11, 227-264.

Mortensen, B. M., Haber, M. J., DeJong, J. T., Caslake, L. F., & Nelson, D. C. (2011). "Effects of environmental factors on microbial induced calcium carbonate precipitation." *Journal of Applied Microbiology*, 111(2), 338–349.

Mullin, J. W. (2001). "Crystallization." *Elsevier*.

Nancollas, G. H., & Reddy, M. M. (1971). "The crystallization of calcium carbonate. II. Calcite growth mechanism." *Journal of Colloid and Interface Science*, 37(4), 824–830.

Nassar, M. K., Gurung, D., Bastani, M., Ginn, T. R., Shafei, B., Gomez, M. G., et al. (2018). "Large-Scale Experiments in Microbially Induced Calcite Precipitation (MICP): Reactive Transport Model Development and Prediction." *Water Resources Research*, 54(1), 480–500.

Nemati, M., & Voordouw, G. (2003). "Modification of porous media permeability, using calcium carbonate produced enzymatically in situ." *Enzyme and Microbial Technology*, 33(5), 635–642.

Nielsen, A.E. (1964). “Kinetics of precipitation” *International Series of Monographs in Analytical Chemistry* Vol. 18. Pergamon.

Noiriel, C., Bernard, D., Gouze, P., & Thibault, X. (2005). “Hydraulic properties and microgeometry evolution accompanying limestone dissolution by acidic water.” *Oil & gas science and technology*, *60*(1), 177-192.

Noiriel, C., Gouze, P., & Bernard, D. (2004). “Investigation of porosity and permeability effects from microstructure changes during limestone dissolution.” *Geophysical research letters*, *31*(24).

Noiriel, C., Steefel, C. I., Yang, L., & Ajo-Franklin, J. (2012). “Upscaling calcium carbonate precipitation rates from pore to continuum scale.” *Chemical Geology*, 318, 60-74.

Otsu, N. (1979). “A threshold selection method from gray-level histograms.” *IEEE Transactions on Systems, Man, and Cybernetics*, 9(1), 62–66.

Parkhurst, D. L., & Appelo, C. A. J. (2013). “Description of input and examples for PHREEQC version 3: a computer program for speciation, batch-reaction, one-dimensional transport, and inverse geochemical calculations.” *US Geological Survey*.

Perdikouri, C., Piazolo, S., Kasioptas, A., Schmidt, B. C., & Putnis, A. (2013). “Hydrothermal replacement of aragonite by calcite: interplay between replacement, fracturing and growth.” *European Journal of Mineralogy*, 25(2), 123-136.

Pereira Nunes, J. P., Blunt, M. J., & Bijeljic, B. (2016). “Pore-scale simulation of carbonate dissolution in micro-CT images.” *Journal of Geophysical Research: Solid Earth*, *121*(2), 558-576.

Pham, V. P., Nakano, A., van Der Star, W. R., Heimovaara, T. J., & van Paassen, L. A. (2016). “Applying MICP by denitrification in soils: a process analysis.” *Environmental Geotechnics*, *5*(2), 79-93.

Phillips, A. J., Gerlach, R., Lauchnor, E., Mitchell, A. C., Cunningham, A. B., & Spangler, L. (2013). “Engineered applications of ureolytic biomineralization: a review.” *Biofouling*, 29(6), 715–733.

Phillips, P. (1912). “The viscosity of carbon dioxide.” *Proceedings of the Royal Society of London. Series A, Containing Papers of a Mathematical and Physical Character*, *87*(592), 48-61.

Plummer, L. N., & Busenberg, E. (1982). “The solubilities of calcite, aragonite and vaterite in CO2-H2O solutions between 0 and 90 C, and an evaluation of the aqueous model for the system CaCO3-CO2-H2O.” *Geochimica et Cosmochimica Acta*, 46(6), 1011–1040.

Qin, C., Hassanizadeh, S. M., & Ebigbo, A. (2016). “Pore-scale network modeling of microbially induced calcium carbonate precipitation: Insight into scale dependence of biogeochemical reaction rates.” *Water Resources Research*, 52(11), 8794–8810.

Roberts, L. G. “Optical and Electro-optical Information Processing, chapter Machine perception of three-dimensional solids.” (1965): 159.

Salek, S. S., Bozkurt, O. D., van Turnhout, A. G., Kleerebezem, R., & van Loosdrecht, M. C. M. (2016). “Kinetics of CaCO3 precipitation in an anaerobic digestion process integrated with silicate minerals.” *Ecological Engineering*, 86, 105–112.

Sass, E., Morse, J. W., & Millero, F. J. (1983). “Dependence of the values of calcite and aragonite thermodynamic solubility products on ionic models.” *American Journal of Science*, 283(3), 218-229.

Smith, M. M., Sholokhova, Y., Hao, Y., & Carroll, S. A. (2013). “CO2-induced dissolution of low permeability carbonates. Part I: Characterization and experiments.” *Advances in Water Resources*, *62*, 370-387.

Söhnel, O., & Garside, J. (1992). “Precipitation: basic principles and industrial applications.” *Butterworth-Heinemann*.

Söhnel, O., & Mullin, J. W. (1982). “Precipitation of calcium carbonate.” *Journal of Crystal Growth*, 60(2), 239–250.

Stocks-Fischer, S., Galinat, J. K., & Bang, S. S. (1999). “Microbiological precipitation of CaCO3.” *Soil Biology and Biochemistry*, 31(11), 1563–1571.

Tai, C. Y., & Chen, P. (1995). “Nucleation, agglomeration and crystal morphology of calcium carbonate.” *AIChE Journal*, 41(1), 68–77.

Terzis, D., & Laloui, L. (2018). “3-D micro-architecture and mechanical response of soil cemented via microbial-induced calcite precipitation.” *Scientific Reports*, 8(1), 1416.

Ubbink, B. J. (2013). “Controlled Precipitation of Calcium Carbonate in Spatial Dimension with Multiple Calcium Chloride and Sodium Carbonate Pulses.”

Rebata-Landa, V., & Santamarina, J. C. (2012). “Mechanical effects of biogenic nitrogen gas bubbles in soils.” *Journal of Geotechnical and Geoenvironmental Engineering*, *138*(2), 128-137.

Vachaparambil, K. J., & Einarsrud, K. E. (2018). “Explanation of Bubble Nucleation Mechanisms: A Gradient Theory Approach.” *Journal of The Electrochemical Society*, 165(10), E504-E512.

Vandevivere, P., Baveye, P., de Lozada, D. S., & DeLeo, P. (1995). “Microbial clogging of saturated soils and aquifer materials: Evaluation of mathematical models." *Water Resources Research*, *31*(9), 2173-2180.

Van Paassen, L. A. (2009). “Biogrout: Ground Improvement by Microbially Induced Carbonate Precipitation.” Delft University of Technology. https://doi.org/10.1111/idj.12061

Van Paassen, L. A., Daza, C. M., Staal, M., Sorokin, D. Y., van der Zon, W., & van Loosdrecht, M. C. (2010). “Potential soil reinforcement by biological denitrification.” *Ecological Engineering*, *36*(2), 168-175.

Van Paassen, L. A., Ghose, R., van der Linden, T. J. M., van der Star, W. R. L., & van Loosdrecht, M. C. M. (2010). “Quantifying biomediated ground improvement by ureolysis: large-scale biogrout experiment.” *Journal of Geotechnical and Geoenvironmental Engineering*, 136(12), 1721–1728.

Van Wijngaarden, W. K., van Paassen, L. A., Vermolen, F. J., van Meurs, G. A. M., & Vuik, C. (2016). “A reactive transport model for biogrout compared to experimental data.” *Transport in Porous Media*, 111(3), 627–648.

Van Wijngaarden, W. K., Vermolen, F. J., van Meurs, G. A. M., & Vuik, C. (2011). "Modelling biogrout: a new ground improvement method based on microbial-induced carbonate precipitation." *Transport in Porous Media*, 87(2), 397–420.

Van Wijngaarden, W. K., Vermolen, F. J., van Meurs, G. A. M., & Vuik, C. (2012). "A mathematical model and analytical solution for the fixation of bacteria in biogrout." *Transport in Porous Media*, 92(3), 847–866.

Van Wijngaarden, W. K., Vermolen, F. J., van Meurs, G. A. M., & Vuik, C. (2013). "A mathematical model for Biogrout." *Computational Geosciences*, 17(3), 463–478.

Wang, Y., Soga, K., Dejong, J. T., & Kabla, A. J. (2019). "A microfluidic chip and its use in characterising the particle-scale behaviour of microbial-induced calcium carbonate precipitation (MICP)." *Géotechnique*, 1-9.

Whiffin, V. S., van Paassen, L. A., & Harkes, M. P. (2007). "Microbial carbonate precipitation as a soil improvement technique." *Geomicrobiology Journal*, 24(5), 417–423.

Whiffin, V. S. (2004). "Microbial CaCO3 precipitation for the production of biocement." Murdoch University.

White, E. T., & Beardmore, R. H. (1962). "The velocity of rise of single cylindrical air bubbles through liquids contained in vertical tubes." *Chemical Engineering Science*, 17, 351–361.

Yasuhara, H., Neupane, D., Hayashi, K., & Okamura, M. (2012). "Experiments and predictions of physical properties of sand cemented by enzymatically-induced carbonate precipitation." *Soils and Foundations*, 52(3), 539–549.

Yoon, H., & McKenna, S. A. (2012). "Highly parameterized inverse estimation of hydraulic conductivity and porosity in a three-dimensional, heterogeneous transport experiment." *Water Resources Research*, 48(10).

Zhang, C., Dehoff, K., Hess, N., Oostrom, M., Wietsma, T. W., & Valocchi, A. J., et al. (2010). "Pore-scale study of transverse mixing induced CaCO3 precipitation and permeability reduction in a model subsurface sedimentary system." *Environmental Science & Technology*, 44(20), 7833–7838.

Zhang, C., M. Oostrom, T. W. Wietsma, J. W. Grate, & M. G. Warner (2011). "Influence of viscous and capillary forces on immiscible fluid displacement: pore-scale experimental study in a water-wet micromodel demonstrating viscous and capillary fingering." *Energy & Fuels*, 25(8), 3493-3505.

Zhang, L., Soong, Y., Dilmore, R., & Lopano, C. (2015). "Numerical simulation of porosity and permeability evolution of Mount Simon sandstone under geological carbon sequestration conditions." *Chemical Geology, 403*, 1-12.

Zhao, Q., Li, L., Li, C., Li, M., Amini, F., & Zhang, H. (2014). "Factors affecting improvement of engineering properties of MICP-treated soil catalyzed by bacteria and urease." *Journal of Materials in Civil Engineering*, 26(12), 4014094.

Zheng, X., Mahabadi, N., Yun, T. S., & Jang, J. (2017). "Effect of capillary and viscous force on CO2 saturation and invasion pattern in the microfluidic chip." *Journal of Geophysical Research: Solid Earth*, 122(3), 1634–1647.